



**FACULTY  
OF MATHEMATICS  
AND PHYSICS**  
**Charles University**

**DOCTORAL THESIS**

Mgr. Lucia Tódová

**Advances in Spectral Uplifting and  
Reconstruction**

Department of Software and Computer Science Education

Supervisor of the doctoral thesis: prof. Dr. techn. Alexander Wilkie

Study programme: Computer Science

Study branch: Visual Computing and Computer  
Games

Prague 2025

I declare that I carried out this doctoral thesis on my own, and only with the cited sources, literature and other professional sources. I understand that my work relates to the rights and obligations under the Act No. 121/2000 Sb., the Copyright Act, as amended, in particular the fact that the Charles University has the right to conclude a license agreement on the use of this work as a school work pursuant to Section 60 subsection 1 of the Copyright Act.

In ..... date .....  
Author's signature

*Dedicated to everyone who helped me gain confidence even when I couldn't find it on my own.*

I would like to thank my husband for his constant support and unwavering belief in me. His patience, encouragement and help have been an anchor throughout this journey.

I thank my parents for introducing me to computer science early on, and for not only teaching me the skills, but also the confidence to pursue what I love. I extend the thank you to my family and closest friends, whose support and interest in my work have been invaluable.

I also thank my supervisor, Alexander Wilkie, for stepping up during the most challenging times, and introducing me to the work I would not have been able to pursue otherwise. I am also thankful to my colleagues, whose encouragement and support – especially at the start – made all the difference. A special acknowledgment is also due to the entire rendering team at Weta Digital for their generosity with time, their patience and guidance during my brief stay – an experience that has significantly shaped my professional development.

Finally, I would like to thank Jaroslav Křivánek for introducing me to the fascinating world of rendering. Even though he was not around to see my research, his legacy endures – impacting my work and inspiring many beyond.

This work has received funding from the Czech Science Foundation (grant number GAČR-22-22875S), and from the Charles University GA UK grant (grant number 252126). Additionally, the work was further supported by Vladimir Koylazov, co-founder of Chaos, and by the Intel oneAPI Center of Excellence through funding of the Computer Graphics Group.

Title: Advances in Spectral Uplifting and Reconstruction

Author: Mgr. Lucia Tódová

Department: Department of Software and Computer Science Education

Supervisor: prof. Dr. techn. Alexander Wilkie, Department of Software and Computer Science Education

**Abstract:** Renderers are integral to computer graphics, enabling realistic simulation of light in 3D scenes across a wide range of applications, including the movie industry, architectural visualizations, medical imaging, etc. While traditional rendering pipelines often rely on RGB-based representation of material properties due to its simplicity, novel approaches achieve a higher degree of realism by using the spectral representation, which reflects real-world behavior. However, adoption of a spectral rendering pipeline poses multiple challenges, with the scarcity of spectral assets being among the most significant ones. To address this, a common practice is to create them in the RGB color space and subsequently convert them into their spectral counterparts – with a process called spectral uplifting. As multiple different spectra can correspond to the same RGB value (a phenomenon called metamerism), designing an effective spectral uplifting system is inherently complex – and even despite the current advancements, the research field has many areas for improvement. This thesis broadens the current scope by introducing two novel uplifting approaches – first, the option of wide gamut constrained uplifting, which allows the user to specify the shapes the spectra should achieve, and second, a physically based approach for uplifting for image-based lighting, i.e. HDR environment maps. Additionally, a novel approach for estimating spectral properties of light sources from only their RGB captures is proposed, which has the potential to replace the need for their uplifting altogether.

**Keywords:** spectral uplifting, spectral rendering, image-based lighting, color science

# Contents

<b>Introduction</b>	<b>6</b>
<b>1 Background</b>	<b>8</b>
1.1 Color Science . . . . .	8
1.1.1 Light Transport . . . . .	8
1.1.2 Color Perception . . . . .	10
1.1.3 Color Representation . . . . .	11
1.1.4 Rendering . . . . .	16
1.1.5 Metamerism . . . . .	18
1.2 Spectral Uplifting . . . . .	19
1.2.1 Requirements . . . . .	20
1.2.2 Existing Methods . . . . .	23
1.2.3 Constrained Spectral Uplifting . . . . .	28
<b>2 Wide Gamut Constrained Spectral Uplifting</b>	<b>30</b>
<b>3 HDR Environment Map Uplifting</b>	<b>48</b>
<b>4 Spectral Emission Estimation of Light Sources</b>	<b>66</b>
<b>Conclusion</b>	<b>78</b>
<b>Bibliography</b>	<b>80</b>
<b>List of Figures</b>	<b>84</b>

# Introduction

In recent years, the field of rendering has seen significant advancements in its capability of reproducing real-world appearance. This is achieved by both incorporating physically based principles of light transport into renderers, but also by taking advantage of more powerful hardware and novel optimization techniques.

However, despite these improvements, there are still numerous application areas in which even small discrepancies between the rendered output and real-world behavior can result in perceptible and problematic artifacts. This is especially prevalent in the visual effects industry (VFX), where it is common to extensively switch between plate footage and its digital counterpart during a single shot. In such cases, even subtle appearance differences are likely to be caught by the human eye. Similar issues can arise in the product manufacturing industry when, for example, real-life products in store do not match catalogue renders.

One of the primary causes of such discrepancies is the use of RGB-based renderers. While in the real world, material properties, such as reflectance, transmission, absorption, etc., are represented as a continuous wavelength distribution, RGB-based renderers simplify this by storing them as 3 floating point values only. Although this allows for a more efficient representation and a significantly better performance, it reduces the whole light transport process into an approximation of real-world behavior rather than an accurate simulation.

This is where spectral rendering offers its distinct advantage. As opposed to using tristimulus values, spectral renderers simulate the process of light transport for every wavelength and therefore have the potential to match real-world appearance almost perfectly. The capability of physically correct simulation comes with an additional benefit of accurate reproduction of natural phenomena, such as fluorescence, phosphorescence, metamerism, etc., which are currently only supported in RGB-based renderers via makeshift solutions.

However, in addition to the performance overhead, the use of spectral renderers is further complicated by the scarcity of spectral assets, such as materials or textures. While it is possible to obtain them directly, the existing methods are often subject to significant limitations. One option is to perform manual measurements, which require specialized equipment, are time-consuming and, most importantly, crucially depend on the availability of a physical counterpart – a prerequisite that is not met in many scenarios. The alternative is direct modeling of the assets in the spectral domain, which is unintuitive for the artists and is therefore typically reserved for only highly specialized applications. Another factor contributing to the problem is that a lot RGB-based assets already exist – and recreating their spectral counterparts from scratch is an extremely costly and resource-intensive process.

As a result, the general approach is to create the assets in the RGB color space and convert them into the spectral domain. This process is called *spectral uplifting* (also referred to in other works as spectral upsampling).

However, the relationship between the spectral and the RGB domain is surjective, meaning that multiple different spectra can map to the same RGB value. This phenomenon, known as *metamerism*, makes spectral uplifting a fundamentally underconstrained problem – and while current methods are capable of producing

spectra that evaluate to the target RGB value, they generally do not have control over the obtained spectral shape. This can lead to a mismatch between the resulting uplifts and their real-life counterparts, which, in turn, may cause inaccuracies in the light transport process and ultimately affect the final appearance of the rendered image. These deviations can range from subtle shifts in the color of individual objects to dramatic changes in the overall scene, particularly when illumination is significantly affected.

This thesis provides multiple contributions to the field of spectral uplifting and spectral reconstruction. We introduce them as follows:

In Chapter 2, we present a method capable of wide gamut *constrained* reflectance uplifting. The approach provides the novel ability to preserve user-defined spectra while ensuring that the rest of the gamut attains similar shapes, thus effectively preventing color artifacts. This is especially useful for VFX workflows, where specific material properties (such as saturated fabrics or even unnatural skin tones of a character) need to be reproduced with an extremely high degree of accuracy. This work can be viewed as an extension of our previous Master’s thesis and a subsequent publication (Tódová; Wilkie; Fascione, 2021) that supported the sRGB gamut only, which inherently lacks the capability to represent such materials and therefore is of limited practical applicability.

Following our work on reflectance uplifting, our next research focuses on uplifting emission, specifically HDR environment maps. Summarized in Chapter 3, the topic choice was motivated by the significant appearance difference when comparing their ground truth measurements to their current state-of-the-art uplifts. We provide a significant improvement by basing the proposed technique on a database of real-life emission measurements of the light sources found in the environment maps.

The need to determine spectral properties of light sources in environment maps loosely inspired our latest work presented in Chapter 4. The proposed method focuses on estimating spectral emission of light sources present during camera capture, and requires only a single input: an RGB capture containing a color target, commonly used in standard production pipelines for the purposes of color calibration. The main benefit of this work is that it proposes a way to eliminate the need for spectral uplifting of illumination altogether, and obtain the emission with a simple and lightweight solution, without the need for an extensive database of measurements. In addition to aiding VFX workflows, we also discuss multiple other scenarios for its application, such as in the product manufacturing industry.

Overall, this doctoral thesis consists of 2 journal publications and 1 conference proceeding, all of which are first-authored and listed in the List of Publications. Additionally, our most recent work is currently being prepared for resubmission, having undergone one round of peer review after being rejected at Eurographics Symposium on Rendering 2025. The version included in this thesis incorporates revisions based on the reviewers’ feedback.

# 1 Background

In computer graphics, the term *physically based rendering* is used to describe the process of generating an image through physically accurate simulation of light transport. In order to replicate real-world behavior, this requires both a precise emulation of light interactions with distinct objects and surfaces; and an accurate representation of material properties, such as reflectance, emission, transmission, etc. This thesis concerns itself with the latter – specifically, with obtaining physically plausible material properties from existing resources that generally do not contain sufficient information.

This chapter contains the overview of the terms and concepts necessary to motivate our research. First, it introduces the physical principles that govern the process of light transport, and moves on to the concept of color and human perception, which is covered along with an overview of existing color spaces. Their use in rendering and the significant distinction between tristimulus and spectral color representation further explain the phenomenon of metamerism, which can be considered one of the main motivators of our research. Together with other phenomena, this necessitates focus on spectral uplifting. Lastly, an overview of the existing uplifting techniques is provided, along with our prior research which is extended in this thesis.

## 1.1 Color Science

### 1.1.1 Light Transport

In the context of physics, the term light transport is closely related to *electromagnetic radiation*. Electromagnetic radiation can be viewed as radiant energy that is being propagated through space in the form of waves. A specific electromagnetic wave is defined by both its amplitude and frequency, which, together, give rise to the term *wavelength*, denoted  $\lambda$ .

Every type of electromagnetic radiation can be defined by its wavelength. Depending on its range, we distinguish between different types of radiation –

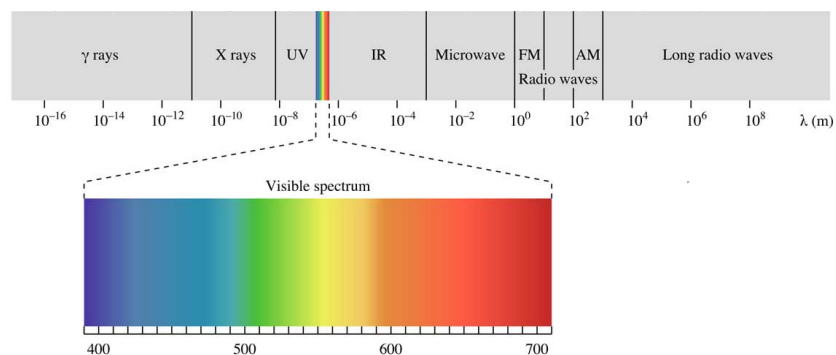


**Figure 1.1** The electromagnetic spectrum. While it spans a wide range of wavelengths, from as short as 1 pm to as long as 100 Mm, the visible spectrum this thesis is concerned with covers only the range from around 380 nm up to around 780 nm.

starting from gamma rays and X-rays, through ultraviolet radiation, visible light and infrared radiation, up to microwaves and radio waves – making up the whole of the electromagnetic spectrum (see Figure 1.1). In this thesis, we specifically concern ourselves with the *visible spectrum*, which is the radiation that is perceivable by the human eye and generally corresponds to the wavelengths from around 380 nm up to around 780 nm.

The most elementary particle of light and all other forms of electromagnetic radiation is a *photon*. For our purposes, it can be viewed as an energy packet that is created during energy release by an emitter (e.g., a light source). Then, it travels through space according to its specific wavelength, carrying radiant energy. Upon hitting a surface, the photon can be absorbed, which results in an energy transfer, or it can be redirected, depending on the properties of the point of interaction.

While a single photon is characterized by its one wavelength, light sources emit photons for a whole range. The distribution of radiant energy carried by photons across the wavelengths of the electromagnetic spectrum is referred to as the *emission spectrum* of a light source (see Figure 1.2a). Due to the nature of light sources, emission spectra are, from a mathematical point of view, considered to be *unbounded*.

The behavior of photons upon interaction with a material is characterized in a similar manner. For example, the likelihood of photons reflecting from a given material is defined by its *reflectance spectrum* (see example in Figure 1.2b). Bounded by 0 and 1, reflectance curves specify the *percentage* of photons reflected for every wavelength. Therefore, if a light source with an emission  $E(\lambda)$  illuminates an object with the reflectance  $R(\lambda)$ , the final energy  $P(\lambda)$  that is further propagated is the result of the combination  $P(\lambda) = E(\lambda) \cdot R(\lambda)$  (see Figure 1.2c).

All other material properties can be defined in a similar manner. For example, the transmission spectrum, also bounded by 0 and 1, describes the proportion of photons that pass through the given material, while the absorption spectrum specifies how much light is absorbed for each wavelength.

Although the independence of photons of one another suggests that spectra could attain arbitrary shapes, in practice, this is fundamentally constrained by the physical and chemical structure of the individual materials. As described by Nassau

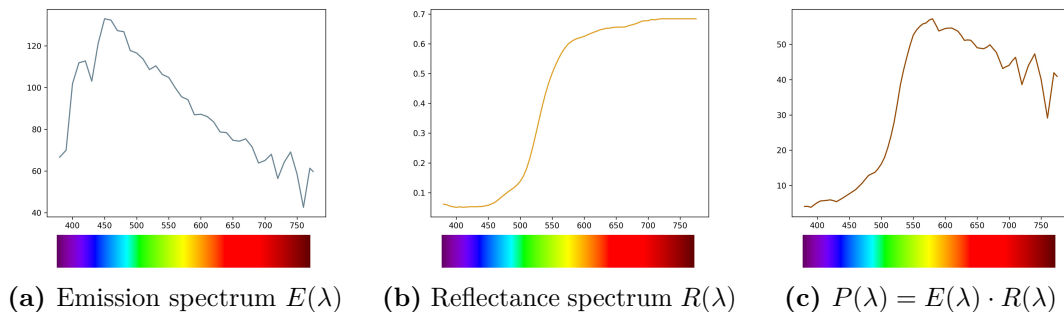


**Figure 1.2** Examples of spectral properties of objects and materials and their interaction. Note that if the emission spectrum were a laser (i.e. photons are only emitted for a single wavelength), only the radiant energy from its wavelength could be further propagated into the scene. This also explains why pure black objects (i.e.  $R(\lambda) = 0$  for every  $\lambda$ ) do not reflect any light.

(1987), fifteen specific color-producing mechanisms can be distinguished, such as simple excitations and vibrations, molecular orbitals, energy bands, geometrical and physical optics, etc. As their result, materials exhibit spectral properties that follow specific, repeatable patterns – for example, emission spectra of fluorescent light sources are prone to spikes at specific wavelengths, while daylight illumination is almost exclusively smooth with an elevated intensity in the blue region of the visible spectrum. These observations are essential to our work, which is based on the key assumption that spectral shapes directly correlate with specific materials.

The varied spectral properties of the scene’s objects govern the behavior of individual photons, determining which are reflected, transmitted, or absorbed. This ultimately shapes the spectral composition of photons that reaches the human eye. Their absorption by the retina is what eventually gives rise to human visual perception.

### 1.1.2 Color Perception

In order to allow vision, the human retina contains millions of cells called photoreceptors. Based on their function, these are categorized into rods and cones (Wyszecki; Stiles, 2000).

*Rods* make up most of the receptor cells and are usually located at the corner of the retina. They contain the protein rhodopsin, which reacts to light intensity and therefore mediates low-light (*scotopic*) vision. However, they do not possess the capability of color recognition, which explains the human eye’s reduced ability to distinguish colors in poor lighting conditions (e.g., at night).

*Cones*, on the other hand, are located in the center of the retina. They are active during daylight and are responsible for color vision. Generally, there are three types of cones: the *L-cones*, which are most sensitive to longer wavelengths at around 560 nm, the *M-cones*, which are most responsive to medium wavelengths

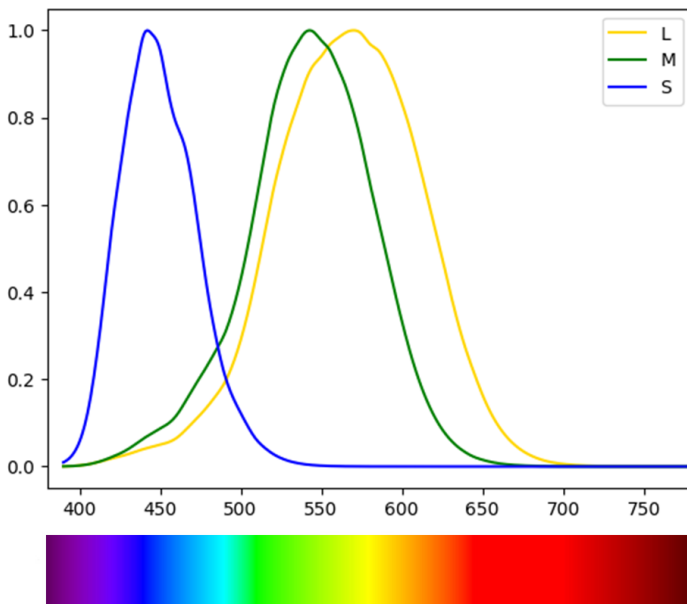


**Figure 1.3** Relative cone sensitivities by Stockman and Sharpe (2000). Data obtained from the Colour Library for Python (2013).

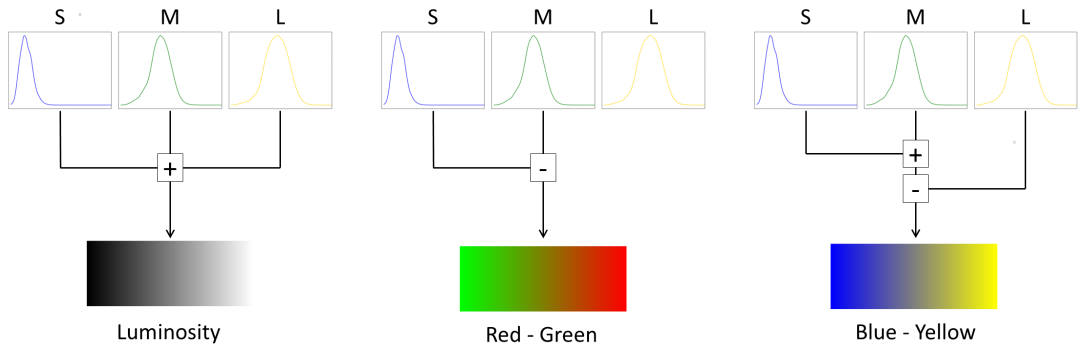


**Figure 1.4** Color processing of the human brain from the stimulation of individual cone types, as described by the opponent process (Judd, 1949). While the summation of all cone responses gives rise to luminosity, the individual values of the respective chromaticity channels (red-green and blue-yellow) are obtained through a more complex process of addition and subtraction. Together, the three channels give rise to the final color.

at around 530 nm, and *S-cones*, which respond to shorter wavelengths at around 420 nm. We provide their relative response to stimulation in Figure 1.3.

This type of perception is called *trichromatic*, as it uses 3 types of stimuli to create the whole space of perceptible colors. In specific cases, a certain type of cones may be missing, resulting in dichromatic or even monochromatic vision. This is referred to as colorblindness and results in a limitation of the space of the perceptible colors.

When light (in the form of a spectral power distribution) hits the retina, the cones are stimulated with the respective energy absorbed from the photons. The processing of the stimulation by the human brain then gives rise to the notion of *color* as we know it. However, it is important to note that the mechanisms that govern this process are much more complex than a simple summation of cone responses – involving not only additive but also subtractive processing (Judd, 1949).

A good example of that is the perception of the color red. Although there is no cone type that responds exclusively to wavelengths in the red region (see Figure 1.3), the human brain is capable of constructing the sensation for inputs where the L-cones are strongly stimulated, M-cones weakly, and S-cones not at all – by subtracting the stimulation of M-cones from L-cones. This effectively isolates the contribution of wavelengths in the red region, thus giving rise to the perception of red color.

In Figure 1.4, we provide a simplified illustration of how the human brain processes the stimulation of individual cone types. This shows that the simulation of human color perception requires a much more complex process than just a replication of individual cone responses.

### 1.1.3 Color Representation

In a rendering system, the camera defines both the viewpoint and the viewing direction, determining how the scene is observed and ultimately rendered. Therefore, similarly to the human eye, the camera also captures the light traveling

through space and is later responsible for its processing.

Once the light is captured, it must be interpreted and represented in a form suitable for the renderer. However, unlike real-world color, which is described by a continuous spectral power distribution, renderers operate in a discrete domain and therefore cannot directly process such input. This is addressed by discretizing the spectral data.

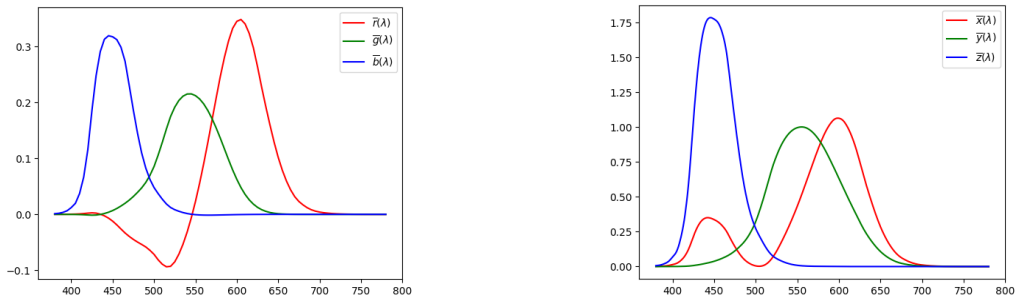
One of the most straightforward approaches of achieving this is through *sampling*. This type of color representation in a renderer is known as the *spectral representation*, and renderers that simulate light transport at individual wavelengths are likewise referred to as spectral. In practice, when a sufficiently dense sampling rate is used, this approach offers the most accurate approximation of real-world light transport that is currently achievable in rendering.

However, in order to faithfully capture all the features that can be present in spectral curves, a high sampling rate is often required. While general reflectance data are usually sampled with at least 30 samples at 10 nm rate (Alexander Wilkie, 2018), more complex lighting, such as fluorescent illuminants, require at least 5 nm increments (Lehtonen et al., 2006). The requirements further increase with higher demands on color accuracy – for example, in production and research areas alike, it is customary to sample the more complex resources with 1 nm increments. Representing every material in this manner, not to mention executing the rendering process for every represented wavelength (i.e. up to 400 times per light interaction), imposes significant performance and memory overhead.

This is where *tristimulus representations*, which describe colors with three components only, become particularly useful.

## CIE RGB Color Space

When creating a tristimulus color space, the original idea was to quantify the typical trichromatic human eye response with three color matching functions. A set of color matching experiments was conducted by Wright and Guild (Broadbent, 2004), the results of which were, in 1931, used by the CIE (International Commission on Illumination) as a basis to define the first set of color matching functions (also called *primaries*) (Fairman; Brill; Hemmendinger, 1997). They were referred to as the  $\bar{r}(\lambda)$ ,  $\bar{g}(\lambda)$  and  $\bar{b}(\lambda)$  primaries (see Figure 1.5a), and their respective tristimulus color space (i.e. all colors that can be created by using the



(a) The CIE 1931 RGB color matching functions (Broadbent, 2004).

(b) The CIE XYZ color matching functions (CIE, 2019).

**Figure 1.5** Color matching functions.

primaries) was named the CIE RGB color space. The RGB value of any spectral power distribution (SPD)  $S(\lambda)$  in the color space is then given by:

$$\begin{aligned} R &= \int_0^{\infty} S(\lambda) \bar{r}(\lambda) d\lambda \\ G &= \int_0^{\infty} S(\lambda) \bar{g}(\lambda) d\lambda \\ B &= \int_0^{\infty} S(\lambda) \bar{b}(\lambda) d\lambda \end{aligned}$$

### CIE XYZ Color Space

After the definition of the CIE RGB color space, the CIE special commission aimed to derive a new set of color matching functions based on it (Ohno, 2000). The main goal was to eliminate the presence of negative factors from the primaries (namely from the  $\bar{r}(\lambda)$  function of CIE RGB), and to make one of the new primaries equal to the photopic luminous efficiency function, i.e. human perception of luminance. This effort resulted in the creation of the color matching functions  $\bar{x}(\lambda)$ ,  $\bar{y}(\lambda)$  and  $\bar{z}(\lambda)$ , with  $\bar{y}(\lambda)$  corresponding to the standard photopic observer (see Figure 1.5b). Their respective color space was then named CIE XYZ. Similarly to the CIE RGB color space, the XYZ coordinates of any SPD  $S(\lambda)$  are given by:

$$\begin{aligned} X &= \int_0^{\infty} S(\lambda) \bar{x}(\lambda) d\lambda \\ Y &= \int_0^{\infty} S(\lambda) \bar{y}(\lambda) d\lambda \\ Z &= \int_0^{\infty} S(\lambda) \bar{z}(\lambda) d\lambda \end{aligned} \tag{1.1}$$

where the Y component corresponds to luminance and the combination of the X and Z components therefore gives rise to chromaticity.

In contrast to most of the available color spaces, the CIE XYZ space is *imaginary*, which means that its primaries do not correspond to physically realizable colors. As a result of this design choice, any existing color can be expressed as a positive combination in the CIE XYZ space. This, along with the space being device-independent, is the reason why CIE XYZ serves as a standard reference against which multiple other color spaces are defined. Generally, the conversion from a spectral representation to an arbitrary space is performed by first obtaining the XYZ coordinates (using Equation 1.1), and then applying a transform by means of a space-specific  $3 \times 3$  matrix to obtain the final value.

However, the theoretical nature of the CIE XYZ space does not allow it to be used in practice. Therefore, despite its widespread use in theoretical research areas, real-world applications rely on alternative color spaces. In the context of rendering, the most commonly used are the RGB color spaces.

### RGB Color Spaces

RGB color spaces are additive spaces that are based on three primaries – **Red**, **Green** and **Blue**. They differ in the exact definitions of these primaries and therefore in their *color gamut*.

A color gamut of a color space is the set of all colors that its primaries are capable of reconstructing. In the case of RGB spaces, it can be conceptually

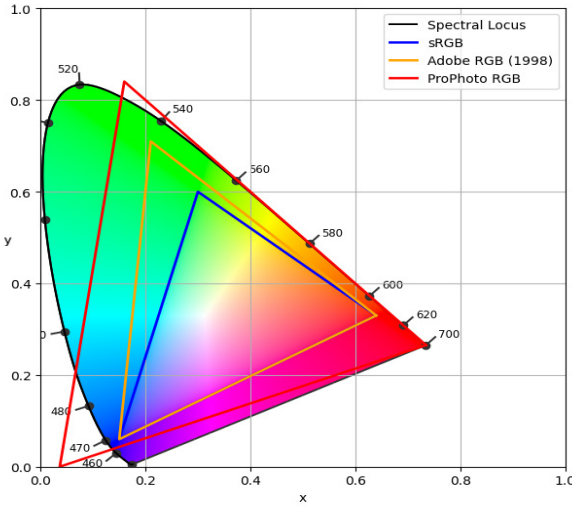


**Figure 1.6** Color gamuts of some of the most popular RGB color spaces visualized in the chromaticity diagram. Note that some spaces (such as ProPhoto RGB) may have imaginary primaries, meaning the primaries are outside the gamut of realizable reflectances.

understood as the range of colors that can be generated by varying the intensities of three lasers, each corresponding to one of the primaries. Usually, the range of the intensities is bounded by 0 and 1 – alternatively, the [0, 255] range is used. Therefore, any RGB color space can be represented by a cube in three-dimensional Euclidean space. However, we note that this does not imply that every point within the cube corresponds to a physically realizable color – on the contrary, for many RGB color spaces, some parts of the cube remain outside the spectral locus. A notable exception to this is the sRGB color space, which is also later discussed in this context as part of our work (see Chapter 2).

The reason for multiple RGB color spaces is the need to accommodate the specific characteristics of different display devices and applications. For example, web or mobile phone applications prioritize consistency across devices and platforms, which is why they often rely on standardized color spaces with smaller gamuts in order to also be reliably reproduced on devices with limited reconstruction capabilities. Newer technologies, on the other hand, offer wider color gamuts and therefore an enhanced vibrancy, which is desired in specific application areas, such as in photography or in the movie industry.

In Figure 1.6, we provide an illustration of the color gamuts of some of the most commonly used RGB spaces, plotted in a 2D diagram called the *chromaticity diagram*.

The chromaticity diagram (Ohno, 2000) is often used as a tool for analyzing gamut coverages, as it encapsulates all the existing chromaticities perceivable by the human eye. Within it, the gamut of any RGB tristimulus color space can be visualized as a triangle, with its corners being the three respective primaries. While the provided figure highlights a selected subset of existing RGB color spaces, multiple others exist (Süsstrunk; Buckley; Swen, 1999), including ISO RGB, Wide Gamut RGB, and Apple RGB. The previously discussed CIE RGB color space also falls into this category – however, it is not as widely adopted in practical

applications.

In research work on rendering methods and in computer graphics in general, the sRGB gamut is frequently referenced due to its widespread use and its role as the basis for many industry standards. However, since the target application areas of our work lie in the movie industry and product design – both of which require a higher level of color vibrancy – our focus is placed on wider color gamuts. This includes the full gamut of realizable reflectances, which, as opposed to three primaries, is bounded by a line referred to as the *spectral locus* (see Figure 1.6). The colors corresponding to the points of the spectral locus are pure spectral colors (Fairchild, 2008), which means that their spectral representation only corresponds to a single wavelength (also called *monochromatic light*). Any color outside the area defined by the spectral locus is not perceivable by the human eye.

## Other Color Spaces

Generally, renderers based on the tristimulus representation use the RGB color space to describe material properties and therefore to also simulate light transport. However, other color spaces can also be incorporated into the rendering process for different purposes.

One of such spaces is the  $L^*a^*b^*$  (or CIELAB) color space (standard by CIE, 2007). Designed with the goal of a more accurate representation of human color perception, the space separates the lightness ( $L^*$ ) of a color from its chromaticity ( $a^*$  and  $b^*$ ). In contrast to RGB color spaces, the Euclidean difference between two CIELAB colors directly correlates with how distinct they are in terms of human perception. This makes CIELAB particularly useful for color comparisons and adjustments that require perceptual uniformity.

Its wide use for such purposes led to the definition of the Delta E ( $\Delta E$ ) metric (CIE, 2007), which is currently considered standard for measuring color differences. Initially defined in 1976 as a simple Euclidean distance in the CIELAB color space (denoted  $\Delta E_{ab}^*$ ), it has since been refined to compensate for some perceptual inconsistencies that are a result of the shortcomings of the space. These improvements resulted in Delta E 94 (CIE, 2007) and, eventually, the currently used *Delta E 2000* ( $\Delta E_{00}^*$ ) (Sharma et al., 2005). In our work, we mostly rely on the latter, and use it to evaluate the effectiveness of our proposed methods.

While perceptual uniformity has driven the development of several additional color spaces – such as  $L^*u^*v^*$  (CIELUV) (Schanda, 2007) and HSLuv – multiple other spaces have also been created with different objectives in mind (Joblove; Greenberg, 1978). For example, cylindrical spaces, such as HSV, HSL, or LCh, were designed to offer more intuitive controls for artists and designers by separating hue, saturation, and lightness, and are generally useful for color selection tools, graphic design interfaces, and other creative visual design applications. Subtractive color spaces, such as CMYK and CMY, are standard in the printing process, and commercial color systems, such as the Munsell Color System, the Pantone Matching System, or RAL, are widely adopted in industry for standardized color specification.

For more information on distinct color spaces and their specific properties, we refer the reader to the work by Ibraheem et al. (2012).

### 1.1.4 Rendering

Generally, the core input to a rendering system is a scene containing a pre-defined set of objects with known material properties, and a specification of the camera position and view angle. The renderer then processes this scene and executes a light transport algorithm, thus producing the final *render*.

While the render is almost always in the RGB format in order for it to be easily displayed on monitors and screens, the internal representation of color during the light transport process categorizes renderers into two main types – spectral and RGB renderers. Generally, other color spaces are not used for performing light transport calculations due to reasons rooted in their foundational design.

While RGB renderers directly display the results of light transport, spectral renderers must perform a conversion into an RGB space. This entails the computation of the XYZ coordinates (by means of Equation 1.1) and then a multiplication with a  $3 \times 3$  RGB space-specific matrix. As the discretized nature of computational systems does not allow a 100% accurate calculation of an integral, the conversion from a spectrum to XYZ requires the discretization of the spectrum and then the computation of the following sum:

$$\begin{aligned} X &= \sum_{i=0}^n S[i] \cdot x[i] \cdot inc \\ Y &= \sum_{i=0}^n S[i] \cdot \bar{y}[i] \cdot inc \\ Z &= \sum_{i=0}^n S[i] \cdot \bar{z}[i] \cdot inc \end{aligned} \tag{1.2}$$

where  $S$  is the discretized spectrum (with  $S[i]$  being its  $i$ th element),  $n$  is the number of samples of  $S$ ,  $inc$  is the increment with which the spectrum is sampled (in nanometers), and  $\bar{x}$ ,  $\bar{y}$  and  $\bar{z}$  are the respective color matching functions sampled at the same sampling rate as  $S$ . The resulting XYZ values are therefore only an approximation, and the specific sampling rate used depends on the desired color accuracy of the result as well as on the sampling rates used internally for light transport algorithms and material representation.

As previously discussed, the fundamental distinction between the two color representations lies in the spectral representation being physically based. This gives rise to multiple other key differences between them:

**Performance Requirements.** While RGB-based renderers only need to simulate the light transport algorithm for 3 components, wavelength-dependent simulation requires a much larger number of samples, leading to higher computational costs. While optimization techniques, like Hero Wavelength Sampling (Wilkie; Nawaz, et al., 2014), help reduce this overhead, there is currently no way to fully eliminate it.

**Memory Requirements.** Similar to execution time, storing spectral information for material properties requires substantially more memory than storing simple RGB values. This is especially prevalent in production spectral renderers, which generally use a sampling rate of as little as 1 nm or even 0.5 nm increments. And while this can be reduced by using techniques such

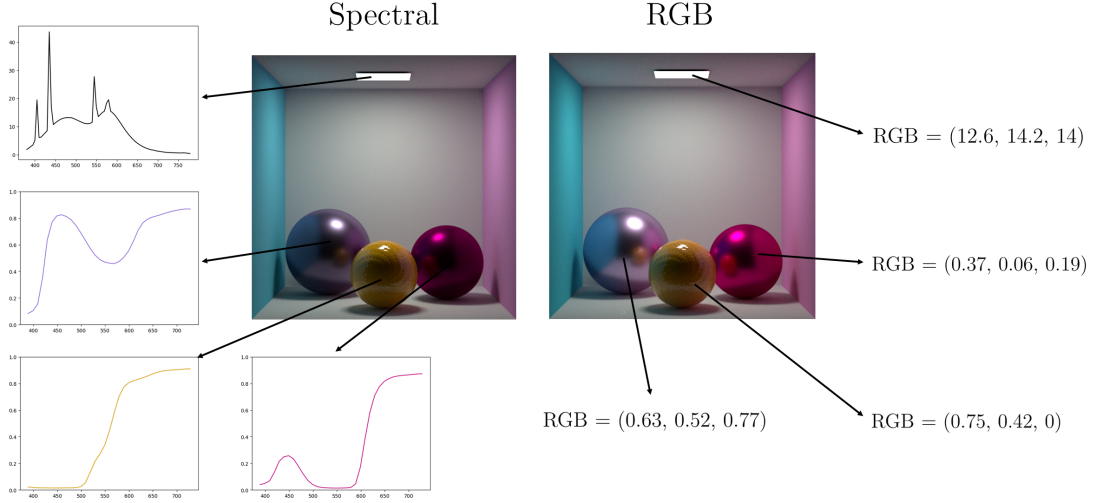


**Figure 1.7** Comparison of the same scene rendered with a spectral and an RGB renderer – specifically, the `scalar_spectral` and `scalar_rgb` variants of Mitsuba 3 (Jakob; Speierer, et al., 2022) are used. The materials in the RGB scene are obtained by performing a conversion from their spectral counterparts by means of Equation 1.2 and a subsequent  $3 \times 3$  space-specific matrix transform.

as basis compression for spectral storage, these, especially in case of complex spectra, result in a decrease of precision, which is undesired and therefore generally not practiced in professional environments.

**Simulation of Real World.** While spectral renderers have an inherent capability to simulate real-world behavior, in RGB renderers, the whole process of light transport and its specific material interactions can be seen as only a coarse approximation. This results in less accurate reflections, refractions, transmissions, etc., which, in turn, decreases the realism of the final render. We show an example of this in Figure 1.7, where we present a comparison of the same scene rendered with both renderers. Even in a simplified scene such as the one shown, the differences are rather significant.

**Natural Phenomena.** Natural phenomena, such as fluorescence, phosphorescence, metamerism, etc., usually occur due to complex interactions between light and matter at specific wavelengths. As RGB renderers inherently do not have the capability to simulate wavelength-dependent behavior, they rely on creative workarounds. By definition, these are not physically plausible, which leads to a mismatch between their results and the results of spectral light transport. And while most natural phenomena, such as phosphorescence (found in specific materials like glow-in-the-dark paints or certain minerals) or iridescence (typically observed in objects with microstructured surfaces like butterfly wings or peacock feathers), are not as common in general scenes, one effect that consistently stands out and affects almost every render is *metamerism*.

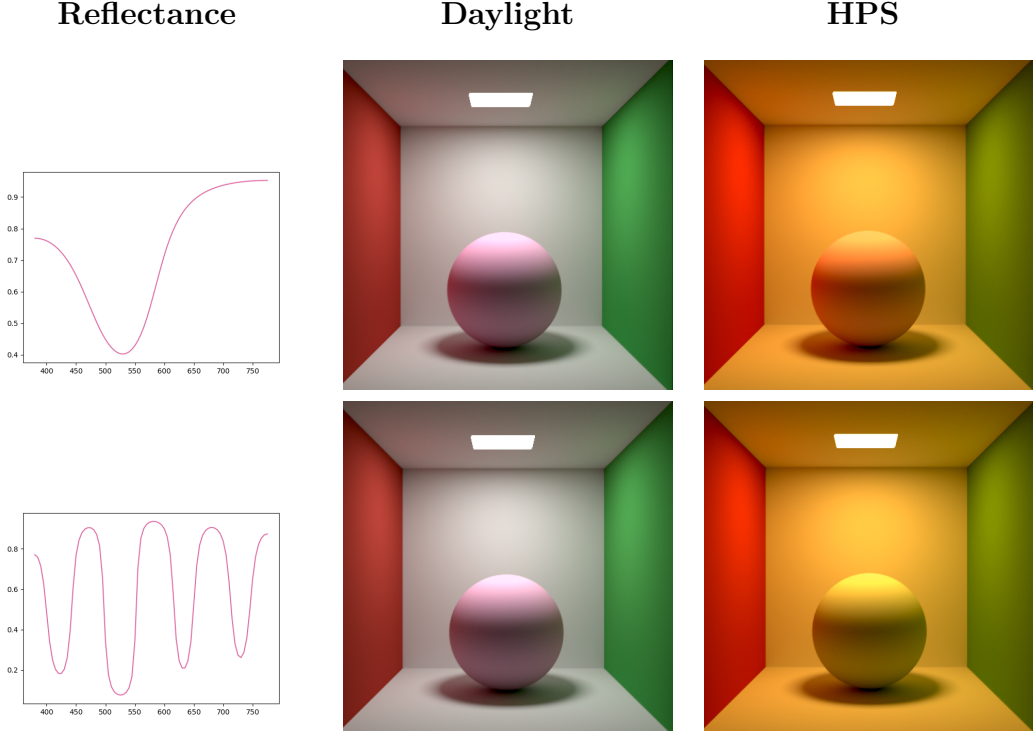


**Figure 1.8** An example of illuminant metamerism, i.e. when two objects appear identical under one illuminant while differing under a distinct one. The renders were obtained with the ART renderer (Alexander Wilkie, 2018), and the specific illuminants used are the D65 daylight and the HP2 high-pressure sodium (HPS) illuminants from the database of standard illuminants defined by CIE (CIE Technical Report, 2004).

### 1.1.5 Metamerism

The relationship between the spectral and any RGB domain is surjective, which means that multiple spectral curves can evaluate to the same RGB value. These are referred to as *metamers*.

The number of metamers that exist for an RGB value can vary depending on its position in the chromaticity diagram. For example, pure spectral colors, which are located on the spectral locus, can be produced by only a single monochromatic spectrum, and colors close to them with similarly high saturation and chromaticity generally correspond to less metamers than e.g., colors in the sRGB gamut. Additionally, while some RGB values can technically be produced by an infinitely many metamers, only a subset of them are physically realizable.

Metamerism occurs when two metamers appear identical under one condition but differ under another (Wyszecki; Stiles, 2000). The type of metamerism depends on the specific condition. For example, *observer metamerism* refers to objects being identical for one observer but having distinct appearance for another, while *geometric metamerism* arises when the same happens for different viewing conditions.

In the context of this thesis, but also more broadly within color science, the term metamerism is most commonly used to describe *illuminant metamerism*, which is where objects appear identical under one illuminating condition but differ under another. This concept can also be extended to the illuminants themselves – two

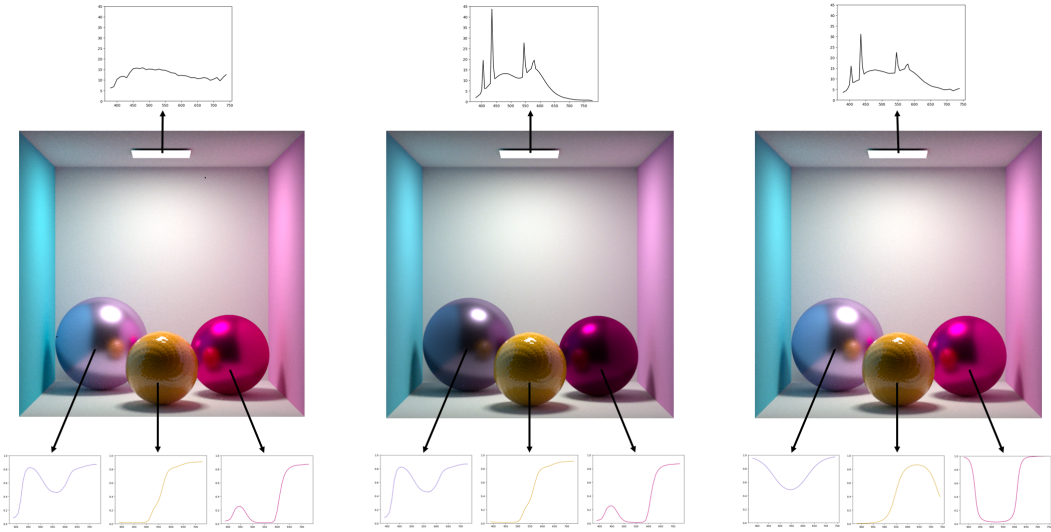


**Figure 1.9** The effects of metamerism. In all three examples, all the illuminants are metamers, which also applies to the material properties of the respective objects.

illuminants are considered metameric if they cause one object to appear identical under both of them, but trigger perceptual differences for other objects.

We show an example of metamerism in Figures 1.8 and 1.9. While Figure 1.8 depicts a scenario where only the reflectance properties of objects are metameric, Figure 1.9 illustrates multiple setups with both the illuminants and the respective object properties being metameric.

The phenomenon of metamerism motivates this thesis in two ways. First, the perceptual differences that arise due to it emphasize the necessity of spectral rendering, as an accurate reproduction of such effects is not possible in an RGB-based renderer. Second, within the context of spectral rendering, it highlights the importance of representing material properties with their real-life counterparts as opposed to arbitrarily chosen metamers.

## 1.2 Spectral Uplifting

While the increased memory and performance requirements pose general technical challenges in spectral rendering, an additional obstacle to adopting such a pipeline in production environments is the limited availability of spectral assets. This includes the spectral definitions of materials and textures, their reflectance, absorption, and transmission properties, the emission spectra of light sources, and virtually all other components necessary for constructing a complete physically accurate scene.

One way to obtain such assets is through spectral measurements. These need to be performed manually with professional-grade equipment, such as a spectrometer or, in the case of full-scene captures, with a specialized spectral camera. In addition to the equipment involved, this process is typically tedious and time-consuming. Moreover, it requires the prolonged availability of a real-life counterpart of the object in the scene. In case of, for example, animals, this is extremely impractical. The same applies to objects in outdoor environments, as even a small change of environmental factors can compromise the accuracy of the measured data. Finally,

in the case of work in the VFX industry, measurements are often not even a possibility, as the workflows typically involve rendering fantasy creatures or other imaginary objects with no real-life counterparts.

Therefore, another option is to create the assets in the spectral domain. This entails manually modeling a spectrum that evaluates to the desired RGB value. However, this approach is rarely employed. First, it requires a lot of specialized and time-consuming work for the artists, who generally do not have sufficient knowledge of the spectral domain. And even if they did, the color space remains the more intuitive and efficient domain for asset creation, allowing the use of familiar color mixing tools and established workflows. Another major factor that discourages manual spectral modeling is the fact that a lot of RGB assets already exist, and that their recreation would be considerably resource-intensive.

Therefore, the general approach to obtaining spectral assets is by creating them in the RGB color space and performing their conversion into the spectral domain – with a process called *spectral uplifting*. We note that in other works, the process is also referred to as *spectral upsampling*.

### 1.2.1 Requirements

Designing a spectral uplifting system has distinct constraints and poses multiple challenges. We summarize them in the following:

**Round-trip Error.** One of the most important properties of any uplifting technique is the round-trip error that it is capable of achieving. This refers to the error between the input RGB value and the RGB value that the uplifted spectrum evaluates to. Since it inherently cannot be 0 (as the conversion from a spectral representation into a tristimulus value, as specified in Equation 1.2, is only an approximation), the general goal is for it to be negligible to the human eye. As shown by Mokrzycki and Tatol (2011), this translates to aiming for  $\Delta E \leq 1$ , which is also the goal the techniques proposed in this thesis strive to achieve.



**Figure 1.10** Two spectral renders of the same scene with distinct uplifting methods applied to the same RGB HDR environment map – a physically based approach (**left**) and an uplifting technique that achieves smooth shapes (**right**). The differences are rather significant, which highlights the importance of using a physically accurate approach capable of simulating real-world behavior.

**Boundary Constraints.** In order to preserve physical plausibility of the resulting spectra, the boundaries of their individual values must be maintained. First, practically all spectra must remain non-negative for every wavelength. The upper bound then depends on their type – for example, while reflectance and transmission spectra are limited to values between 0 and 1, emission spectra, in theory, have no upper limit.

Generally, the focus of most spectral uplifting techniques is on *reflectance spectra*. However, in practice, all of these methods can, in the same manner, be applied to the uplifting of transmission or absorption due to identical boundary requirements. This is also often taken advantage of in production environments.

**Spectral Shape.** Due to metamerism, the process of spectral uplifting is significantly underconstrained, as, even after satisfying both the round-trip error and boundary requirements, most RGB values can uplift to a wide variety of physically plausible options. When designing a general uplifting technique for a whole color gamut that provides a single uplift for every RGB value, it is usually preferred that the resulting shapes be smooth and simple to resemble the shapes typically occurring in nature (such as reflectance of vegetation, wood, or even emission of daylight illumination). An additional advantage of such approach is its reduced susceptibility to metamer artifacts, meaning the appearance of color gradients remains consistent under different lighting conditions.

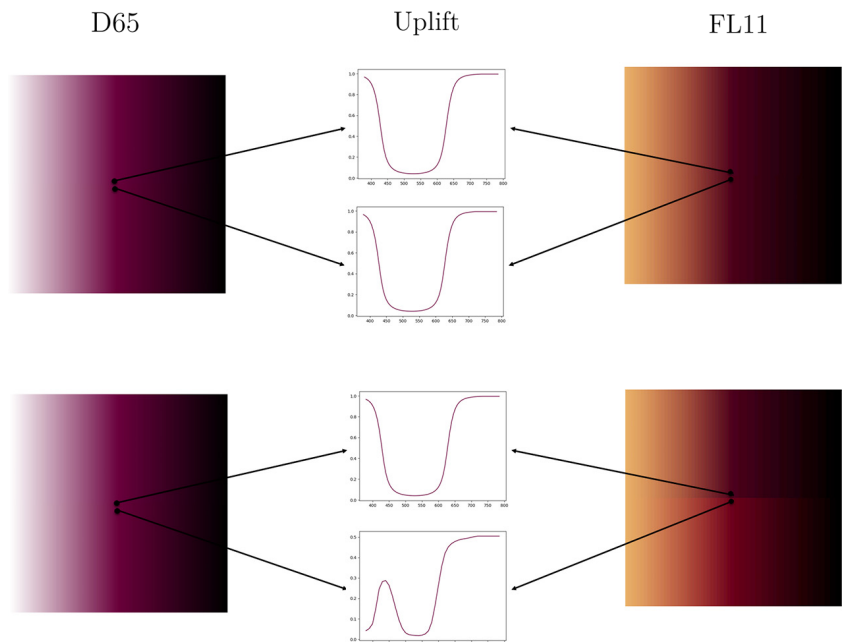


**Figure 1.11** Importance of shape consistency when designing an uplifting method. While in the top row, colors in close proximity to one another uplift to similar shapes, the uplifting method employed in the second row uses a rather distinct metamer. Although this does not cause noticeable differences when rendering under a daylight illuminant, the gradient breaks down significantly for a fluorescent light source. The specific illuminants used are the CIE standard illuminants D65 and FL11 (CIE Technical Report, 2004).

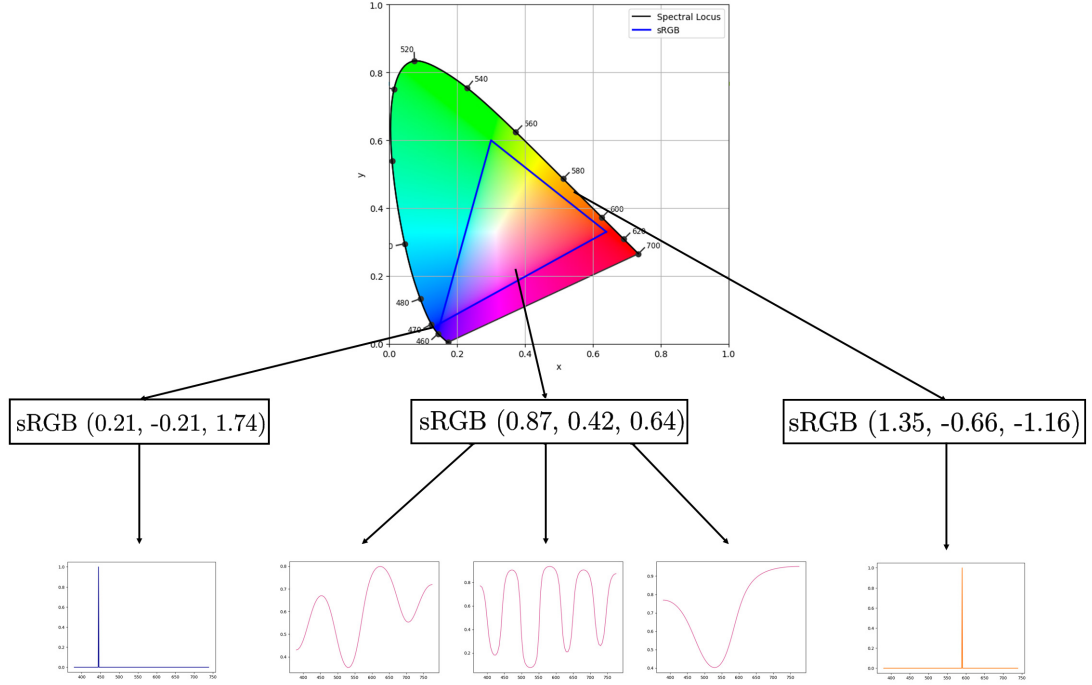


**Figure 1.12** Examples of metamers that correspond to individual colors shown in the chromaticity diagram. While colors on the spectral locus can only be achieved by a single spectrum, less saturated colors in the sRGB gamut may be produced by a wide variety of metamers.

However, in cases where the input RGB belongs to an object with a more complex and spiky spectrum (such as fabrics, dyes, or indoor LED or fluorescent illuminants), the preservation of such artifacts is one of the primary benefits of using a spectral renderer. Therefore, a corresponding uplifting technique should be employed.

We provide an example of the possible metamer artifacts that can be caused by distinct uplifting techniques in Figure 1.10. In addition to it emphasizing the need to focus on the shapes of the final spectra, it also highlights the insufficiency of having only a single uplifting method that provides only bijective mappings, i.e. where an RGB value uplifts to the same spectrum regardless of the context.

**Shape Consistency.** In specific cases, it may be desired that a particular color region uplifts to certain spectral shapes – for example, if a scene contains a distinct yellow dye, there might be a preference for colors in that part of the gamut to uplift to complex, spiky spectra that reflect it, while the rest of the gamut should attain smooth curves that correspond to the rest of the scene’s environment.

However, if RGB values in close proximity to one another uplift to significantly distinct spectral shapes, this may lead to undesirable metamer artifacts under varying illumination. An example of this can be seen in Figure 1.11, where we show the effect of two distinct uplifting techniques on a color gradient. This aspect can be especially problematic when designing uplifting techniques for wider color gamuts, as the colors nearing the edges

of the spectral locus correspond to only a limited number of metamers, all of which are rather spiky and blocky (see Figure 1.12).

**Performance.** While in some cases, renderers are capable of preloading the scene’s assets into memory and performing their uplifting prior to the start of light transport, the general preference is to carry out the uplifting on the fly, i.e. upon every light interaction with a material. While this significantly saves memory, it also places additional demands on the performance and efficiency of the techniques.

### 1.2.2 Existing Methods

When the need for spectral uplifting was first recognized, the goal of the initial techniques was to simply create a solution that would enable the use of general RGB textures in a spectral renderer while satisfying the mandatory round-trip error and boundary constraints. This essentially translated to methods that provide bijective mappings from the RGB to the spectral domain for a sufficiently large color gamut. The quality of the results was also assessed by the smoothness of the spectra, both in order to be similar to typical material properties in nature and to prevent unnecessary metamer artifacts.

As this was shown to be a rather complicated task, multiple approaches were developed, each tackling the problem from a slightly different perspective. We start this section by providing their brief review – while for more thorough information, we refer the reader to the overview by Weidlich et al. (2021) and to the individual publications. As the focus of the initial methods was primarily on reflectance data, mainly due to the scarcity of emissive assets that required immediate support, we then follow up with a discussion on the current state of the art for emission uplifting. Lastly, novel techniques that also focus on other aspects of uplifting (such as spectral shapes and metamerism) are reviewed.

#### General Bijective Methods

The first technique for spectral uplifting was proposed by **MacAdam (1935)**. Although it supported the full color gamut, it relied on the so-called *MacAdam spectra*, which are box-shaped and therefore do not correspond to real-world material properties.

The technique by **Glassner (1989)** addresses this with a method that starts with a physically implausible spectrum defined for only three wavelengths, and iteratively smooths it out over the visible wavelength range. However, the results can attain negative values, which does not satisfy the lower boundary constraint. Additionally, while smoothness is improved in contrast to MacAdam spectra, the results are still prone to staircasing.

A technique widely used in the early days of commercial spectral renderers, such as Manuka (Fascione et al., 2018), was proposed by **Smits (1999)**. Based on a set of seven predefined spectra that consist of 10 samples, an arbitrary RGB value is uplifted by using a simple optimization algorithm that searches for the most suitable combination. While the method is both fast and takes physical plausibility into account, it becomes unstable for gamuts wider than sRGB. Additionally, in

specific cases, it is prone to breaking the upper bound constraint on reflectance spectra, which, in turn, results in round-trip errors.

To handle the full gamut of realizable reflectance, **Meng et al. (2015)** propose another method based on predefined spectra and their optimization. Specifically, the set of spectra spans the xy-chromaticity plane, and a smoothness constraint is introduced in order to avoid blocky results. However, values above or below the plane require scaling, which introduces round-trip errors even in the sRGB gamut. **Otsu et al. (2018)** also base their method on the xy-chromaticity plane. In their case, they propose dividing it into clusters that contain localized bases for spectral recovery. However, while efficient and suitable for indirect illumination, the method leads to discontinuities at cluster boundaries, resulting in poor color gradient transitions.

A technique that can be considered state of the art for general reflectance uplifting was introduced by **Jakob and Hanika (2019)**. In their work, they propose a low-dimensional parametric model for spectral representation, which stores spectra with only 3 floating point coefficients and follows:

$$f(\lambda) = S(c_0\lambda^2 + c_1\lambda + c_2)$$

where  $c_i$  are the coefficients of a second-order polynomial that are used to represent the spectrum,  $f(\lambda)$  is the resulting spectrum, and  $S$  is a simple sigmoid function defined as follows:

$$S(x) = \frac{1}{2} + \frac{x}{2\sqrt{1+x^2}}$$

The simplicity of the representation allows the construction of a full sRGB uplifting model, which contains a set of mappings from RGB values to their respective coefficients. An arbitrary RGB value is then uplifted by a lookup in the model and, if needed, by an interpolation of the closest mappings in the model. While in the original paper, the model is stored in 3 distinct cubes of resolution  $64^3$  that collectively make up the sRGB gamut, more recent implementations, such as the one in the Mitsuba 3 renderer (Jakob; Speierer, et al., 2022), only use one sRGB cube of resolution  $32^3$ . We also utilize the cube-based model as a basis of our work (see both Chapter 2 and Chapter 3).

The spectra constructed in this manner are smooth and simple, which corresponds to typical material properties found in nature. The method does not introduce discontinuity errors for color gradients, and the results satisfy the  $[0, 1]$  boundary constraints of reflectance data.

The main downside to using this technique is its performance overhead – finding an accurate coefficient representation for an input RGB requires running an optimization algorithm, which is too computationally expensive to execute during light transport. Therefore, the entire model must be precomputed beforehand, which implies the need for its storage and easy access on every light interaction with a material.

Another limitation is its target color gamut, which, in the original publication, is only the sRGB gamut. This is later extended to wider range in the works by **Jung et al. (2019)** and the extension by **König et al. (2020)**. The tendency of highly saturated RGB values to uplift to blocky shapes is addressed by adding fluorescent components to the original method by Jakob and Hanika, thus resulting

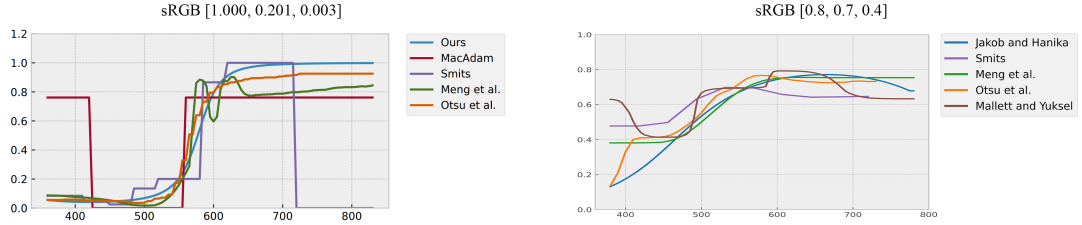


**Figure 1.13** Examples of different general reflectance uplifting techniques when applied to two distinct sRGB values. The first example (**left**) is taken from the work of Jakob and Hanika (2019) (i.e. label *Ours* corresponds to their technique), while the second (**right**) was generated using the implementations of the uplifting methods provided by Python’s Colour library (2013).

in smoother shapes. Another gamut extension is also proposed as a part of our work (see Chapter 2).

The wide use of this method for general reflectance uplifting prompted the exploration of other optimization-based techniques. The main motivation was the need for the uplifting of more complex, yet still physically plausible shapes, such as the reflectances of saturated fabrics or emission spectra of spiky indoor illuminants like LEDs or fluorescent lamps.

This led to the technique introduced by Peters et al. (2019b). In their work, they propose a method for storage and a subsequent reconstruction of spectra with trigonometric moments. The number of needed moments (or *coefficients*) is based on the complexity of the spectral shape along with the desired color accuracy, ranging from 3 for general reflectance spectra up to over 31 for extremely complex emission. This representation is, in a similar manner to the method by Jakob and Hanika, used to store RGB to spectra mappings in an evenly divided sRGB cube that is then utilized during the uplifting.

The proposed implementation demonstrates inferior runtime performance compared to the method by Jakob and Hanika. Additionally, the uplifts are also only arbitrary spectral shapes (that are based on only the number of used moments), which, at first glance, shows no improvement over the previous methods. However, we note the significant potential of the proposed spectral representation. In addition to it being capable of covering the full gamut of realizable reflectances (as opposed to only sRGB), it is variable enough to reconstruct almost any real-life spectral measurement. The novel capabilities of such representation are also later used in our work (see Subsubsection 1.2.3 and Chapter 2), where storage of specific spectral shapes is imperative.

The latest research in the field of general reflectance uplifting was proposed by Mallett and Yuksel (2019) and Burns (2020). Both techniques create spectra as a linear combination of three predefined spectral response curves (or primaries). However, the achieved spectral shapes are inferior to the ones proposed by Jakob and Hanika. In case of the method by Mallet and Yuksel, this is caused by the lack of a smoothness constraint, which results in the presence of box-like artifacts. The technique by Burns, on the other hand, is prone to staircasing. As such, these contributions are best regarded as theoretical explorations of distinct spectral bases.

In Figure 1.13, we present an illustration of the spectral shapes that some of the

reviewed techniques achieve by uplifting two distinct sRGB values. Note that, technically, not all of the shown spectra are perfect metamers, as some of the methods are prone to round-trip errors.

## Emission Uplifting

The emphasis on designing only reflectance uplifting methods was primarily driven by the scarcity of emissive assets in typical rendering workflows. The main light sources of the scene are still generally either measured manually, or their spectral power distribution is obtained from known databases of illumination spectra.

Still, a basic support for emission uplifting was required. While this was also aimed at handling specific emissive textures used mainly in the VFX industry (e.g., glowing skin of fantasy creatures), as well as unconventionally colored light sources, one of the primary use cases was image-based lighting, i.e. HDR environment maps.

In the context of computer graphics, environment maps are special types of textures used to simulate surrounding lighting in a scene (Pharr et al., 2023). Unlike traditional light sources that exist at a specific point in space, an environment map surrounds the entire scene and is conceptually placed at infinity. Each pixel in the map acts as a distinct, parallax-free emitter, contributing to the overall illumination from all directions.

Environment maps are typically created as 360° panoramic HDR (High Dynamic Range) images, either by performing specialized photographs or by digital drawings. Unlike standard LDR (Low Dynamic Range) images, whose RGB values are bounded by 0 and 1, the high dynamic range has the ability to represent a much wider spectrum of luminance levels. This allows the capture of emission properties, which is one of the primary reasons why HDR is used in image-based lighting.

In order to support HDR assets in spectral renderers, the only option currently available is first downscaling the input HDR RGB values into the [0, 1] range, employing a general reflectance uplifting technique, and scaling the results back to obtain the final emission. This approach can be considered the current state of the art and is also used for general emission uplifting in modern spectral renderers – for example, the Manuka renderer scales the spectra obtained by Smits (Fascione et al., 2018), while the Mitsuba 3 renderer adopts the reflectance uplifting method by Jakob and Hanika (Jakob; Speierer, et al., 2022). In order to avoid blocky shapes that can be present when uplifting at the edges of the color gamut, the Mitsuba 3 renderer (Jakob; Speierer, et al., 2022) additionally derives the scaling factor from the original input HDR  $rgb$  value as follows:

$$scale = 2 \cdot max(rgb.r, rgb.g, rgb.b)$$

which results in the reflectance spectra being obtained from the central region of the sRGB cube.

The scaling of reflectance spectra, however, can lead to physically unrealistic results, as real-life emission tends to contain more spiky and blocky features. Therefore, **Guarnera et al. (2022)** propose a method for uplifting illumination that uses a basis of six spectral distributions and obtains the uplift as their convex combination. Although originally corresponding to LED light sources, the method also works with other spectral bases, including Gaussian functions also evaluated as

part of the paper. While the results are satisfactory for multiple application areas, the input is still only an RGB value, which provides no information about the desired spectral shape and therefore about which basis should be used. Choosing one that does not correspond to the real-life counterpart of the scene is, once again, prone to result in metameric artifacts.

## Other Methods

Despite certain limitations in the achieved spectral shapes, the proposed techniques effectively enabled uplifting of practically any type of input RGB asset while satisfying the mandatory uplifting requirements – that is, the round-trip error and boundary constraints. This allowed research to progress beyond the problem of general uplifting and focus on more specific challenges. One of them included the issue of metamericism, which is prone to arise when using a method that provides only one-to-one mappings. As a result, more recent techniques turned their focus on the appearance of the uplift under differing illuminants in order to either prevent metameric artifacts, or to deliberately achieve a specific appearance under particular lighting conditions.

**Belcour et al. (2023)** propose a so-called *one-to-many* method that uplifts a single RGB value to a family of metamers. Building from a small set of basis functions, the technique computes a class of basis coefficients which reconstruct spectra with the chromaticity and luminance of the input RGB value. The primary application examined by the paper is the recreation of the Usambara effect, which is the color change induced by variations in the path length traveled by light, typically observed in gemstones. While the paper also presents a way in which to use the technique to reproduce metamericism, its practical applicability in a spectral renderer is limited due to, once again, the underconstrained nature of the spectral uplifting process – without additional information, the renderer does not know which metamer to uplift to.

**Van De Ruit and Eisemann (2023)** address this by additionally allowing the user to define texture appearance under various lighting conditions. The result is then a space of possible metameric manipulations, with interactive adjustments enabled so the user can obtain the most suitable spectrum while still satisfying the constraints. Direct uplifting is also supported by interpolation of the inferred metamers. Despite the exhibited limitations of the method (such as the possible omission of specific uplifts from the output set, and the high dependency on the proper specification of the also limited user input), the results represent a meaningful advancement in the field. We note that, while the addressed problem is not identical to that of our work (see later in Subsubsection 1.2.3, or alternatively in Chapter 2), it was published following our contribution.

In addition to the proposed methods, production pipelines also develop targeted techniques in order to improve the uplifting of specific material categories. While these usually consist of only a lookup table containing a large dataset of obtained spectral measurements that are interpolated to determine the final uplift, certain materials have received more attention by applying more advanced approaches, such as neural networks and deep learning techniques.

A notable example is the work by Aliaga et al. (2023), which returns the spectral volume properties of skin layers upon an input albedo, effectively performing physically plausible skin uplifting. Techniques based on deep learning are also

popular when applied to the problem of data reconstruction for hyperspectral imaging (see overview by J. Zhang et al., 2022).

Lastly, as our Master’s thesis (Tódová, 2021) and a subsequent conference publication (Tódová; Wilkie; Fascione, 2021), we presented a novel technique capable of constrained reflectance uplifting. As this method serves as the basis for the contributions in this thesis, we provide a more thorough summary in the following.

### 1.2.3 Constrained Spectral Uplifting

Generally, scenes rendered for use in the VFX or even the product manufacturing industry are primarily comprised of objects that simulate naturally occurring materials, such as wood, vegetation, rocks, etc. As their reflectance spectra are usually smooth and simple, a significant portion of an input scene would therefore typically benefit from utilizing an uplifting technique with similar results – such as, for example, the method by Jakob and Hanika (2019), or even a variant of the technique by Peters et al. (2019b) that uses a low number of coefficients. In such cases, slight discrepancies between the uplifts and their real-life counterparts are generally negligible due to the smoothness of the spectra, especially if the affected objects do not occupy the majority of the scene.

However, in scenarios where such objects either dominate the viewport or exhibit more complex reflectance properties, preserving the exact spectral shape becomes significantly more important for physically accurate color simulation. In our example in product manufacturing and the VFX industry, this could regard brightly colored sheets in an architectural visualization of a bedroom, or a superhero costume with three distinct, saturated colors that are prone to metamerism under indoor fluorescent illumination.

For such cases, it would be valuable if specifically this set of colors uplifted to the desired spectral shapes, and the rest of the gamut achieved smooth reflectances. This motivates the idea of *constrained uplifting*. Its premise is as follows:

The input to the uplifting system is a set of *constraints* – i.e. predefined spectra that must be preserved. These are supplied by the user, either through manual measurements or by obtaining them from an existing dataset. Based on the constraints, an uplifting model similar to one proposed by Jakob and Hanika (2019) is created. Specifically, the model is an sRGB cube with evenly-spaced lattice points which contain mappings from their respective coordinates (or RGB values) to spectra. As opposed to the 3-coefficient sigmoid model used by Jakob and Hanika, the representation by Peters et al. (2019b) is adopted due to its greater flexibility in terms of the supported spectral shapes. The number of coefficients used to represent a given spectrum is determined heuristically based on its complexity.

In the beginning, the cube is populated only with the mappings specified by the constraints. The remaining entries are then obtained in an iterative manner using an optimization algorithm – to determine the spectrum of a specific lattice point, the method optimizes the coefficients of its already-resolved neighbor to find the most similar shape that evaluates to the desired RGB value. This implies that the cube effectively “grows” from the positions of the constraints.

By prioritizing the preservation of spectral features when moving away from the constraints, the optimization algorithm limits the possibility of a gradient

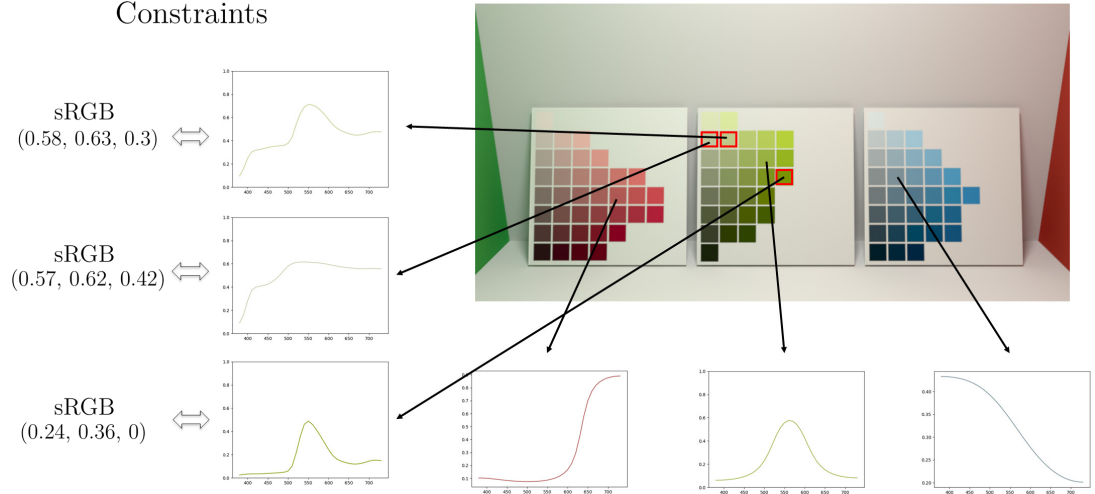


**Figure 1.14** The results of constrained uplifting in the sRGB gamut. The RGB values of the three constraints (the three highlighted patches of the green page of the Munsell Book of Color) uplift to the specified shapes with a high degree of accuracy, while the unconstrained RGB values attain smooth and simple spectra. Also note the uplift of the green unconstrained patch – while the spectrum also exhibits smoothness, the shape is close to that of the last constraint, which aids in prevention of gradient discontinuities.

discontinuity (such as the one shown in Figure 1.11) occurring. Additional benefit of such approach is the mitigation of floating point errors when uplifting the constrained RGB values – for example, if a specific yellow superhero costume is captured by a camera and used as a texture for uplifting, it is highly unlikely that its captured RGB value is going to be identical to the RGB value obtained by conversion from spectral measurements. Uplifting to an extremely similar shape ensures the preservation of the desired appearance.

On the other hand, areas of the color gamut that are not affected by the constraints require simpler uplifts. This is achieved by lowering the number of coefficients of the moment-based representation in these areas to only 3, which inherently lacks the capability to represent complex shapes. As a result, RGB values that are far from the constraints are uplifted to smooth and simple spectra.

We show an example of constrained uplifting as proposed by our early work in Figure 1.14. For additional examples and more thorough explanation of the algorithm, we refer the reader to the original paper and thesis.

While the initially proposed technique was novel in its capability to constrain the uplifting process, it exhibits several limitations and areas for improvement. The first and foremost is its support of the sRGB gamut only. This is because colors in the sRGB gamut typically correspond to smooth and simple spectra and are therefore generally not subject to metamerism. This additionally limits the ability to properly evaluate the method, as the input constraints are already rather smooth to begin with.

This motivates the first contribution of this doctoral thesis, which is a constrained uplifting method that is able to support any RGB gamut from within the gamut of realizable reflectances.

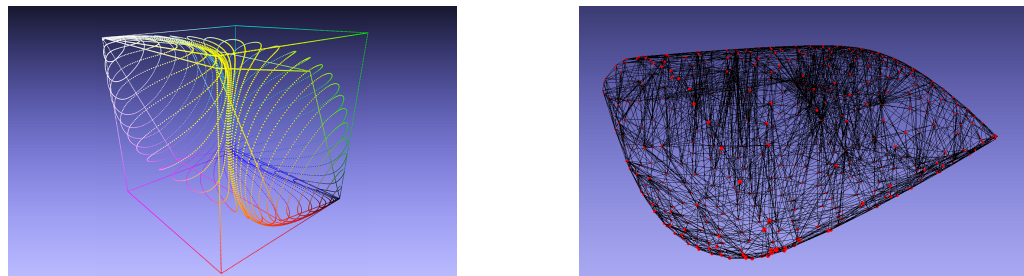
## 2 Wide Gamut Constrained Spectral Uplifting

The first contribution of this thesis is the extension of the previously proposed sRGB constrained uplifting method (see Subsection 1.2.3 of Chapter 1) for the support of wider color gamuts. This poses multiple challenges. The main one lies in the data structure used for the uplifting model – while the physically realizable colors in the sRGB gamut make up the entire sRGB cube, for wider gamuts, such as the gamut of realizable reflectances or even e.g., the Adobe Wide Gamut RGB gamut, their subset of physically realizable colors forms a blob-like shape that does not have such a precise definition (see Figure 2.1a).

A notable part of our work therefore consisted of researching the data structures suitable for such a problem. The explored approaches were primarily based on the idea of sampling the gamut boundary, and using the samples as additional constraints of the uplifting system. Along with the user input, these would be the only mappings stored, which would eliminate the need for executing an optimization process to determine the mappings for arbitrary lattice points. Overall, the uplifting model would therefore be comprised of tetrahedra within which the uplifting could take place (see visualization in Figure 2.1b).

However, this idea, along with other approaches based on similar principles, was subject to multiple concerns. The primary issue lied in the quality of the spectra resulting from the interpolation within the structure. While in the sRGB cube model, the lattice points are in close proximity and generally contain similar spectral shapes, less densely sampled structures are inherently subject to the possibility of interpolating uplifts from different parts of the color gamut. Including the spiky spectra at the gamut boundary and the potential complexity of the constraints, the results of such an interpolation are prone to attain shapes that are both physically inaccurate and also likely to cause gradient discontinuities.

The possibility of interpolating in a different space used for spectral representation – such as interpolating trigonometric moments or even the sigmoid coefficients – has



(a) The gamut of realizable reflectances visualized with the sRGB and the wrGB cubes. The image is obtained from the extended publication (Tódová; Wilkie; Fascione, 2022).

(b) Our researched concept of the tetrahedral uplifting structure, with the samples (or constraints) on the boundary visualized in red. Note the large number of tetrahedra – this has a significant effect on the performance of the method.

**Figure 2.1** Visualization of the shape of the gamut of realizable reflectances in the 3D RGB space.

already been explored by previous works (e.g., Jakob and Hanika (2019), Peters et al. (2019b)), and while its performance is sufficient for specific cases, in general, the idea is not supported by a mathematical proof. A supplementary document on the moment-based representation research by Peters et al. (2019a) specifically addresses this, claiming that “*Binning is the only linear reconstruction that preserves non-negativity of signals*” and providing a subsequent proof. Therefore, we also emphasize the necessity of the interpolation of the reconstructed spectra as opposed to any other type of representation.

A way in which to improve the results of the interpolation is by sampling the 3D RGB space of the gamut and therefore adding additional constraints to the proposed structure. However, this gives rise to yet another problem, and that is the performance of the method. Given an input RGB value, finding the correct tetrahedron within which to interpolate has an  $\mathcal{O}(n)$  complexity, which may take a rather significant absolute execution time given the increased number of tetrahedra. While this can be optimized by employing a space-partitioning data structure, such as a k-d tree or a bounding volume hierarchy (options which we have also explored), the worst-case scenario of the lookup process may still be excessive – especially in comparison to the  $\mathcal{O}(1)$  complexity of the previously used cube. The benefits of an even sampling of the gamut space in terms of both the implementation complexity and the final interpolated spectral shapes additionally support the use of the cube structure.

As a result, our method resorts to using an RGB cube as the uplifting model, which serves as the bounding volume of the target gamut. This means that while the model does not, technically, support the full gamut of realizable reflectances, it is capable of handling any RGB color space. Therefore, although our goal of incorporating the tetrahedral structure was, in practice, unsuccessful, we still find the effort worth mentioning for any potential future attempts with a similar goal in mind. Additionally, while the inability to create a single constrained model that encompasses virtually all realizable colors can be limiting in large production environments, this design choice nevertheless offers several practical advantages. First, asset creation is typically carried out relative to a specific RGB space, which makes the full-gamut support unnecessary for most workflows. Second, it facilitates handling of color spaces whose primaries are outside of the gamut of realizable reflectances (such as ProPhoto RGB), which would be more difficult to represent using the tetrahedral-based model.

The work included provides a specific implementation for the Adobe Wide Gamut RGB (*wRGB*). However, we note that the same principle could be applied for the support of virtually any RGB color gamut.

Additional contributions of the paper include the extension of the unconstrained sRGB cube (which is based on the model by Jakob and Hanika (2019)) for wRGB support, as well as the handling of out-of-gamut values in the empty regions of the new wRGB cube. As opposed to the original method, which did not address this possibility, the extended implementation incorporates gamut mapping and thus has the capability of uplifting virtually any value within the wRGB cube, even if the uplift results in a higher round-trip error.

The method (Tódová; Wilkie; Fascione, 2022) is an extension of our previous work on constrained uplifting (Tódová, 2021 and Tódová; Wilkie; Fascione, 2021), which was published as a conference proceeding.

The full citation of the journal publication is as follows:

TÓDOVÁ, Lucia; WILKIE, Alexander; FASCIONE, Luca, 2022. Wide Gamut Moment-based Constrained Spectral Uplifting. In: *Computer Graphics Forum*. Wiley Online Library. Vol. 41, pp. 258–272. No. 6. Available from DOI: [10.1111/cgf.14617](https://doi.org/10.1111/cgf.14617).

The full journal publication is inserted and begins on the next page.

# Wide Gamut Moment-based Constrained Spectral Uplifting

L. Tódová,<sup>1</sup> A. Wilkie<sup>1</sup> and L. Fascione<sup>2,\*</sup>

<sup>1</sup>Faculty of Mathematics and Physics, Department of Software and Computer Science Education, Charles University, Prague, Czech Republic  
todova@gmail.com, wilkie@cgf.mff.cuni.cz

<sup>2</sup>NVIDIA, Santa Clara, California, USA  
l.fascione@gmail.com

## Abstract

*Spectral rendering is increasingly used in appearance-critical rendering workflows due to its ability to predict colour values under varying illuminants. However, directly modelling assets via input of spectral data is a tedious process: and if asset appearance is defined via artist-created textures, these are drawn in colour space, i.e. RGB. Converting these RGB values to equivalent spectral representations is an ambiguous problem, for which robust techniques have been proposed only comparatively recently. However, other than the resulting RGB values matching under the illuminant the RGB space is defined for (usually D65), these uplifting techniques do not provide the user with further control over the resulting spectral shape. In a recent publication, we have proposed a method for constraining the spectral uplifting process so that for a finite number of input spectra that need to be preserved, it always yields the correct uplifted spectrum for the corresponding RGB value. We extend this previous work, which supported the sRGB gamut only, by describing a method that is able to constrain any spectrum from within the gamut of realisable reflectances. Due to constraints placed on the uplifting process, target RGB values that are in close proximity to one another uplift to spectra within the same metamer family, so that textures with colour variations can be meaningfully uplifted. Renderings uplifted via our method show minimal discrepancies when compared to the original objects.*

**Keywords:** rendering, reflectance and shading models rendering

**CCS Concepts:** • Computing methodologies → Reflectance modelling

## 1. Introduction

Over the last few years, the demand for physical accuracy in rendering has grown substantially. The main advantage of providing renderers with the capability to simulate light transport in a physically accurate fashion is that one can obtain an intrinsically realistic scene appearance via global illumination. But there are also other useful capabilities of physically correct rendering, such as colour accuracy: working with spectral data allows one to predict object appearance under varying illuminations.

However, almost all VFX and game engine assets, in particular their textures and material data, are defined in RGB, as this is easier for the artists creating them. Defining genuinely spectral assets would require artists to either specify spectral reflectances from reference data collections (e.g. colour atlas data), or to measure them on a real asset with a spectrometer. Both options are more or less tedious, and the second one is not possible for fully virtual assets. Additionally, painting spectral textures is an open problem.

To make spectral rendering possible while utilising RGB textures as input, a reliable conversion from RGB to spectral data, called *spectral uplifting* (or *spectral upsampling*), is needed. However, as RGB colour spaces are intrinsically smaller than the space of all possible spectra, multiple different spectral representations of the same RGB colour, called *metamers*, exist. From a mathematical viewpoint, there are infinitely many metamers: but, in reality, the number of achievable metamers is limited by the properties of real colourants and pigments.

Typically, metamers no longer match in appearance under different light sources. This may cause issues with spectra created by current uplifting technology, which, while robust and reliable, creates arbitrary metamers. Therefore, the appearance of assets defined via RGB can be somewhat unpredictable under changing illumination.

Figure 2 shows an example of this: the Munsell Book of Colour is an old colour atlas, which was defined before fluorescent lights were common. The yellow-green pages of the atlas are known to exhibit noticeable distortions in the colour gradient of the samples when

\*Work conducted while at Weta Digital.

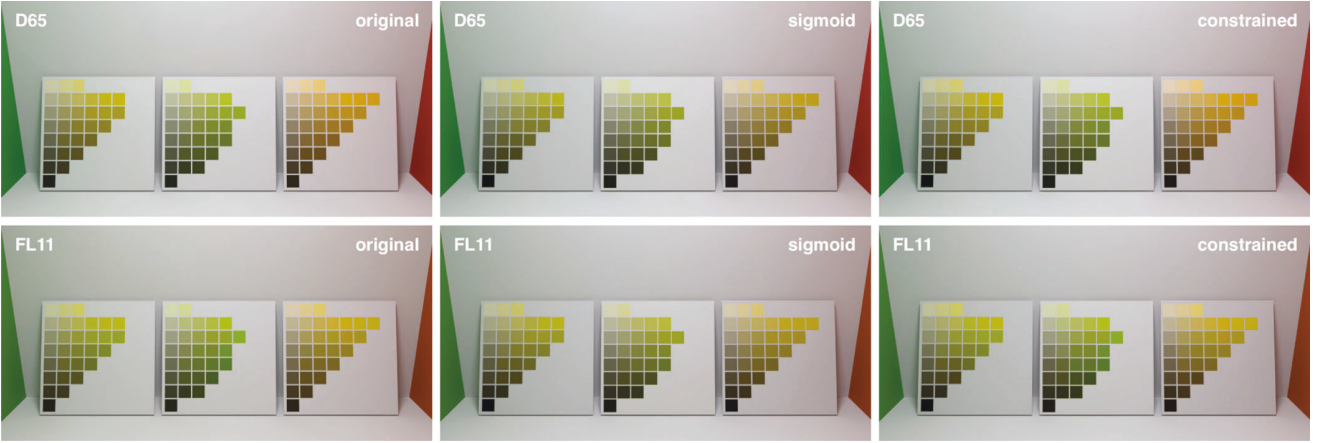


**Figure 1:** Pages from the Munsell Book of Colour under illuminant CIE D65 (top row) and CIE FL11 (bottom row). **Left column:** the materials in the scene are defined via their spectral properties, so no uplifting is needed. **Middle column:** the materials are defined as wRGB values and uplifted with the sigmoid method. Note that no metameristic failures occur in the bottom row: the colour gradient stays ordered. **Right column:** The materials are defined as wRGB values and uplifted with our method. The spectra of the Munsell Book of Colour were used to constrain the uplift: as one can see, particularly in the middle page (050GY), the spectra show the same metameristic disruptions of the colour sequence as real Munsell Book of Colour pages do. Note that white balance was applied to both sets of images.

viewed under fluorescent or LED light sources. If an RGB texture of an atlas page were used as input, a naive uplifting technique would have no chance of reproducing the fact that under one type of light source, there is a smooth gradient, while under others, the gradient breaks down.

Accurately reproducing colour atlas pages under varying illumination is of course not a very practically useful goal in itself: we merely use them as an example of a problem, which the VFX industry faces in practice. There, one must frequently deal with the task of matching plate footage of real objects with rendered images of their digitized asset counterparts. In such scenarios, it is crucial to preserve visual continuity: the viewer must not be made aware that a real asset is replaced with a virtual one. However, in order for the viewer to be oblivious to such an asset switch, not even the slightest colour differences between them must be visible.

For such work, 3D artists currently use standard colourspace modelling tools to carefully craft elaborate virtual doubles of a real asset, and obtain a perfect appearance match under the main target illumination (e.g. for daylight). If the same asset is later used in another scene with different illumination (e.g. fluorescent lamps, in an indoor setting), the entire virtual asset appearance has to be manually fine-tuned again. Such a process is, as expected, both tedious and time-consuming.

If the virtual double were modelled using spectral data, appearance continuity under varying illumination would be guaranteed in a spectral rendering system: but, as stated earlier, artists cannot easily work with spectral data directly. Even though the core rendering technology in the VFX industry is now moving towards spectral systems, asset textures will continue to be painted in colour space, as this is the intuitive way for artists to perform such work.

In previous work [TWF21], we proposed an uplifting method that allowed sRGB textures to be uplifted so that user-selected key sRGB colours would evaluate to pre-measured spectra. We termed these pre-defined mappings between specific sRGB colours and spectra of the *constraints* of the uplifting system. Using this approach, sRGB colours in close vicinity to the constraints uplift to spectral shapes similar to the original, so that minor texture edits in terms of sRGB colour difference do not cause noticeable visual distortions. All the other parts of the sRGB space return plausible, smooth spectra. This offers the new functionality of exact appearance match of renders with plate footage under varying illumination, and thereby eliminates a substantial amount of tedious appearance fine-tuning work.

However, while our previous publication proved that the basic approach works, and its contribution was valuable insofar as we addressed a problem with no previous solution, it was capable of uplifting within the sRGB gamut only. But in order to fully utilize our approach in the VFX industry, we must be able to constrain any value within the gamut of realisable reflectances.

In this paper, we extend our previous publication by addressing this aspect. We propose a method supporting larger gamuts, and demonstrate it on Adobe Wide Gamut RGB. We describe the technical challenges this extension poses, and discuss possible solutions. Our approach exhibits similar performance as in our previous work, with the additional benefit of providing implicit gamut mapping even outside the gamut of realisable reflectances, i.e. plausibly uplifting all values within Adobe Wide Gamut RGB.

Furthermore, we perform an extended evaluation of our method, which now also explores the behaviour of constraints that previously had to be omitted due to sRGB limitations. These include saturated colours along with colours from the edges of the chromaticity diagram. Even for values such as these, the performance of our method is satisfactory.

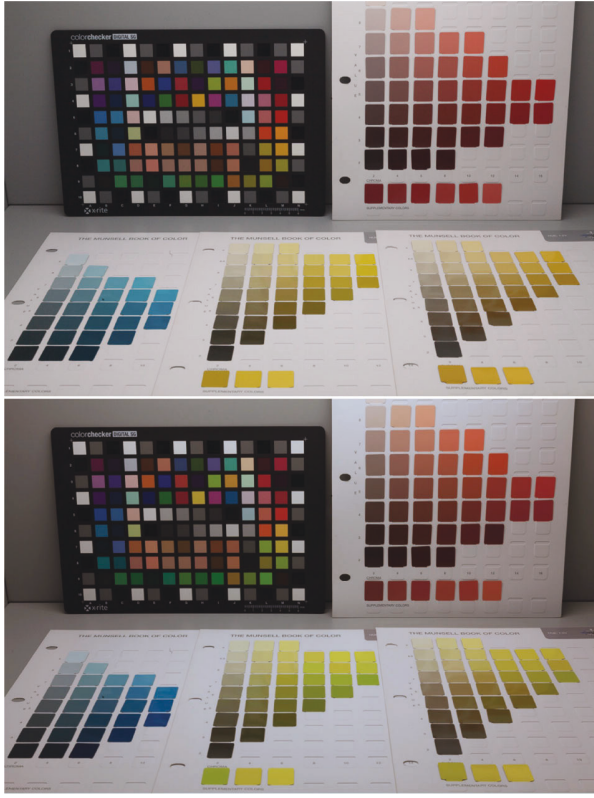


**Figure 2:** Photos of four Munsell Book of Colour pages (050B, 075Y, 100Y and 075R) in an xRite Judge QC viewing booth. **Top:** daylight. **Bottom:** fluorescent light. The photos are white balanced so that the neutral patches on the colour checker match. Note the distortions in the colour gradient on the yellow pages under fluorescent light: this same sort of effect can also be seen in Figure 1, in the images obtained with our uplifting.

## 2. Previous Work

There are two areas of prior work relevant to our technique: spectral uplifting itself, and efficient representations of spectral shapes.

### 2.1. Spectral uplifting

The reflectance spectra created by a spectral uplifting process need to satisfy multiple constraints. Their values should fall within the [0,1] range, the round-trip error caused by uplift and subsequent conversion to RGB should be negligible, and the resulting spectral shapes should qualitatively correspond to real-life materials, which are generally smooth and simple.

Although multiple techniques for spectral uplifting exist, not all of them satisfy the listed criteria. They also differ in the RGB gamut they are capable of uplifting with negligible error, and the round-trip error they obtain both outside of this gamut.

The technique by MacAdam [Mac35] is capable of creating only blocky spectra, which are not representative of the smooth re-

flectances usually found in nature. The widely used proposal by Smits [Smi99] is prone to small round-trip errors, which arise from slightly out-of-range spectra: the process is based on a set of blocky basis functions, and the result is, while usually fairly close, not guaranteed to be in the [0,1] range. While the errors are usually not perceivable for the sRGB gamut, these inaccuracies are accentuated when uplifting other RGB values and the method is rendered unstable for larger gamuts.

One of the first approaches which both produced smooth spectra and also adequately uplifted larger gamuts was proposed by Meng *et al.* [MSHD15]. However, since the spectra were created without taking energy conservation into account, they had to be rescaled in order to reproduce colours with real physical counterparts. This resulted in colour shift, and therefore, round-trip errors. Otsu *et al.* [OYH18] introduced a technique that is capable of outperforming most of the existing approaches under specific conditions. Its drawback is its inability to satisfy the [0,1] spectral range restrictions, which again causes colour errors upon round trips and a subsequent inability to correctly uplift larger gamuts.

Our method builds mainly on the technique proposed by Jakob and Hanika [JH19], which utilizes a low-dimensional parametric model for spectral representation in order to create a pre-built uplifting model, which can then be employed during rendering. The structure of the uplifting model is a cube-shaped 3D lookup table, consisting of evenly spaced lattice points representing RGB values. Each of the points contains a mapping to its respective spectral representation, which in the model by Jakob and Hanika consists of three sigmoid coefficients. The acquisition of the coefficient sets for individual points is performed during the creation of the model by an optimisation tool, CERES solver [AM\*]. Requiring only a set of prior coefficients and the definition of functions which to minimize (in case of Jakob and Hanika, the difference between the reconstructed and the target RGB), the CERES solver is capable of modifying the coefficients to the point where they reconstruct a spectrum that evaluates to the desired RGB value. This process is referred to as lattice point *fitting*. Jakob and Hanika [JH19] initially fit the coefficients for the centre of the cube (i.e. the lattice point with  $RGB = (0.5, 0.5, 0.5)$ ), and let the fitting process gradually fill in all lattice points by using the coefficients of already fitted neighbours as prior for non-fitted points. Their approach is targeted for uplifting the sRGB gamut and produces smooth spectra that satisfy spectral range restrictions with negligible round-trip error for the sRGB gamut, and acceptable error for a variety of other colour spaces. Jung *et al.* [JWH\*19] further improve this technique for wide gamut spectral uplifting by introducing new parameters for fluorescence.

None of the existing techniques, however, propose a way in which to constrain the uplifting process to deliver specific spectral shapes, and they also cannot trivially be extended in this direction. The main obstacle is that their spectral representations are simple, and unable to reproduce all possible user-defined spectra.

### 2.2. Moment-based spectral representation

A trivial way to store spectral information is via regular sampling. While being easy to implement and handle, this approach is not very

efficient in terms of memory utilisation, especially when high accuracy is desired.

The simple and smooth shapes of most real-life reflectance spectra indicate that using a lower-dimensional linear function space, such as the Fourier series, could be the key to their reliably efficient storage. Techniques based on this observation have been studied for representation of both emission spectra [RVHN03] and reflectance spectra. However, as stated by Peters *et al.* [PMHD19], although the round-trip accuracy for reflectance spectra is reasonably satisfactory, the resulting spectra do not always have a physical counterpart, as the reconstruction does not obey the  $[0,1]$  restriction needed for physically plausible reflectance spectra.

In addition to linear function spaces, non-linear approaches to spectral representations have also been proposed. These representations are, however, incompatible with linear pre-filtering of textures [PMHD19].

To eliminate these shortcomings, Peters *et al.* [PMHD19] proposed a novel approach to spectral representation. While their representation uses Fourier coefficients (which makes it compatible with linear filtering), the reconstruction is based on the theory of moments (i.e. it is non-linear in that regard). We base our work on this approach, and discuss it in more detail in Sections 3.1 and 3.2.

### 2.3. Gamut mapping

As opposed to the sRGB gamut, wide gamut RGB spaces contain values that cannot be realized as reflectances and therefore cannot be uplifted to viable reflectance spectra that would evaluate to their respective RGB values. In order to support the uplifting of such values, they must first be mapped into the gamut.

Gamut mapping is the process of modifying colour values to become displayable in a given limited target colour space. To do so, multiple methods exist: in the context of ICC profiles [Int10], these are referred to as *rendering intents*. They differ not only in their approach towards the out-of-gamut values, but some also affect the overall appearance of the entire image.

A *perceptual* rendering intent scales the entire source colour space in order to match the destination space. While this preserves the relative visual relationships between the colours, the resulting image is often noticeably less saturated than the source. The *saturation* rendering intent works in a similar manner, it also enhances the saturation of the new colours in order to provide more vibrant results.

*Colorimetric* rendering intents, on the other hand, only modify out-of-gamut values—although strictly speaking, this is only true with the *absolute colorimetric* intent. The *relative colorimetric* intent also adjusts white and optionally also black point of the target space.

However, as can be seen in Figure 3, even if restricted to only modifying out-of-gamut values, different trajectories can be used to move out-of-gamut colours to the border of the displayable space. As reviewed by Mokrzycki *et al.* [MF98], the colour values can either be moved along the axis connecting them to the centre of the destination gamut (*node clipping*), or they can decrease their

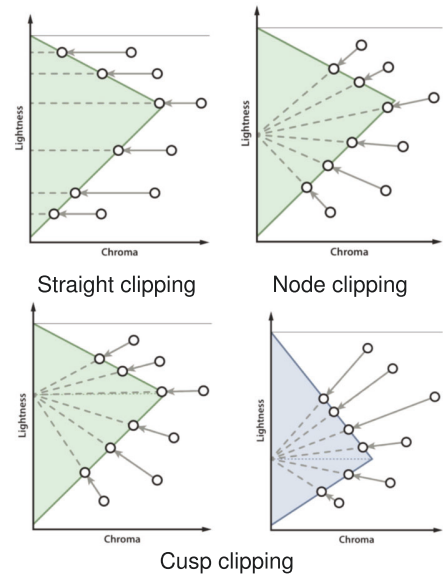


**Figure 3:** Possible approaches to the absolute colorimetric rendering intent. While the straight clipping approach preserves the luminance and decreases chroma, the node and cusp clipping approaches project the colours towards the neutral axis, retaining chroma but losing highlight information. Note that the cusp clipping is visualized for two different hues.

chroma component with constant luminance until they fall inside the gamut (*straight clipping*). While node clipping is susceptible to losing highlight information, straight clipping tends to create artificial highlights. Additionally, in order to improve the node clipping approach, *cusp clipping* has been proposed. There, the focus point is at the luminance of the most saturated colour for each hue. Although its results are better than those obtained with the node clipping approach, it is still susceptible to similar problems.

## 3. Constrained Spectral Uplifting

Similarly to Jakob and Hanika [JH19] and Jung *et al.* [JWH\*19], our uplifting model is also based on a pre-computed RGB coefficient cube that provides mappings of RGB values to their corresponding spectral representations. However, the spectral representation we employ must be capable of accurately representing the user-supplied spectra, which we need to reproduce. This cannot be done with the sigmoid approach as proposed by Jakob and Hanika [JH19], as it lacks enough degrees of freedom to match complex spectral shapes. Instead, we utilize the moment-based spectral representation [PMHD19]. In the following subsections, we first provide a brief overview of the principle behind this spectral representation, and then discuss how we fit a moment-based uplift coefficient cube based on the user-supplied target spectra.

### 3.1. Obtaining moment-based coefficients

As the shapes of spectra are aperiodic, storing them via Fourier coefficients requires their conversion to a periodic signal for which the

Fourier coefficients can then be computed. Although the mapping of wavelength range to the signal can be performed linearly, Peters *et al.* [PMHD19] advise against this approach and propose two improvements to the mapping—mirroring of the signal (which eliminates artefacts at the boundaries) and warping (which focuses the reconstruction accuracy on the area around 550 nm, i.e. the most important part in terms of colour reconstruction). After testing the proposed methods for the purposes of our uplifting model, we choose to mirror (due to more accurate round-trips), but not warp the signal (due to its incompatibility with our model).

The moment-based coefficients stored for a periodic signal  $g(\varphi)$  are then computed as:

$$c = 2\Re \int_{-\pi}^0 g(\varphi)\mathbf{c}(\varphi)d\varphi, \quad (1)$$

where  $\mathbf{c}(\varphi)$  is the Fourier basis.

The coefficients  $c$  are referred to as *trigonometric moments*. Note that using  $|m|$  trigonometric moments for spectral representation implies that  $|c| = |m| + 1$  coefficients are actually stored. The additional factor is the zeroth moment  $c_0$ .

### 3.2. Reconstruction from moment-based coefficients

The process of spectral reconstruction from an input set of trigonometric moments is based on the theory of moments, specifically on maximum entropy spectral estimate (MESE) [Bur74], which has been shown to produce impressive results when used for the reconstruction of emission spectra. However, as the MESE is not bounded, it cannot be directly used for the reconstruction of reflectance spectra, which must satisfy the  $[0,1]$  range constraint. Therefore, *bounded MESE* has been introduced [PMHD19], which utilizes a duality between bounded and unbounded moment problems formulated in terms of the Herglotz transform. Based on this duality, trigonometric moments can be converted to their corresponding unbounded *exponential moments*, so that the bounded problem represented by the trigonometric moments has a solution if and only if the dual unbounded problem represented by the exponential moments has a solution.

Although this method has been shown to perform rather accurately for even a low number of moments (e.g. 5), reconstruction of complex reflectance spectra with sharp edges often requires a substantially higher coefficient count. By computing the Delta E round-trip error (specifically, the CIE 2000 Delta E) under multiple illuminants for a large ( $>12k$ ) database of spectra from multiple colour atlases, we empirically determined that for typical reflectance spectra the error stabilizes at around  $|m| = 20$ , i.e.  $|c| = 21$ .

Naturally, we wish for the reconstruction to be as precise as possible, however, we want to prevent unnecessarily high coefficient counts due to both memory consumption and, as discussed later, also time performance. Therefore, we opt for using a variable number of coefficients for each spectrum. This number is computed with a heuristically based iterative method—starting from  $|c| = 4$ , we check whether the coefficient count is sufficient, and, if not, we increase it and move on to the next iteration, repeating this process up to  $|c| = 21$ . The adequacy of the representation is determined

by its round-trip error under an error-prone illuminant (specifically, FL11). In contrast to our previous publication, we utilized the CIE Delta E 2000 metric instead of the RGB Euclidean distance. This eliminated our previous issues with inaccuracies in the dark regions of the cube.

Since the maximum allowed CIE Delta E 2000 error can be defined by the user, we cannot, in advance, determine the average number of coefficients needed for a moment-based representation. However, as concluded later (see Section 4.4.1), the memory overhead resulting from increased accuracy is negligible.

### 3.3. Seeding a moment-based uplift coefficient cube

In a similar manner that Jakob and Hanika use the centre point of the cube as a starting point for the fitting process, we utilize the user-provided constraints. We call this process the *seeding* of the cube. For each of the constraints, it works as follows.

First, we obtain the constraint's trigonometric moment representation  $c$ . Then, we find the constraint's position within the RGB cube according to its RGB value. As it is likely that it does not lie exactly on a lattice point, but rather falls inside one of the cube voxels, we assign the obtained coefficients  $c$  to all eight voxel corners. This is done in order to ensure proper reconstruction upon uplifting.

To support larger sets of user-provided spectra, e.g. whole colour atlases, we extend the cube by allowing multiple moment representations per lattice point. We distinguish them by constraint-specific IDs, which are then utilized during the uplifting process for the purposes of identifying the original seed of the voxel.

By seeding the cube, we have placed initial coefficients at some of the lattice points, which do not necessarily reconstruct curves that evaluate to the target RGB. Therefore, the coefficients must be modified so that the resulting colour difference is as low as possible.

Our problem of improving the coefficients satisfies the definition of the *Non-linear Least Squares* problem [GNS09]. Non-linear Least Squares is an unconstrained minimisation problem in the following form:

$$\underset{x}{\text{minimize}} \quad f(x) = \sum_i f_i(x)^2, \quad (2)$$

where  $x = \{x_0, x_1, x_2, \dots\}$  is a parameter block that we are improving (i.e. our coefficients) and  $f_i$  are so-called *cost functions*, which we want to minimize.

Similarly to Jakob and Hanika [JH19] and Jung *et al.* [JWH\*19], we utilize the CERES solver [AM\*] for solving our problem. We define the cost functions as follows:

$$\begin{aligned} f_0(x) &= |\text{target\_rgb.R} - \text{current\_rgb.R}| \\ f_1(x) &= |\text{target\_rgb.G} - \text{current\_rgb.G}| \\ f_2(x) &= |\text{target\_rgb.B} - \text{current\_rgb.B}| \\ f_3(x) &= \sum_{i=0}^s |\text{constraint}[i] - \text{current\_spectrum}[i]|, \end{aligned} \quad (3)$$

where  $target\_rgb$  is the RGB value of the lattice point,  $constraint$  represents a discretized reflectance spectrum of the input constraint,  $current\_spectrum$  represents the spectrum the current coefficients  $x$  reconstruct,  $current\_rgb$  is the RGB value of  $current\_spectrum$  and  $s$  is the number of samples used for internal representation of reflectance curves.

While the  $f_0(x)$ ,  $f_1(x)$  and  $f_2(x)$  residuals are identical to the previous approaches, we also add the  $f_3(x)$  residual (called the *distance* residual) in order to preserve the input spectral shapes.

### 3.3.1. Reduced coefficient count in unseeded cube parts

As the properties of the input spectra correspond to the initial fits of the lattice points, their number of coefficients is bound to be comparatively high. However, after the initial fitting round that deals with the RGB cube voxels that contain seeds, we do not need to maintain such high coefficient counts: this would be inefficient and memory consuming, in addition to propagating specific spectral shape features beyond the area of the RGB cube where they are actually wanted. Instead, once we leave the initial fitting regions that contain exemplar spectra we want to reproduce, we switch to lower-dimensional moment representations that intrinsically yield smooth spectra not unlike the sigmoids of the original technique [JH19]: the remainder of the lattice points are fit with three coefficients only.

The loosened requirements on the spectral shapes of the unseeded lattice points (i.e. we only want them to be smooth and to be within the same metamer family as their neighbours) additionally allow us to eliminate the distance cost function—computing only three RGB residuals has the added benefit of lower time complexity.

The conversion of a moment representation  $c_i$  of a seeded point to a fitting prior  $c_j$  for a non-seeded lattice point is performed by spectral reconstruction of  $c_i$  and its subsequent storage with only three coefficients. Although this process, called *coefficient recalculation*, causes loss of spectral information, it preserves the rough outline of the curve—essentially, it can be viewed as a low-pass filter. This works to our benefit—it reduces the likelihood of significant colour artefacts between the seeded and non-seeded points, while keeping the spectra smooth.

The last detail we discuss is how to perform coefficient recalculation of lattice points that contain multiple moment representations. Let us assume lattice point  $P$  and its two seeded neighbour voxels,  $A$  and  $B$ . After seeding of the cube,  $P$  contains two moment representations, one from the metamer family of  $A$ , the other from  $B$ . Let us then assume a non-seeded lattice point  $Q$ , and let  $Q$  be a neighbour of  $P$ . Now, let us use the information provided by  $P$  as prior for fitting the moment representation of  $Q$ .

If we choose to employ only the representation corresponding to  $A$ , we can expect visible artefacts between  $Q$  and the voxel  $B$ . Similarly, recalculating only the representation of  $B$  would result in colour artefacts between  $Q$  and  $A$ . Therefore, in order to keep the colour transitions within all voxel pairs smooth, we first interpolate the spectra reconstructed from all coefficient representations of  $P$  and we use the result of this interpolation as a basis of coefficient recalculation. In this specific case, this translates to the reconstruction of 2 spectra stored at point  $P$  (one belonging to moment repre-

sentation of  $A$ , the other of  $B$ ) and their linear interpolation resulting in a new spectrum that is subsequently stored with only three coefficients.

### 3.4. Interpolation of metamer spectra

In the following, we show that the linear combination of two spectra that are metamer under a given light source results in another metamer spectrum. To our best knowledge, this insight, while not particularly mathematically complex, has not been explicitly stated in graphics literature before.

Let us assume the spectral power distributions of two metamers saved at a lattice point,  $P_1(\lambda)$  and  $P_2(\lambda)$ , that satisfy the conditions

$$\begin{aligned} \int P_1(\lambda)\bar{r}(\lambda)d\lambda &= \int P_2(\lambda)\bar{r}(\lambda)d\lambda \\ \int P_1(\lambda)\bar{g}(\lambda)d\lambda &= \int P_2(\lambda)\bar{g}(\lambda)d\lambda \\ \int P_1(\lambda)\bar{b}(\lambda)d\lambda &= \int P_2(\lambda)\bar{b}(\lambda)d\lambda \end{aligned} \quad (4)$$

where  $\bar{r}(\lambda)$ ,  $\bar{g}(\lambda)$  and  $\bar{b}(\lambda)$  are the RGB colour matching functions.

Let us express the R component of the RGB value resulting from the linear combination of  $P_1(\lambda)$  and  $P_2(\lambda)$  as follows:

$$R = \int a \cdot P_1(\lambda)\bar{r}(\lambda)d\lambda + b \cdot P_2(\lambda)\bar{r}(\lambda)d\lambda, \quad (5)$$

where  $a + b = 1$

By rewriting this expression and utilising the equality from Equation (4), we get

$$R = a \cdot \int P_1(\lambda)\bar{r}(\lambda)d\lambda + (1 - a) \cdot \int P_1(\lambda)\bar{r}(\lambda)d\lambda, \quad (6)$$

So

$$R = \int P_1(\lambda)\bar{r}(\lambda)d\lambda \quad (7)$$

The same proof can be equivalently applied to the G and B components of the resulting RGB value. Therefore, we conclude that the resulting spectral distribution is also a metamer.

### 3.5. Using a moment-based coefficient cube in a renderer

Discretisation of the RGB space in terms of a cube-like structure poses the problem of how to uplift RGB query values for which no direct mapping to a moment representation exists (i.e. which do not directly lie on a lattice point). In such a case, it is reasonable to employ a weighted trilinear interpolation of the data stored at the eight voxel corners: both Jakob and Hanika [JH19] and Jung *et al.* [JWH\*19] propose interpolating the (in their case: sigmoid) coefficients, mainly due to this being faster than interpolating the reconstructed spectra. In our own implementation of the original sigmoid fitting, we noted that such an interpolation of coefficients indeed works: but interpolation of complete spectra is more accurate even for sigmoids. Additionally, as our technique uses variable

coefficients counts, interpolating coefficients within a voxel is generally not an option. Therefore, we always interpolate the reconstructed spectra.

Due to the potential presence of multiple moment representations per lattice point, reconstruction of spectra at such lattice points is not straightforward. If a voxel has been seeded during the construction of the uplifting model, we force exclusive use of the metamer family of the original spectral seed, in order to achieve our goal of matching the input spectra. In all other voxels, for each of its eight lattice points, we reconstruct spectra of all moment representations that have accumulated there, and interpolate between them in equal ratios: as discussed in Section 3.4, this is permissible, and also yields a metamer for the RGB coordinates of the lattice point. This ‘hybrid’ metamer is then used as input for the eight corner trilinear interpolation that yields the actual result spectrum for the RGB query value. The reason for this strategy is the same as for the coefficient recalculation, i.e. to provide a smooth transition between metamer families.

Whether the voxel has been seeded or not is determined by means of the unique IDs assigned to the moment representations during the seeding process. If the voxel corners share a common ID, it is the representations corresponding to this ID that must be utilized in order to properly reconstruct the seeds.

### 3.6. Support of larger RGB gamuts

Since the RGB spaces are bounded orthogonal systems, the shape of their gamut is a cube. In the case of sRGB, the RGB cube is at the same time also the gamut of possible reflectances *within sRGB*. However, with other larger RGB gamuts, this is no longer the case. For example, for the Adobe Wide Gamut RGB (*wRGB*) gamut, the subset of colours that correspond to valid surface reflectances is a convex, curved shape and, as Figure 4 shows, considerable parts of the *wRGB* cube do not correspond to colours that can be realized by plain reflectance spectra. These can only be realized via emission, or reflectance with a fluorescence component [JWH\*19].

In this section, we describe our method of supporting targeted uplifting within larger RGB gamuts, and specifically demonstrate it for the Adobe Wide Gamut RGB gamut.

It is obvious that if a coefficient cube approach like in our previous work [TWF21] is used, a significant number of the cube’s lattice points fall out of gamut, so no exactly matching reflectance spectra can be synthesized for them. Although a simple solution would be to discard the out-of-gamut points and flag their voxels as ‘empty’, this would cause issues during uplifting in the voxels containing the gamut’s boundary. We call these voxels the *boundary* voxels, since a part of their values lies within the gamut and the rest is outside. If, during uplift, a *wRGB* value falls into the boundary voxel, our system has no means of interpolating between its corners, since not all of them contain reflectance values. Therefore, even these values would have to be discarded, which in turn results in incomplete support of larger gamuts.

We address this issue by applying a gamut mapping technique, which assigns the out-of-gamut lattice points coefficients of a boundary RGB value closest to them. This results in plausible, al-

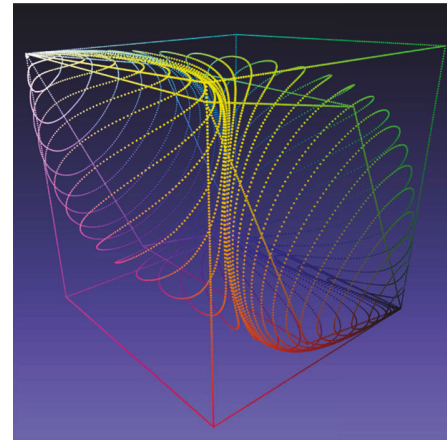


**Figure 4:** The gamut of realisable reflectances, the sRGB and the wRGB coefficient cubes. While the sRGB cube only covers a part of the gamut, the wRGB cube encompasses most of it (note that small parts are sticking out of the cube, mainly in the yellow and cyan regions). The transparent parts of the cube do not correspond to colour values that can be realized as plain reflectance spectra: these RGB values need to be mapped to the gamut of realisable reflectances.

beit slightly incorrect colours in the boundary voxels, and has the additional benefit of also supporting other out-of-gamut RGB values (which is valuable if e.g. an artist paints a texture that is too colourful). Following, we explain the applied gamut mapping technique in more detail.

#### 3.6.1. Our approach to gamut mapping

Gamut mapping is performed as the final step of the cube creation, after the fitting of the lattice points. For its purposes, we utilize an absolute colorimetric intent—specifically, we use the node clipping approach described in Section 2.3). Since the goal of this paper is to preserve the exact colours of the constraints, employing any kind of global mapping approach is not an option, and, although we believe straight clipping would also provide satisfactory results, we have opted for node clipping in order to preserve saturation. Cusp clipping was not used due to being more complex and offering only moderately better results (if that).

In order to map an RGB value into the gamut, we first find the line from the entry to the centre of the cube. The RGB value we wish to map our out-of-gamut entry to lies on this line. To obtain it and its respective coefficients, we apply a recursive approach as described in Algorithm 1.

The recursive division of the line is only meaningful while its endpoints are in different voxels. Since we can expect the boundary voxel to already show colour inconsistencies due to some of its corners being out of gamut, once we reach this voxel in our division process, we can terminate the search. The initial *depth* parameter is, therefore, set to  $\text{depth} = \log_2(\text{diagonal})$ , where *diagonal* is the number of voxels on the diagonal of the cube.

**Algorithm 1.** Gamut mapping

---

```

1: function MOVETOGAMUT(center, outer, depth)
2:   middle.rgb  $\leftarrow$  (center.rgb + outer.rgb) / 2
3:   if depth > 0 then
4:     if middle is in gamut then
5:       MoveToGamut(middle, outer, depth - 1)
6:     else
7:       MoveToGamut(center, middle, depth - 1)
8:     end if
9:   else
10:    if middle is in gamut then
11:      final.rgb  $\leftarrow$  middle.rgb
12:    else
13:      final.rgb  $\leftarrow$  center.rgb
14:    end if
15:    final.coeff  $\leftarrow$  fit from voxel corner of final.rgb
16:    return final
17:  end if
18: end function

```

---

Once we find the RGB value we want our entry to map to, we obtain its coefficients (see step 15 of Algorithm 1). As prior, we use the coefficients of the corner of the voxel the RGB value falls into. If this lattice points have multiple coefficient representation, we perform coefficient recalculation in the same manner as we did during the fitting (see Section 3.3.1).

### 3.7. Wide gamut sigmoid-based uplift

Although the paper by Jakob and Hanika [JH19] focuses mainly on spectral uplifting within the sRGB gamut, we extend their work by creating a wRGB sigmoid-based uplifting cube. We do this solely in order to provide comparisons of a non-constrained approach to ours and to showcase the benefits of constraining the uplifting process.

The extension is done in exactly the same manner as ours for the moment-based cube. For lattice points outside of the supported gamut, we apply gamut mapping by recursively moving the points into the gamut, and subsequently running the CERES solver in order to obtain their coefficients. The only difference to our approach is that, since the points have only one fit, no coefficient recalculation needs to be performed.

## 4. Results

In the following, we evaluate the accuracy of our technique and compare its results to the sigmoid-based uplift as defined by Jakob and Hanika [JH19]. We start by assessing the quality of our implementation in terms of both accuracy upon uplifting constraints and the colorimetric properties of the uplifting system as a whole. We then assess the plausibility of our gamut mapping technique for wide gamut uplifting. Lastly, we provide measurements of both memory utilisation and time performance. All the data of colour atlases and illuminants used in our experiments were provided by ART [Wil18].

### 4.1. Accuracy of constrained uplifting

We determined the accuracy of our proposed constrained uplifting approach by measuring the round-trip error of a large constraint set: the Munsell Book of Colour (MBOC). As difference metric, we used CIE Delta E 2000.

As expected, since the cube was fitted with regard to the daylight CIE D65 illuminant, the round-trip error under D65 was negligible. However, examining the behaviour of our model under more complex, spiky illuminants, similar to the fluorescent illuminant used in the xRite Judge QC viewing booth (see Figure 2), proved to be more interesting.

In our experiments, we utilized all 24 non-LED CIE standard illuminants, including the five high pressure discharge lamp ones. For all constraints and illuminants, we measured both the average round-trip  $\Delta E$  error and the percentage of round-trips that resulted in  $\Delta E \geq 1$ . In order to assess the effect of the input parameters on the performance of our uplifting model, we ran the experiments for multiple cubes with different resolutions, as well as different error allowed during the storage of spectra with moments. We also ran the same experiments for sRGB as well as wRGB. Note that not all constraints were utilized for every experiment—especially for smaller cubes, constraints with similar RGB values fall into the same voxels, so that only one of them can be used (see section 4.4.1 for more detail). Additionally, for sRGB, constraints falling outside of the gamut had to be omitted.

For the purposes of comparing the constrained uplifting model to the non-constrained approaches, we also ran the same experiments for the sigmoid cubes as proposed by Jakob and Hanika [JH19].

The results, presented in Table 1, show slight improvement in both the average error and the percentage of erroneous uplifts (i.e. uplifts that resulted in  $\Delta E \geq 1$ ) with increasing cube resolution and also decreasing permitted error during constraint storage. We attribute the higher errors in cubes with lower resolution to the higher distance between the original constraints' positions and the corners of their respective voxels during the seeding process. Because of this, the prior coefficients passed to the optimizer are further away from the desired coefficients, allowing the optimizer more room for error. The maximum allowed error parameter only accentuates this deficiency, as the coefficients are already stored with less precision.

While the results do not show significant differences between sRGB and wRGB cubes, we can observe that the wRGB cubes perform slightly better for almost all cases. This may initially seem contradictory, mainly due to our statement in the previous paragraph. As the wRGB cube is noticeably larger than the sRGB cube, its voxels are also larger than those of the sRGB cube, subsequently resulting in larger distances between the constraints and their seeded voxel corners. Additionally, especially for cubes with lower resolutions, the fitting process of seeded points in the wRGB cubes occasionally fails and the spectra need to be stored with three coefficients only, which does not happen at all for the sRGB gamut.

We attribute this behaviour to the shapes of the spectra: according to our observations, constant spectral shapes are more prone to failure. This is because the trigonometric moments are, in their nature, Fourier coefficients, and are therefore not well-suited for

**Table 1:** The average Delta E 2000 error and the percentage of constraints' round-trips with  $\Delta E \geq 1$ , measured both for the sRGB and the wRGB gamut, for different sets of input parameters as well as for sigmoid cubes as defined by Jakob and Hanika [JH19]. The constraint set utilized was the Munsell Book of Colour, and the illuminants under which the experiments were performed were the CIE standard illuminants and the HP illuminants. Note that not all entries of MBOC were utilized for the experiments due to collisions of constraints in cube voxels.

sRGB										
Max $\Delta E$ Dim	8		16		32		64		128	
	Avg	$\Delta E \geq 1$	Avg	$\Delta E \geq 1$	Avg	$\Delta E \geq 1$	Avg	$\Delta E \geq 1$	Avg	$\Delta E \geq 1$
2.0	0.52	0.1461%	0.52	0.1520%	0.53	0.1547%	0.51	0.1425%	0.50	0.1373%
1.0	0.40	0.0866%	0.41	0.0912%	0.41	0.0919%	0.39	0.0853%	0.38	0.0805%
0.5	0.32	0.0541%	0.27	0.0379%	0.25	0.0308%	0.24	0.0275%	0.24	0.0268%
0.25	0.26	0.0325%	0.17	0.0148%	0.14	0.0086%	0.13	0.0061%	0.13	0.0050%
0.1	0.20	0.0330%	0.11	0.0083%	0.07	0.0027%	0.06	0.0010%	0.06	0.0009%
0.05	0.17	0.0282%	0.07	0.0066%	0.06	0.0026%	0.05	0.0006%	0.04	0.0002%
Sigmoid	46.73	0.9581%	47.89	0.9581%	50.87	0.9581%	56.9	0.9581%	68.05	0.9581%

wRGB										
Max $\Delta E$ Dim	8		16		32		64		128	
	Avg	$\Delta E \geq 1$								
2.0	0.65	0.1716%	0.50	0.1282%	0.45	0.1114%	0.43	0.1074%	0.42	0.1010%
1.0	0.58	0.1377%	0.42	0.0885%	0.37	0.0733%	0.35	0.0651%	0.34	0.0605%
0.5	0.50	0.1115%	0.31	0.00472%	0.25	0.0304%	0.23	0.0239%	0.22	0.0221%
0.25	0.51	0.1140%	0.25	0.0315%	0.15	0.0177%	0.13	0.0054%	0.12	0.0042%
0.1	0.52	0.1205%	0.20	0.0324%	0.09	0.0093%	0.06	0.0021%	0.05	0.0005%
0.05	0.52	0.1360%	0.18	0.0280%	0.08	0.0086%	0.05	0.0021%	0.04	0.0003%
Sigmoid	57.79	0.9559%	54.21	0.9580 %	56.28	0.9555 %	57.51	0.9555 %	61.18	0.9558%

representing a constant signal: a deficiency the optimizer further amplifies. As the shapes of colours with low saturation tend to resemble constant lines, as opposed to the more complex spectra of saturated colours, it is expected that their reconstruction is more prone to error.

While the optimizer's failures during the fitting process may appear concerning, this rarely happens—for cubes with  $res = 32$  (i.e. of size  $32^3$ ), we observed only around four failures during the seeding of the whole constraint set (containing 891 entries, i.e.  $891 * 8 = 7128$  seeds). Additionally, if the fitting does fail, it is always for the voxel corners that are farthest away from the constraints—in our case, these usually had the interpolation weight lower than 0.1, meaning that their influence on the uplifted spectral shape was minimal. Realistically, this deficiency can only be observed for the wRGB cubes with  $res = 8$ , which demonstrate even worse results than their sRGB counterparts. Therefore, in case wide gamut support is required, we advise on setting the resolution parameter to at least  $res = 32$ .

However, overall, utilising cubes with even smaller resolutions and higher allowed error appears promising. As the maximum error perceivable by a standard observer is  $\Delta E < 1$  [MT11], even the average Delta E of 0.53 is highly sufficient for reproduction purposes, and while the model cannot guarantee no human perceptual discrepancies, these can be minimized by tweaking the input parameters.

With regard to the performance of the sigmoid model, the improvement is significant, even for cubes with low resolutions. While our model results in only an extremely small portion of the constraints with the round-trip error of  $\Delta E \geq 1$ , for the sigmoid cubes, this number is as high as 96%. Closer examination has revealed that

the round-trip measurements resulting in  $\Delta E < 1$  were all obtained under the CIE D65 illuminant, i.e. the illuminant under which the sigmoid cubes were fitted. However, note that while the average Delta E error for the sigmoid cubes is rather high, this does not make the cubes unusable for regular uplifting purposes: for our experiments, we specifically chose complex, spiky spectra that expose the constraints' susceptibility to metamerism artefacts.

We compare the effect of our uplifting technique on the resulting curve shapes in Figure 5, where we provide comparisons of curves of the seeded and uplifted spectra. We can observe that the differences are negligible, and that the slight deviations from original curves are mainly due to the imperfections of the optimizer rather than the moment representation.

In Figure 6, we present the results of comparison between the sigmoid-based uplifts and our constrained uplifts on specific pages of the Munsell Book of Colour. We set the resolution of our cubes to 64, because it is a sufficient enough size for all constraints to be utilized, and we set the maximum allowed Delta E to 0.1. While the results are satisfactory enough even for higher Delta E parameter, we consider the slight memory and performance overhead resulting from higher coefficient representations (see Section 4.4) to be worth the higher constraint uplifting accuracy. For this reason, we also set the maximum allowed Delta E parameter to 0.1 for other experiments performed in this paper. Due to our experiments presented in Table 1, setting the parameter to even lower values does not noticeably improve the constraint uplifting accuracy.

We can clearly see that our technique provides reasonable results throughout, while images uplifted with the sigmoid-based cube demonstrate rather significant colour errors. Although our model

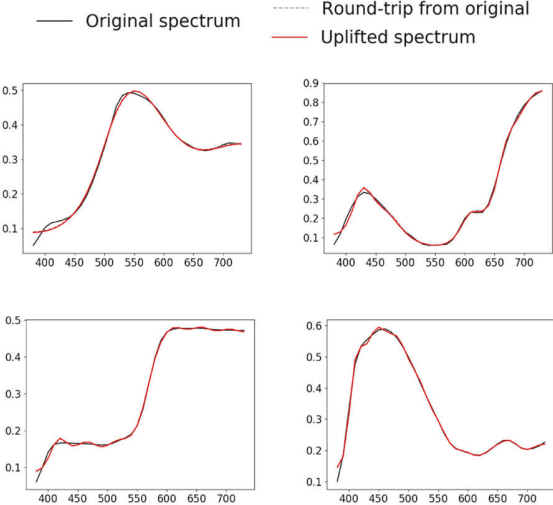


**Figure 5:** Accuracy of constrained uplifting demonstrated on examples of input spectra. The spectral curve labelled round-trip is a direct reconstruction of the spectrum from the moments used to seed the fitting process. The red curve labelled uplift is the result of querying the final coefficient cube, including interpolation within the voxel the RGB value falls into. All three curves should be identical: separating ‘round-trip’ and ‘uplift’ shows whether any error that is present is caused by the moment-based representation, or the interpolation in the coefficient cube. As one can see, the uplifted spectra follow the spectra reconstructed from the original coefficients quite precisely, and also match the input spectra pretty well. Note that the demonstrated range on the y-axis is not [0,1], i.e. the deviations are even less perceptible than demonstrated.

does not completely eliminate human-perceivable errors, these occur exclusively for extreme illuminants, such as HP2, which excessively amplify even the smallest deviations that occur due to the moment-based representation.

Other small deviations in the uplifting process are expected both because of the imprecision of the moment-based representation and due to the failures of the optimizer during the seeding process. These can be observed mainly for the darker colours, since their spectra tend to resemble constant lines close to zero. However, note that the error caused by this ‘failure’ is still barely (if at all) perceptible.

#### 4.2. Uplift consistency across RGB space

In order to assess how our technique uplifts the entire supported RGB gamuts (and not just the regions around the seeds), we created multiple uplift cubes that were seeded with different colour atlases. This included an atlas with a single starting constraint at  $\text{RGB}(0.5, 0.5, 0.5)$ , i.e. fitted with the same sole starting constraint as the sigmoid-based approach by Jakob and Hanika [JH19].

We first compared their performance in terms of colour reconstruction with regard to uplifting a gradient texture. We selected a gradient with highly saturated sRGB colours, and we uplifted it

for all selected uplift cubes under a spiky, error-prone illuminant, specifically HP2 (under D65, there are, as per the fitting process, practically zero differences). The choice for the HP2 illuminant, the sRGB gamut and the saturated texture was motivated by the fact that under these conditions, the differences between individual uplifts are most perceivable. While the wRGB gamut shows similar differences, some of the values of the texture may fall inside the boundary voxels and therefore, their uplifts are less pronounced than if they were properly inside the gamut. Similarly, the differences are present even under other illuminants (or for other textures), but are less noticeable.

In Figure 7, we compare the resulting uplifts. While the distinctions between them are barely perceptible by the human eye, the difference images between individual pairs demonstrate some variations—mainly around the locations of seed points, which is precisely what is intended by constraining the uplifting process. To be specific, the most evident artefacts can be observed for the MBOC constraint set, especially in the light green region, and for the RAL and MCCSG constraint sets in the saturated red region. We contribute this to the distinct, complex input spectra (i.e. spectra from different metamer families) in these regions which, however, evaluate to RGB values in close vicinity. This makes them exhibit metamer discontinuities similar to that of the 075Y and 100Y pages of the Munsell Book of Colours (see Figure 2).

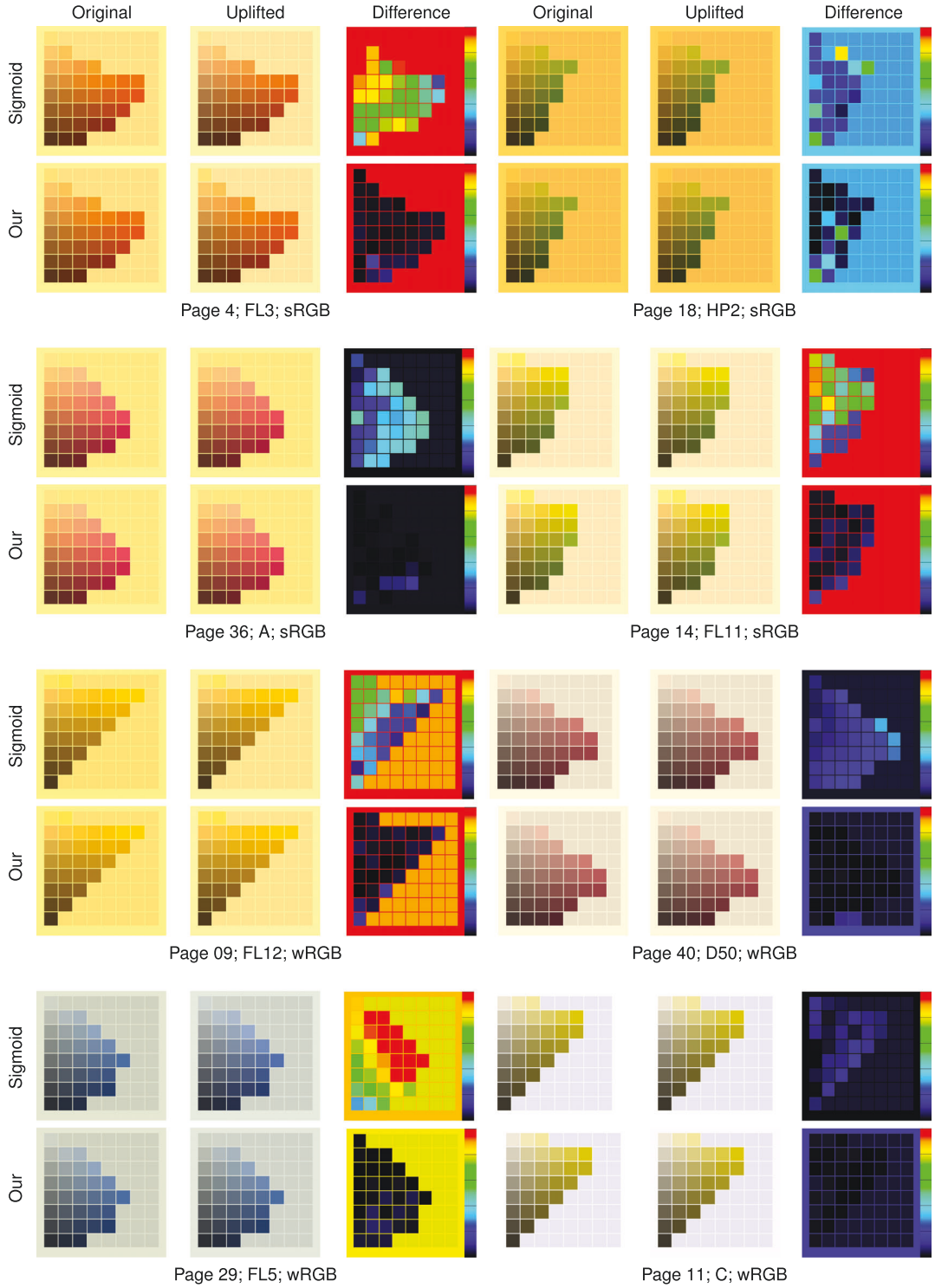
None of the gradient textures, however, exhibit any significant discontinuities, which indicates that our interpolation approach works properly in the presence of multiple metamer families of reflectance spectra.

Figure 8 demonstrates that our approach can properly uplift large regions of the RGB gamut without showing artefacts under varying illumination. We provide multiple renderings of a rainbow texture, uplifted with various constraint sets under distinct illuminants both for the sRGB and the wRGB gamut. Even though a considerable subset of all voxels was seeded and the remainder was filled in with smoother spectra (as described in Section 3.3.1), none of the renderings exhibit significant artefacts.

#### 4.3. Performance of gamut mapping

While some of the wRGB textures shown in the preceding sections already contained colours outside the gamut of realisable reflectances, the performance of the gamut mapping technique has not yet been explicitly analysed. In order to do so, we created a texture with values falling out of wRGB, uplifted it under the D65 illuminant and subsequently applied gamut mapping. We present the results in Figure 9.

As anticipated, there is a visible difference between the original texture and the gamut-mapped uplift in the places of the out-of-gamut values. Since the RGB values in close proximity to each other in terms of hue are mapped to extremely similar values, the gradients in the texture’s out-of-gamut areas tend to fade out, giving rise to areas with constant colours. Therefore, the farther away the out-of-gamut value is from the gamut boundary, the higher the difference between the original and the uplifted RGB value (see also Figure 9). This is an expected and desired behaviour of local gamut mapping techniques. Additionally, while the mapped values in



**Figure 6:** Comparison of our uplifting model with the sigmoid-based technique [JH19] for pages of the Munsell Book of Colour under different illuminants. For each of the constrained uplifts, we utilize a different moment-based cube seeded with the colour patches from that specific page, with the maximum delta  $E$  parameter set to 0.1 and the resolution parameter set to 64. The difference images are relative to maximum  $\Delta E_{00} = 3$ . Note that patches that fall outside sRGB have been omitted for the first four visualized pages.

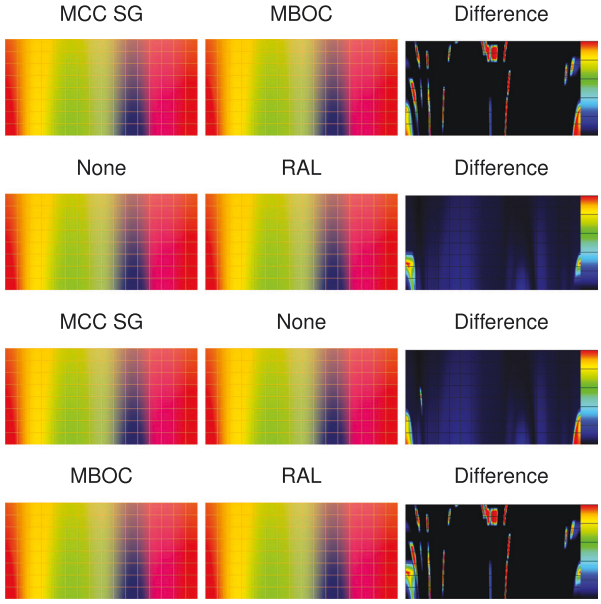


**Figure 7:** A region of the sRGB gamut uplifted with different sets of input spectra, illuminated by HP2. The difference images between selected pairs serve as a tool for demonstrating the effects of different constraint sets on the resulting uplift. Note that the difference images are relative to maximum  $\Delta E = 2$ , i.e. the differences are perceptible by the human eye.

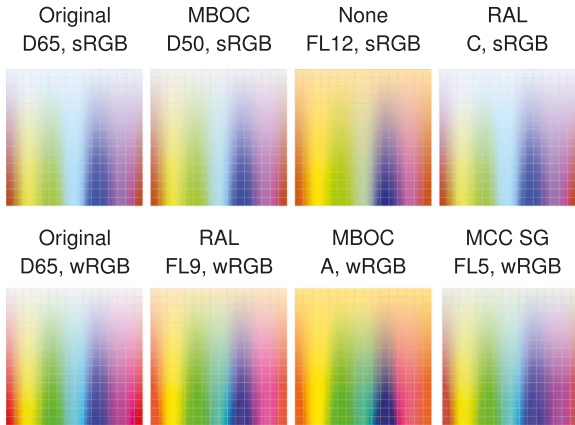


**Figure 8:** Constrained spectral uplifting of a colourful texture for various constraint sets under different illuminants. Note that all uplifts were performed with  $64^3$ -sized cubes, i.e. some of the constraints may not have been utilized due to collisions during seeding. Also note that the colour gamuts of the uplifts are scaled so that wRGB fits into the standard sRGB gamut that can be shown on screen. This results in the desaturated appearance of the sRGB uplifts.

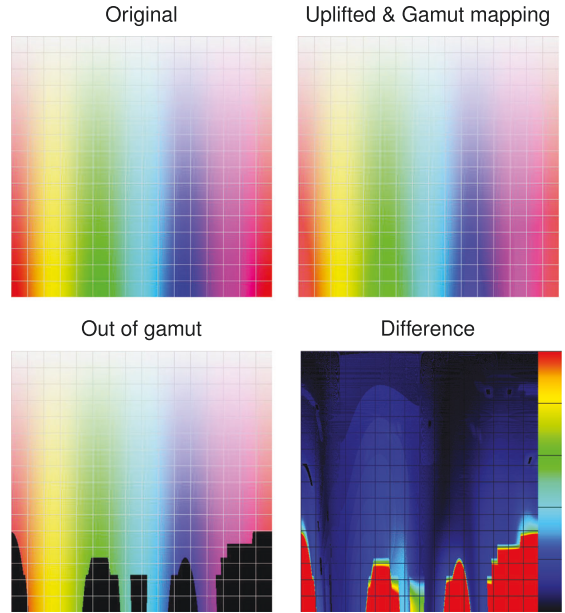


**Figure 9:** The behaviour of our gamut mapping strategy shown on a wRGB texture with out-of-gamut values. The image labelled Out of gamut highlights the values from Original texture that fall outside of wRGB, while the image labelled Uplifted & Gamut mapping was obtained by uplifting the Original texture under the D65 illuminant with a cube of size  $64^3$  and by subsequently applying our gamut mapping strategy. The Difference image shows the difference between the Original and the Uplifted textures. Note that it is relative to  $\Delta E = 1$ , and that the differences in the images are also perceptible by the human eye. Also note that not all values shown in the Out of gamut image necessarily fall out of gamut—some of them fall inside the boundary voxels, which also require gamut mapping.

areas of similar hues are similar, they are not identical, which prevents undesirable artefacts such as banding.

However, while the performance of our gamut mapping strategy is satisfactory, it is often utilized in cases where it should not be necessary, i.e. inside the gamut in the boundary voxels. This is not as problematic for cubes with higher resolutions, where the boundary voxels take up a small portion of the cube. However, if we were to use a cube with e.g.  $res = 8$  in order to uplift the texture from Figure 9, we would find that 31% of the image's voxels fall out of gamut in contrast to the 11% for a  $64^3$ -sized cube utilized for the purposes of Figure 9. To give a better example, for a cube of size  $8^3$ , we estimate that around 22% of the wRGB gamut is not supported and needs to be mapped, in comparison to roughly 3% for a cube of size  $64^3$ .

For future work, we propose solving this problem by either creating a dynamic structure that is capable of encompassing the whole wRGB gamut, or by utilising the fitted lattice points on the corners of the boundary voxels to determine the desired uplifted spectrum (e.g. by employing the optimizer). Currently, if high precision in

saturated colours is needed, we recommend utilising a cube with at least  $res = 64$ .

#### 4.4. Performance and future work

In this section, we evaluate the performance of our method in terms of both memory and execution time, and propose possible future work for their improvement.

##### 4.4.1. Memory usage

The memory necessary for storing our cube depends on its resolution (i.e. the number of lattice points), which is, in turn, dependent on both the size of our constraint set and on the position of its spectra within the RGB cube. For example, the Macbeth Colour Checker (MCC), which contains only 24 entries that are spaced quite far apart from each other in the RGB space (with one of them falling outside of sRGB), requires as little as a  $13^3$ -sized cube for both the sRGB and the wRGB gamut. Due to the close proximity of some seeds, the 1396 sRGB entries of the Munsell Book of Colour would require as much as 340 lattice points per axis for all seeds to fall into a unique voxel, and, for its 1597 wRGB entries, the cube resolution would need to be as high as 420 and even then, one constraint would remain unseeded. Additionally, due to the rigid nature of an evenly spaced voxel grid, using a higher cube resolution does not necessarily imply more points that can be successfully seeded. Due to voxel edges being in different positions for different cube resolutions, increasing cube size might even have an adverse effect—for example, while an sRGB cube of size  $90^3$  is sufficient for the sRGB entries of the RAL Design atlas, in a  $300^3$ -sized cube, 1 point remains unfitted due to a voxel collision.

To store the coefficients of cube entries, we require three floating point values for all non-seeded points, and, for a cube with maximum allowed  $\Delta E$  set to 0.1, an average of 16 floating point values per constraint. For the  $340^3$ -sized sRGB cube required for the proper coverage of the Munsell Book of Colour, this would yield a size of over 450.35MB. Although decreasing the maximum allowed  $\Delta E$  parameter and therefore using less coefficients for storing constraints is possible, it would not noticeably improve the size of the cube—even if we were to use three coefficients for all coefficient representations within the cube, the overall size would still be over 449.8MB. That is a negligible improvement, and the overall size remains excessive—after all, the seeding of all sRGB entries of the Munsell Book of Colour requires only 1396 voxels, which sums up to a maximum of  $8 \cdot 1396$  lattice points. Additionally, while most of the regions of the cube are barely utilized, there exist some that have all of their voxels fitted, which might result in a lack of smooth colour transitions within these regions.

We, therefore, conclude that, for the purposes of constrained spectral uplifting for large sets of user-supplied target spectra (e.g. entire colour atlases), a coefficient cube with evenly spaced lattice points is distinctly sub-optimal, in terms of both memory requirements and its resulting colorimetric properties. As future work, we will investigate a dynamic structure e.g. kD-trees, which can split the RGB space into variably sized voxels according to the number of constraints.

**Table 2:** Fitting time of a  $32^3$ -sized sRGB coefficient cubes with  $\max_{\Delta E} = 0.1$  for multiple colour atlases. As the chosen cube resolution may be insufficient for the utilisation of all constraints in a given atlas (see Section 4.4.1), we also provide the number of seeds that were placed on lattice points. Note that as the performance metric, we use the wall clock time.

Colour atlas	Number of seeds	Seeding time	Fitting time	Overall
MBOC	7672	33 min 53 s	42 s	34 min 35 s
RAL	1072	4 min 59 s	43 s	5 min 42 s
Macbeth SG	560	2 min 48 s	45 s	3 min 33 s
Macbeth	184	1 min 43 s	1 min 15 s	2 min 58 s
None	1	0.03 s	4 min 00 s	4 min 00 s
Sigmoid	1	0.01 s	24 s	24 s

However, it has to be noted that the approach presented in this paper works perfectly fine for constraint sets with up to several dozen, or even low numbers of hundred, data points. This is sufficient for typical usage in VFX scenarios, where only a few key assets (e.g. the main colours of the costume of a lead character) are measured on set, in order to later constrain the spectral uplift of virtual doubles.

##### 4.4.2. Execution time

Since our uplifting model is created prior to the rendering process, we divide the evaluation of the execution time into two parts—the cube creation process, and the rendering speed when utilising our cube for uplifting purposes.

We test the execution time of cube fitting on multiple sets of constraints in forms of colour atlases, and present the results obtained for the sRGB gamut in Table 2. The size of each cube is  $32^3$ , and the maximum allowed Delta E is set to 0.1. All the experiments are performed on an Intel Xeon CPU E5-2680 v3 (48 logical cores).

Due to the higher coefficient count and the strict requirements placed upon the shapes of the reconstructed spectral curves, the fitting of seeded lattice points takes significantly longer than the fitting of the latter (on average, a seeded point takes 0.27 s to fit, in comparison to the 0.004 s for those which are not seeded). However, as the cube fitting process is multi-threaded, it benefits from multiple starting points evenly positioned across the RGB cube. This is particularly obvious when comparing the performance of the fitting of the Macbeth charts and the fitting without constraints.

Other factors affecting the performance of cube creation are the user-defined parameters, i.e. the resolution of the cube and the maximum allowed Delta E. While it is obvious that the fitting time will increase with increasing cube resolution, it is noteworthy that this does not happen for the seeding time. For example, for a cube of size  $8^3$  constrained with MBOC ( $\Delta E = 0.1$ ), the average fitting time of a seeded point is 0.64 s, while for its  $128^3$ -sized variant, it is only 0.11 s. This is due to larger voxels in cubes with lower resolutions. As already observed when examining the decreased accuracy of constraint uplifting in cubes with smaller resolutions (see Section 4.1), larger voxels imply increased distance between the constraints' RGB values and the RGB values of the voxel corners. This causes greater difference between the constraints' spectral shapes

and the desired spectral shapes of the seeded points, subsequently resulting in more iterations of the optimizer.

Decreasing the maximum allowed Delta E parameter also results in higher seeding time, due to higher number of coefficients per representation and higher required precision, both of which strain the optimizer. However, for  $\Delta E = 1$ , representations with only four coefficients are generally sufficient, and therefore, setting the parameter above the value 1 does not noticeably improve performance.

For wRGB cubes, the ratio between their seeding and the fitting time is almost identical to their sRGB counterparts. However, in their case, the performance of cube creation is also affected by gamut mapping.

The time it takes to move a point inside the gamut is identical for each lattice point, and is only dependent on the number of recursive iterations, i.e. on the resolution of the cube. Since the gamut always takes up the same portion of the cube (in case of wRGB, roughly 20% of voxels fall out of gamut—however, this number decreases with higher resolutions due to smaller portion of cube voxels being on the gamut boundary), the overall performance of gamut mapping is, therefore, dependent only on the cube size and on the time spent in one iteration of the recursive gamut mapping process. By performing experiments similar to those presented in Table 2 on the wRGB cubes, we have observed that the overall time of gamut mapping is 12 s for  $32^3$ -sized cubes. From this knowledge and the knowledge of how many lattice points fall out of gamut, we can compute this value for any other cube resolution—for example, for cubes with  $res = 16$ , the time spent on gamut mapping is only 3s, and for the cubes of size  $128^3$ , this is 155 s. We have performed additional experiments for wRGB cubes of other resolutions to support this claim.

In terms of overall performance, for the unconstrained cubes, the gamut mapping process takes up around 7% of the whole cube creation process. While this might be slightly higher for their constrained variants (since their fitting benefits from multiple starting points), overall, the time spent on gamut mapping is acceptable and, in contrast to the seeding process, even negligible.

None of these usage cases outperform the sigmoid-based cube in terms of fitting time. While our technique needs to use various complex mathematical operations, such as the application of Levinson’s algorithm, Herglotz transform and multiple other conversion processes [PMHD19], not to mention the interpolation of metamers for lattice points with multiple representations and a non-trivial check on whether the current voxel has been seeded, the sigmoid-based approach evaluates the spectral curve from a coefficient set with as little as six floating point operations for any given wavelength [JH19].

This drawback of our technique also carries over to using our method during rendering. In order to properly evaluate the execution time, we perform two tests—first, we compare the performance of the sigmoid-based cube with the performance of our non-constrained cube (in order to avoid the overhead of spectral reconstruction from higher-dimensional coefficient representations), and second, we provide measurements of the execution time of the constrained uplift of the renders in Figure 6. The testing conditions are identical to the previous experiment—the resolution of the tested cubes is set to  $res = 64$ , and the maximum allowed  $\Delta E = 0.1$ . How-

ever, we have observed that cubes with different user-defined settings perform similarly.

For the latter experiments, the sigmoid-based approach performed, on average, 2.1 times better than our constrained cubes. The performance overhead arising from constraining the uplifting process was expected. When used in a spectral renderer—specifically, ART [Wil18]—on a closely viewed texture of one of the pages of the Munsell Book of Colour (that is, when pretty much all the pixels in the image show the constrained texture), rendering times slow down by about a factor of four when compared to the sigmoid uplift.

For non-constrained uplifting, our method provides no benefits compared to the sigmoid-based approach, except perhaps that it creates slightly more varied spectral shapes. Even when not constrained, uplifting of the colourful textures shown in Figure 8 is 2.3 times slower with our cube than with the sigmoid-based technique.

That having been said, we wish to point out that so far, our focus was placed on the correctness and accuracy of the constrained uplift, i.e. our implementation of both the model creation and its utilisation in a renderer does not include any real optimisations yet. In the future, these could be applied to the fitting process (by further exploiting the possibilities of the CERES solver, or, possibly, another optimisation technique) and to the actual uplifting, which currently does not cache any intermediate values (such as the exponential moments) and therefore requires them to be unnecessarily re-computed during each uplift. We estimate that such optimisations could improve the performance up to a factor of two, both during fitting and during rendering.

We also note that our approach, while being both slower to fit and slower to render than the sigmoid technique, offers the unique capability of targeted uplifting, which was simply not available before. As such, we deem a somewhat slower performance compared to the sigmoid-based uplift to be an acceptable price to pay.

## 5. Conclusion

We presented the first method capable of constraining the spectral uplifting process with an arbitrary set of target spectra. By utilising a trigonometric moment-based approach for spectral representation, the RGB values of the target spectra are accurately uplifted to their original spectral shapes, while the rest of the RGB gamut uplifts to smooth spectra. This results in smooth transitions between the various metameric families that originate from the constraining process.

In terms of colour accuracy, the results of our uplifting model are noteworthy, as the uplifted curves describe the original ones with negligible differences. We also propose an approach with which to apply our method to larger gamuts, where we achieve similar results.

However, neither the memory, nor the execution time of the uplifting process of our model are optimal: the new and so far unique capability to perform targeted uplifts comes at the cost of some overhead that is not present in e.g. the unconstrained sigmoid uplift technique of Jakob and Hanika [JH19]. Additionally, our support of wRGB is not complete, since, for our recommended settings, an estimated 3% of the wRGB gamut is uplifted to less saturated values.

In the future, we will primarily focus on utilising a more suitable and memory efficient structure for storing the constraints, such as a kD-tree or an octree. We believe that such a structure would also enable us to cover larger gamuts more efficiently. Second, we will improve the time execution by optimising the moment reconstruction process.

## Acknowledgements

We acknowledge funding by the Czech Science Foundation Grant 19-07626S, the EU H2020-MSCA-ITN-2020 Grant Number 956585 (PRIME) and the Charles University Grant Number SVV-260588.

## References

- [AM\*] AGARWAL S., MIERLE K.: Ceres solver. <http://ceres-solver.org> (2022).
- [Bur74] BURG J. P.: Maximum entropy spectral analysis. *Astronomy and Astrophysics Supplement* 15 (1974), 383.
- [GNS09] GRIVA I., NASH S., SOFER A.: Nonlinear least squares datafitting. In *Linear and Nonlinear Optimization*. SIAM - Society for Industrial and Applied Mathematics (2009), pp. 743–758.
- [Int10] International Color Consortium: Specification ICC.1:2010, profile version 4.3.0.0. 2010. [https://www.color.org/specification/ICC1v43\\_2010-12.pdf](https://www.color.org/specification/ICC1v43_2010-12.pdf) (2010).
- [JH19] JAKOB W., HANIKA J.: A low-dimensional function space for efficient spectral upsampling. In *Computer Graphics Forum* 38 (2019), pp. 147–155.
- [JWH\*19] JUNG A., WILKIE A., HANIKA J., JAKOB W., DACHSBACHER C.: Wide gamut spectral upsampling with fluorescence. In *Computer Graphics Forum* 38 (2019), pp. 87–96.
- [Mac35] MACADAM D. L.: The theory of the maximum visual efficiency of colored materials. *JOSA* 25, 8 (1935), 249–252.
- [MF98] MONTAG E. D., FAIRCHILD M. D.: Gamut mapping: Evaluation of chroma clipping techniques for three destination gamuts. In *Proceedings of the Color and Imaging Conference* (1998), vol. 1998, Society for Imaging Science and Technology, pp. 57–61.
- [MSHD15] MENG J., SIMON F., HANIKA J., DACHSBACHER C.: Physically meaningful rendering using tristimulus colours. In *Computer Graphics Forum* 34 (2015), pp. 31–40.
- [MT11] MOKRZYCKI W., TATOL M.: Colour difference delta E—A survey. *Machine Graphics and Vision* 20, 4 (2011), 383–411.
- [OYH18] OTSU H., YAMAMOTO M., HACHISUKA T.: Reproducing spectral reflectances from tristimulus colours. In *Computer Graphics Forum* 37 (2018), pp. 370–381.
- [PMHD19] PETERS C., MERZBACH S., HANIKA J., DACHSBACHER C.: Using moments to represent bounded signals for spectral rendering. *ACM Transactions on Graphics (TOG)* 38, 4 (2019), 1–14.
- [RVHN03] ROMERO J., VALERO E., HERNÁNDEZ-ANDRÉS J., NIEVES J. L.: Color-signal filtering in the Fourier-frequency domain. *JOSA A* 20, 9 (2003), 1714–1724.
- [Smi99] SMITS B.: An rgb-to-spectrum conversion for reflectances. *Journal of Graphics Tools* 4, 4 (1999), 11–22.
- [TWF21] TÓDOVÁ L., WILKIE A., FASCIONE L.: Moment-based constrained spectral uplifting. In *Proceedings of the EGSR (DL)* (2021), A. Bousseau and M. McGuire (Eds.), Eurographics Association, pp. 215–224.
- [Wil18] WILKIE A.: The Advanced Rendering Toolkit. <http://cg.mff.cuni.cz/ART> (2018).

# 3 HDR Environment Map Uplifting

The integration of image-based lighting in a spectral renderer plays a crucial role in achieving physical realism of a scene. By providing spatially-varying illumination from all directions, HDR environment maps allow a much closer approximation of real-world lighting conditions, which results in a more accurate shading and color reproduction.

However, the current state of the art for uplifting of such maps is lacking. As explained in Subsubsection 1.2.2 of Chapter 1, the existing techniques are only capable of obtaining HDR values by scaling existing reflectance uplifts, which does not reflect real-life behavior of the captured emissive properties. The discrepancies in the spectral shapes can lead to noticeable color deviations of the final renders, especially for environment maps whose captures contain complex, spiky light sources, such as, for example, LED or fluorescent indoor lighting.

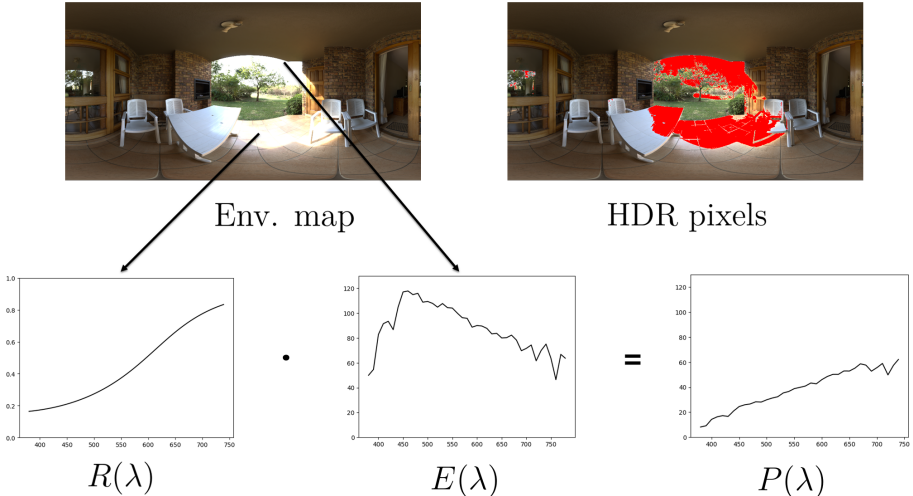


**Figure 3.1** The core principle behind the proposed method for HDR environment map uplifting. The final emission of an input HDR pixel,  $P(\lambda)$ , is obtained as a multiplication of the reflectance of the object the pixel belongs to,  $R(\lambda)$ , and the incoming emission,  $E(\lambda)$ .

The second contribution of this thesis addresses this issue with a novel uplifting method for HDR environment maps. The work is based on a simple observation: the emissive properties of objects captured in an environment map are a consequence of the illumination of the surrounding light sources, rather than an inherent property of the objects themselves. This implies that the final emission spectrum of a pixel in an HDR environment map ( $P(\lambda)$ ) can be obtained as a multiplication of the reflectance of the object the pixel belongs to ( $R(\lambda)$ ) and the incoming emission that hits the object ( $E(\lambda)$ ), i.e.:

$$P(\lambda) = E(\lambda) \cdot R(\lambda) \quad (3.1)$$

For visual example, see Figure 3.1.

The proposed work is therefore divided into multiple parts:

First, the main light sources of the scene and their respective emission spectra are determined. Then, all of the pixels of the input environment map are clustered depending on the light source that influences them the most (note: a pixel belongs to precisely one cluster). For every cluster, a reflectance uplifting model specific to its light source is created. The models are similar to the uplift cube used in our previous methods (see either Subsection 1.2.3 of Chapter 1 or Chapter 2), and are then used to identify the reflectance data of the individual pixels. Lastly, to obtain the final HDR uplifts, the reflectance spectra are multiplied by the emission of the cluster's light source as per a simplified version of Equation 3.1.

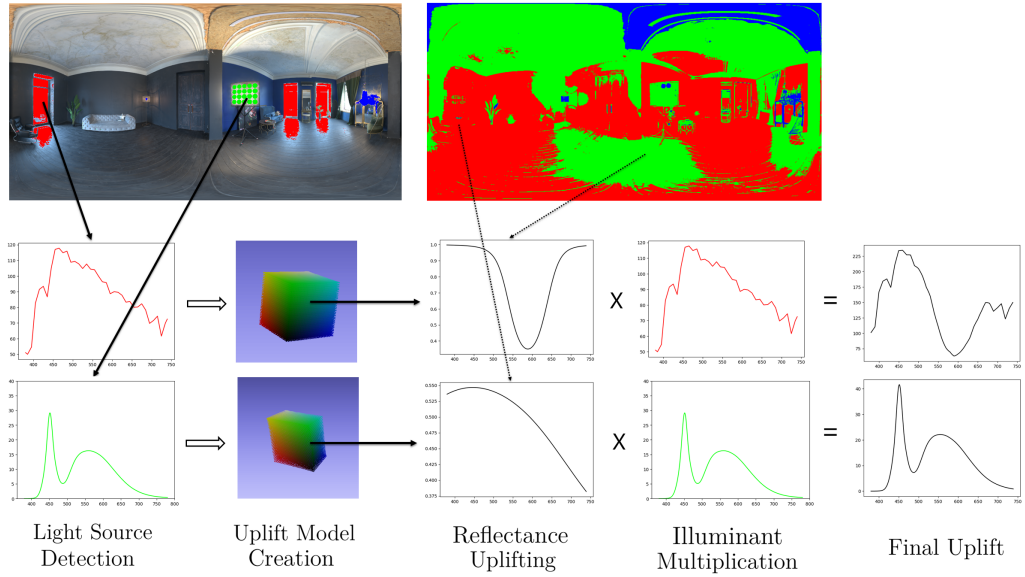


**Figure 3.2** A summary of the proposed uplifting process for HDR environment maps. First, the main light sources of the image are detected and the map's pixels are clustered depending on which light source they are influenced by the most. A reflectance uplifting model is subsequently created for each cluster. The reflectance spectrum of a pixel is then obtained from the model of its cluster, and the result is multiplied by the corresponding light source.

The implementation details are provided in the inserted paper. For convenience, we also include a simplified summary of the process in Figure 3.2, shown for an example input HDR environment map.

The method is first introduced in a conference publication (Tódová; Wilkie, 2024), and later extended for a journal publication with a thorough evaluation (Tódová; Wilkie, 2025).

The full citation of the conference publication follows.

TÓDOVÁ, Lucia; WILKIE, Alexander, 2024. Constrained Spectral Uplifting for HDR Environment Maps. In: HAINES, Eric; GARCES, Elena (eds.). *Eurographics Symposium on Rendering*. The Eurographics Association. ISBN 978-3-03868-262-2. ISSN 1727-3463. Available from DOI: 10.2312/sr.20241153.

The full citation of the journal publication follows.

TÓDOVÁ, Lucia; WILKIE, Alexander, 2025. Constrained spectral uplifting for HDR environment maps. In: *Computer Graphics Forum*. Wiley Online Library. Vol. 44, e15280. No. 1. Available from DOI: 10.1111/cgf.15280.

The full journal publication is inserted and begins on the next page.

# Constrained Spectral Uplifting for HDR Environment Maps

L. Tódová  and A. Wilkie 

Charles University, Prague, Czech Republic  
todova@gmail.com, wilkie@cgg.mff.cuni.cz

## Abstract

*Spectral representation of assets is an important precondition for achieving physical realism in rendering. However, defining assets by their spectral distribution is complicated and tedious. Therefore, it has become general practice to create RGB assets and convert them into their spectral counterparts prior to rendering. This process is called spectral uplifting. While a multitude of techniques focusing on reflectance uplifting exist, the current state of the art of uplifting emission for image-based lighting consists of simply scaling reflectance uplifts. Although this is usable insofar as the obtained overall scene appearance is not unrealistic, the generated emission spectra are only metamers of the original illumination. This, in turn, can cause deviations from the expected appearance even if the rest of the scene corresponds to real-world data. In a recent publication, we proposed a method capable of uplifting HDR environment maps based on spectral measurements of light sources similar to those present in the maps. To identify the illuminants, we employ an extensive set of emission measurements, and we combine the results with an existing reflectance uplifting method. In addition, we address the problem of environment map capture for the purposes of a spectral rendering pipeline, for which we propose a novel solution. We further extend this work with a detailed evaluation of the method, both in terms of improved colour error and performance.*

**Keywords:** HDR, image-based lighting, rendering, spectral uplifting

**CCS Concepts:** • Computing methodologies → Rendering

## 1. Introduction

The last few years have seen a significant improvement in the field of spectral rendering due to its ability to simulate light transport in a physically correct manner. As opposed to tristimulus rendering, where the colours are represented as an RGB value, spectral renderers model colour stimuli as they occur in nature, which is a distribution of wavelengths. This allows for a physically correct simulation of light transport and results in more realistic calculations of reflection, transmission, absorption and so forth. An additional benefit is its capability to simulate natural phenomena, such as fluorescence or phosphorescence.

However, directly creating spectral assets, such as textures or environment maps, is, in most cases, rather difficult. Either their real-life counterparts need to be precisely measured with a spectrometer (or, in case of environment maps, captured with a hyperspectral camera), which is a tedious and complicated process, or they can be modelled in the spectral space, which is very unintuitive for artists. For the purposes of VFX workflows, the preferred pipeline is to model or capture assets in the RGB space, and then convert them into the spectral domain. This conversion process is called *spectral uplifting*.

The relationship between the spectral and the RGB domain is not bijective, as multiple different spectra, called *metamers*, attain the same value when converted to RGB. Therefore, the process of spectral uplifting is not straightforward and a number of techniques have been proposed. The selection of a suitable technique depends on the scene at hand—for example, when uplifting reflectances of objects usually found in nature (such as wood or vegetation), methods producing smooth and simple curves are usually preferred in order to obtain results in accordance with real-life counterparts. On the other hand, the dyes of fabrics tend to have more complex spectra and would therefore benefit from a distinct uplifting approach.

However, most existing spectral uplifting techniques focus mainly on reflectance uplifting, that is, spectral curves that only have values between 0 and 1. For the purposes of emission uplifting, the current general approach is the downscaling of input RGB values into low dynamic range RGB (i.e., the RGB components are bounded by 0 and 1), and then utilising one of the existing reflectance uplifting methods. The resulting spectral curve is then scaled back into the high dynamic range. However, due to the typically more complex and spiky nature of emission spectra, the spectral power distributions obtained this way rarely resemble

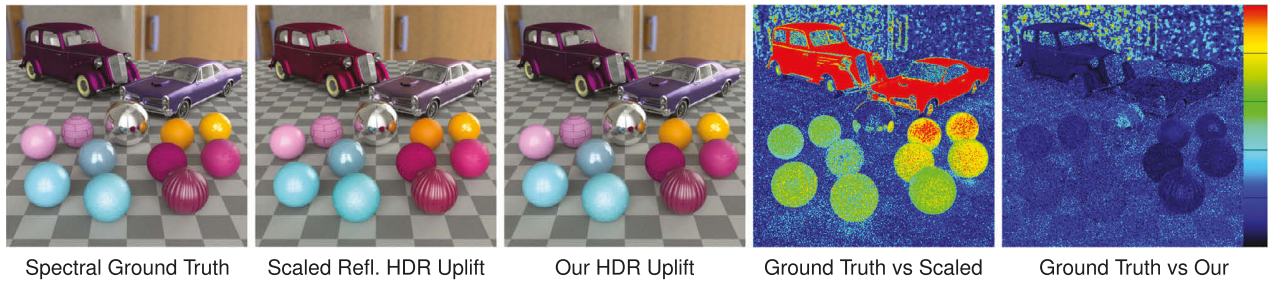


**Figure 1:** Different approaches to rendering image-based lighting. **Ground Truth** uses a spectral HDR environment map as an input, that is, no uplifting is performed. **Scaled Reflectance Uplift** employs the current state-of-the-art environment map uplifting, while **Our Uplift** uses the technique proposed in this paper. Both uplifts take the RGB counterpart of the ground truth spectral map as input. The error images are relative to CIE Delta E 2000 = 5, and the reflectance measurements of the objects in the scene are from the Pantone Atlas. Note that the environment map was obtained as a spectral render rather than a capture for increased precision for comparison purposes.

their real-life counterparts. This, in turn, may cause metamerism artefacts in the final render.

This is a problem in the VFX industry, where it is common to freely mix plate footage and its digital counterpart. These switches pronounce even slight deviations between the two scenes, making the discrepancies visible to the human eye. To prevent this, specific light sources present in the scene are therefore usually uplifted manually, by measuring their corresponding spectral power distributions with a spectrometer. The problematic case is that of image-based lighting, that is, HDR environment maps, where such an option is not easily possible.

In this paper, we present a technique capable of uplifting HDR environment maps for image-based lighting in a manner that simulates real-world behaviour. Our approach builds upon the observation that the emissive properties of pixels in HDR environment maps are mainly due to one dominant light source (or a small set of strong light sources). This, in turn, implies that the spectral power distribution of all pixels must be influenced by the emission spectra of these light sources. With our method, we identify these sources and utilise their spectral power distributions to constrain a universal reflectance uplifting technique in order to obtain plausible uplifts for HDR environment maps.

In the VFX industry, currently, the generally used approach to camera calibration for environment map capture is to use a colour chart. However, such captures do not contain enough information for the proper identification of the present light sources. Therefore, we furthermore propose a novel way in which to perform camera calibration. In addition to maximising the accuracy of our technique, we explain how the process allows the capture to retain valuable spectral information.

## 2. Background

### 2.1. Image-based lighting

In order to achieve a realistic scene appearance, especially in outdoor or more complex settings, the VFX industry relies on the use of image-based lighting via HDR environment maps. During path

tracing, each pixel of the map is treated as a separate parallax-free emitter located at infinity. Although environment maps mainly serve as a tool that aids realism, their incorrect capture and colour calibration can have negative impact on the final render by causing an undesired tint. As different cameras can have distinct spectral response curves, it is easy to obtain such erroneous captures without prior calibration.

Generally, camera calibration is performed with the help of a colour target, such as the Macbeth Colour Checker [MMD\*76], which is a chart with colourful patches that have known reflectance properties. Every patch is assigned a *target RGB value*. First, captures are performed with the colour target in the scene. The captured RGB values of the patches are expected to deviate from the target values, and based on the differences, a colour correction profile is determined. This profile is then applied to the actual environment map footage. The RGB values of the patches are selected so that they provide a wide coverage of the RGB space, thus ensuring better consistency of colour appearance regardless of the camera sensitivity curves.

Although this is a sufficient approach for use in RGB renderers, we note that the proposed calibration is, only a mean of colour correction in order to simulate human perception and therefore achieve a more realistic appearance. It does not provide any meaningful information about the colour properties of the original scene—for example, if the captured patches have a yellow tint, there is no way of identifying whether it is due to the spectral response curves of the camera or, for example, due to a yellowish fluorescent light source. Such captures therefore render the identification of spectral properties of individual objects impossible.

An important tool that addresses the problem of environment map capture for the spectral rendering pipeline, called PhysLight, was introduced by Langlands and Fascione [LF20]. It has the capability of bringing photometric units and other physical parameters to the digital pipeline. However, it also does not attempt to identify the spectral properties of present light sources.

Currently, the only way to achieve such calibration is to use an emissive colour target, such as the camSPECS measurement device [Eng]. It works by emitting a controlled spectrum of light,

which the camera captures and uses to calibrate its colour response. However, the use of such targets is of limited practicality both due to their high cost and restricted accessibility. Their handling may be cumbersome for an average user, due to both their complex calibration and limited portability. Additionally, they are dependent on a stable, controlled environment, which is not always available.

We additionally note that even though most of the objects in an HDR environment map capture are not by themselves emissive, their emissive properties in the final image are due to the dominant light source(s) being reflected off a non-emissive surface. Specifically, the final spectral power distribution of a pixel can be computed as a per-wavelength multiplication of the reflectance spectrum  $R(\lambda)$  of the object and the incoming emission  $E(\lambda)$  that reaches the object. We utilise this observation in this work.

## 2.2. Spectral uplifting

Since spectral rendering as a research area is comparatively new, there is not a very large variety of spectral uplifting techniques, and many of those that exist are limited. Initially, research was not even focused on the final curve shape, but rather on satisfying the most important constraints of a proper spectral uplifting technique—specifically, a negligible round-trip error between the original RGB and the RGB the uplifted curve evaluates to, and, in case of reflectance uplifting, a proper boundary on the curve's values (i.e., it has to be bounded by 0 and 1). Successful evaluation of the techniques for the whole gamut (e.g., sRGB) also posed a problem. Therefore, although the initially proposed methods, such as by MacAdam [Mac35], Meng et al. [MSHD15] or Otsu et al. [OYH18] significantly advanced the field of spectral uplifting, they lack in the fundamental aspects.

The first widely used technique was proposed by Smits [Smi99]. Although it is also prone to minor round-trip errors and does not necessarily satisfy the [0,1] boundary constraint, it is simple and efficient for use during the spectral rendering process. Additional focus of the technique was on the physical plausibility of the uplifted spectra.

To counter the deficiencies of the method by Smits [Smi99] and to address the blockiness of the resulting spectra, Jakob and Hanika [JH19] proposed a method that can be considered state of the art for general reflectance uplifting. In their work, they present a low-dimensional parametric model for spectral representation, which stores spectra with only 3 floating-point coefficients. The simplicity of the model allows them to precompute a set of RGB to spectra mappings, which they store in a 3D table. The uplifting itself is then performed by a lookup in the table, and, in case the desired RGB value is not present, the spectra of its closest entries are interpolated. This approach both achieves smooth reflectance curve shapes similar to those found in nature and satisfies the fundamental requirements of a correct uplifting technique. As this technique was originally proposed for standard reflectances within the sRGB gamut only, the work by Tólová et al. [TWF22] extends it to support Adobe Wide Gamut RGB. To simplify the lookup, they use an evenly-spaced RGB cube as the uplift model instead of the proposed 3D table.

As the method by Jakob and Hanika [JH19] finally solved the issue of satisfying the fundamental uplifting constraints, it allowed research in the area of spectral uplifting to focus on improving the physical realism of the uplifts based on specific material properties. Their model is, for example, used as a basis for the work presented by Jung et al. [JWH\*19] in order to uplift a wider colour gamut by adding fluorescent components. The work by Tólová et al. [TWF21] also takes inspiration from the pre-computed uplift model and proposes the novel idea of constrained reflectance uplifting, which allows the user to preserve specific spectral shapes during the uplifting process. This aids in preserving desired metameristic artefacts when matching plate footage to its digital counterpart in the VFX industry. This method is later extended for support of Adobe Wide Gamut RGB [TWF22]. Van de Ruit and Eisemann [VDRE23] also address the problem of metamerism during uplifting. They propose a method that selects the most plausible metamer by allowing the user to define texture appearance under multiple illuminants. Belcour et al. [BBG23], on the other hand, propose a technique that uplifts to a family of metamers rather than a single spectrum, allowing the user to select the preferred uplift.

Although recent years have seen significant advancements in the area of spectral uplifting, most of the proposed techniques focus on reflectances only. The main reason for that is the lack of emissive objects in a scene in comparison to reflective surfaces. Additionally, in the VFX industry, the main light sources of the scenes are always going to be uplifted manually, by performing measurements on the set. This is because of their significant influence on the scene appearance and therefore a need for high precision.

Currently, general emission uplifting in common spectral renderers is performed by downscaling the input HDR values into the low dynamic range and utilising a known reflectance uplifting method (for example, the Mitsuba renderer uses the technique by Jakob and Hanika [JSR\*22], while the Manuka renderer uses a modified version of the method by Smits et al. [FHL\*18]). The resulting reflectances are then scaled back into the high dynamic range and are therefore considered emissive. In terms of the round-trip error, the results of this approach are satisfactory, however, the final spectra are only synthetic and do not correspond to real-life data. In contrast to reflectance uplifts, where this does not cause a problem, as the shapes of the synthetic spectra resemble real-life reflectances, emission spectra tend to attain much more complex and spikier shapes. Especially in the case of indoor light sources, such as LED or fluorescent lamps, the emission uplifts significantly differ from the actual measurements. This may, in turn, cause metameristic artefacts in the final render. While these can be avoided by manually uplifting the light sources from measurements, this is not an option for the case of image-based lighting, where they remain prevalent.

Both our previous work [TW24] and this extension address this issue by constraining the uplifting process of input HDR environment maps with the illumination that was present during their capture.

## 3. Environment Map Uplifting

Our proposed uplifting method consists of two parts that can be considered separate processes. The first part involves an analysis

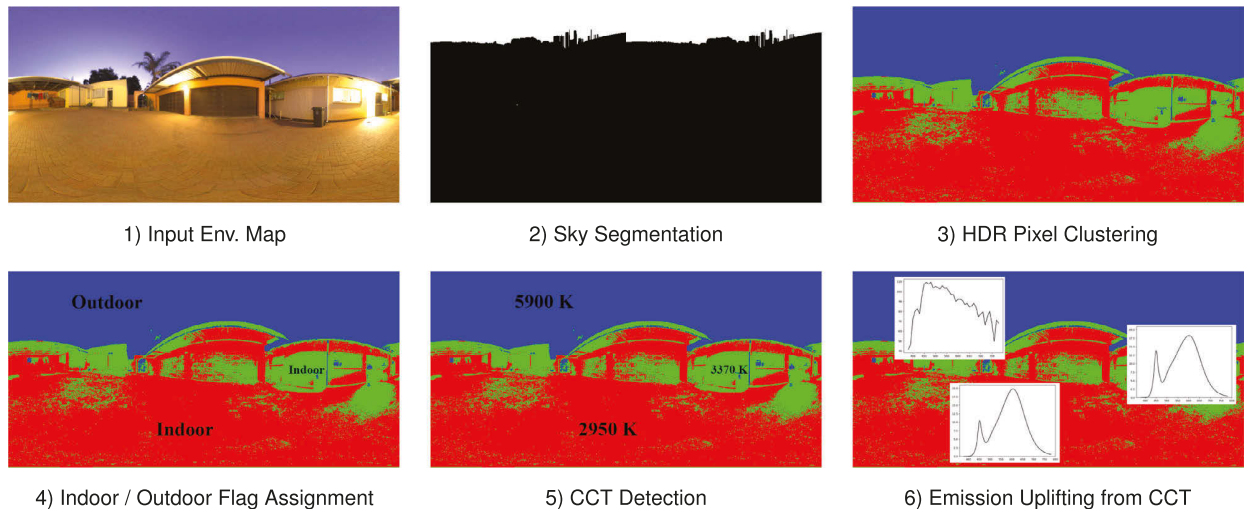


**Figure 2:** Individual steps of our proposed light source detection process shown on an input environment map.

of the input HDR environment map in order to identify its main light sources and their emission spectra. The second part consists of per-pixel uplifting of the environment map constrained by the identified illuminants.

### 3.1. Light source identification

In this section, we describe our proposed solution to light source identification in input HDR environment maps. Our implementation consists of multiple parts—first, we perform detection of the most luminous light sources in the map and identify which pixels they affect. Second, we determine whether the light sources are indoor or outdoor and establish their correlated colour temperatures. We use this information alongside a database of measured spectra to determine their spectral power distribution.

We provide an overview of this process applied to an input environment map in Figure 2. In the following, we describe the individual steps of the process in more detail.

#### 3.1.1. HDR pixel clustering

At first glance, light source identification in an input RGB environment map image appears to be an image segmentation problem requiring a robust trained neural network. However, our analysis of the HDR pixels of existing environment maps gives rise to a more elegant solution.

Every neutral light source has a specific correlated colour temperature—for example, indoor tungsten sources tend to have warm temperatures around 2000 K, while daylight illumination typically reaches the temperature of 6500 K. This results in a colour cast that is transferred to the objects illuminated by the light source. Specifically, in HDR environment maps, pixels are tinted towards yellow or blue depending on which light source they are affected by the most. While the colour difference between pixels in the lower dynamic range (i.e., the pixels' luminosity is lower than the average in the image) is too small to be able to distinguish any type of

colour cast, in the higher dynamic range, even slight shifts in correlated colour temperature represent significant changes in the RGB colour distance.

In Figure 3, we present a set of HDR environment maps and a visualisation of their pixels in the 3D RGB space. Although the pixels with lower luminosity values tend to create a seemingly random cluster in the low dynamic range, in the high dynamic range, we can observe rather distinguishable clusters forming around certain axes. We call these clusters the *light source clusters*, since the highest luminosity values of each of them belong to light sources of a similar temperature. Upon closer inspection, we further observe that the rest of the pixels in each cluster belong to areas that are primarily illuminated by light sources of this temperature.

In order to identify the visible clusters, we implement a modified version of the K-Means clustering algorithm. For each input point, in addition to storing its RGB coordinates, we also compute its spherical coordinates - specifically the angles  $\theta$  and  $\phi$ . The means (centroids) also carry this information. When assigning a point to its nearest mean, as opposed to the least squared Euclidean distance that is used as a distance metric in the standard K-Means algorithm, we utilise the least squared distance between the  $\theta$  and  $\phi$  angles. By omitting the radial distance  $r$  from the calculation, we force the algorithm to create clusters based on the points' relative angular position from the origin rather than their Euclidean distance from each other. This, in turn, forces the points to cluster around specific axes.

As they have no informative value for the algorithm and their processing only hinders performance, we omit the pixels in the low dynamic range from the clustering. We assign them to their corresponding clusters only after its termination, by utilising the same distance metric as in our modified version of the K-Means algorithm.

The final aspect left to determine is the number of clusters. As the standard K-Means algorithm takes the desired number of clusters as a parameter on input (denoted  $k$ ), the general approach is to iteratively run the algorithm for an increasing  $k$ , and design a cluster

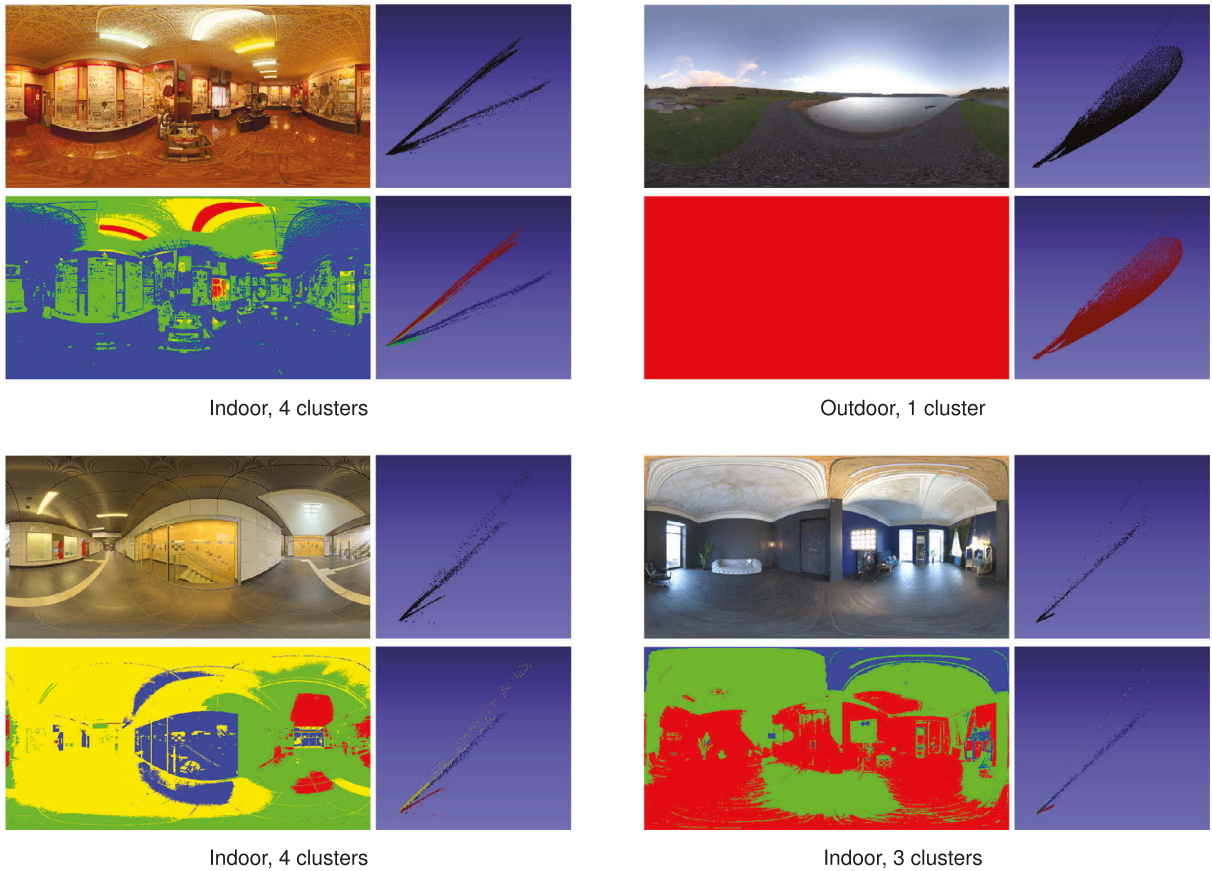


**Figure 3:** Our modified version of the K-Means algorithm applied to 4 input HDR environment maps. For every environment map, we visualise: its pixels in the RGB space; its colour-coded clustered version (one colour belongs to one cluster); a colour-coded visualisation of its pixels. Note that pixels affected by distinct illuminants of similar temperatures fall into the same cluster.

sufficiency metric based on heuristics that identifies the most desirable clustering. We also implement this approach, and design a set of heuristic rules based on the most common properties of environment maps—for example, we do not allow more than 1 outdoor cluster, we discard clusterings that result in clusters with similar colour temperatures, we do not allow more than 6 clusters overall (as it generally results in overclustering, which hinders performance) and so forth.

Such a heuristic approach is bound to have its deficiencies. In our situation, these are most pronounced for corner cases, such as indoor settings with a lot of small lamps or a night sky capture covered with bright stars. While we believe that some of the shortcomings could be resolved using a distinct approach, such as employing a neural network, we find the current algorithm sufficient for our purposes, especially since its design was not the main goal of the paper. Additionally, we note that even the most robust methods proposed for the problem of environment map segmentation are prone to failure on certain inputs.

We present the results of our proposed clustering on a couple of example environment maps in Figure 3. We note that the assumption of cluster exclusivity (that is, one pixel belongs to one cluster), is

not entirely correct, as in real life, objects are often illuminated by more than one light source. However, this assumption does not have a significant effect on the final result. This is because the effect of the environment map on the rest of the scene is mainly determined by the spectral uplifts of the pixels with the highest luminosity, whose emission is generally a result of exclusively one light source (as they either belong to the light source or are extremely close to it).

### 3.1.2. CCT detection

The general idea behind determining the emission spectrum of a cluster's light source is to first determine its correlated colour temperature (or *CCT*), and then utilise existing light source measurements to identify the one that attains this temperature.

We explored multiple approaches to most accurately determine the CCT of a cluster, such as picking the most luminous pixel, using linear regression to fit a line through the cluster and so forth. Our final and most accurate solution works as follows:

First, the clusters are divided into *indoor* and *outdoor* clusters depending on whether the cluster contains any portion of the sky. The division is performed with a simple sky segmentation algorithm,

specifically the one proposed by Shen and Wang [SW13]. While this algorithm sometimes fails to recognise the specific edges (see e.g., Figure 2), we employ it solely for the purpose of determining the presence of sky, for which it performs sufficiently. Note that this approach manages to classify even, for example, outdoor street-lamps as indoor clusters (as their illumination rarely affects the sky pixels), which is the desired behaviour.

To determine the CCT of the indoor clusters, we utilise the results of the K-Means algorithm. Using McCamy's approximation [McC92], we convert the RGB values of the clusters' means to their corresponding correlated colour temperatures, which are then established to be the final CCTs.

Unfortunately, we found this approach to perform inadequately for specific corner cases in outdoor settings—particularly for sunset and sunrise environment maps captured when the sun is just below the horizon. In such cases, the mean CCT was not able to accurately balance out the extremely saturated red or yellow tints attained at the horizon with the cool colour cast of the rest of the capture. We address these cases by applying heuristics and averaging the CCT of the cluster mean with the CCT of the pixel with the highest luminosity in the cluster, which we found to result in a much closer final estimation. We avoid the need to detect these corner cases by applying this heuristic to all outdoor clusters, since for daylight illumination, the CCT of the pixel with highest luminosity is practically identical to the CCT of the mean.

We note that we do not perform sky segmentation only to address a specific corner case, and that the information about cluster type is also utilised for the purposes of uplifting emission from CCT as explained later in Subsubsection 3.1.4.

### 3.1.3. Environment map calibration

The CCT detection process heavily relies on the light sources to attain colour values identical to their real-life properties. However, as previously mentioned in Subsection 2.1, the current environment map capture and calibration process only aids with simulating human visual perception. And while there exist methods that are capable of preserving this information (i.e., using an emissive colour target such as camSPECS [Eng]), they are too cumbersome and costly to use in practice.

We therefore propose a novel capture process for the purposes of a spectral rendering pipeline—specifically, we propose to additionally calibrate the camera according to a light source with a known spectral power distribution that is, in the same manner as the colour target, manually placed and captured in the scene. For our work, we use a multi-LED light source that simulates the spectrum of the D65 distribution (specifically, we use Waveform Lighting's ABSOLUTE SERIES LED D65 Module). While the ACES colour space, which is generally used for production workflows in motion pictures, has a different white point, we chose to use D65 as it is the white point of most current RGB spaces. We, however, note that our proposed technique would work in an identical manner for any chosen white point.

The capture therefore contains both a colour target and a light source. The calibration process itself is then twofold—first, the

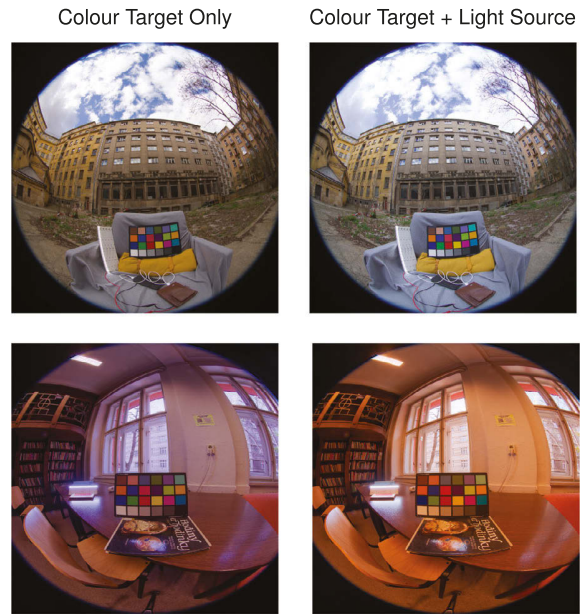


**Figure 4:** Our proposed calibration process shown on examples of environment maps. **Left.** The capture is calibrated with the Macbeth Colour Chart only. **Right.** The capture is additionally white balanced according to the light source (i.e., the light strip present in the images). In the calibrated captures, the pixels of the light source therefore attain the RGB value of (1,1,1) (in sRGB).

standard colour target calibration is performed. This results in the change of colour for the whole image, including the light source. As we know the goal RGB value of the light source (in our case, it is  $RGB = (1, 1, 1)$ ), we can obtain a white balance matrix that transforms the image into a colour space, where we can properly distinguish the colour cast. To do so, we use the von Kries chromatic adaptation method [Fai20], with the source white point being the current RGB value of the light source and the destination white point being the goal RGB of the light source (in our case,  $RGB = (1, 1, 1)$ ). We note that the selection of the white balance matrix was only due to personal preference, and that utilising a different one (e.g., the CIECAM02 matrix) would not yield qualitatively different results.

We present examples of environment maps captured in the proposed manner in Figure 4, both before and after the light source calibration. We note that while this process is essential for the method to work perfectly, it does not render our technique useless for environment maps calibrated using a colour target only. Especially for clear daylight illumination, we do not expect significant changes of the image's colours. However, in such cases, we must warn against the possibility of incorrectly estimated emission, which may in turn result in a decrease of realism of the final uplift.

### 3.1.4. Emission uplifting

To determine the correct emission spectrum for an input correlated colour temperature, we implement different methods depending on the type of the light source. In the following, we review the light

source categories that we support, along with their viable input CCTs, and the approaches to their uplifting:

**Daylight (over 5000 K).** In addition to the standard daylight CIE illuminants (D50, D55, D65 and D75) whose temperatures range from roughly 5000 K to 7500 K, Judd et al. [JMW\*64] defined a method that computes the spectral power distribution of a D-series illuminant (i.e., emission of natural daylight) for colour temperatures also outside of this range. Our uplifting therefore utilises the linear interpolation of D-series CIE illuminants for input CCTs of values from 5000 K to 7500 K, and performs the D-series illuminant computation by Judd et al. [JMW\*64] for inputs over 7500 K.

**Sunset/Sunrise (2200 K–5000 K).** To obtain sky emission spectra at sunset or sunrise, we utilise the Prague Sky Model presented by Wilkie et al. [WVBR\*21] and its implementation proposed in the later extension by Vévoda et al. [VBRKW22]. We locked 4 of the model's 5 parameters to values that simulate sunset the closest (specifically, we set *ground albedo* to 0, *solar azimuth* to 90 degrees, *camera view* to side-facing fisheye and *ground level visibility* to the maximum value of 131.8 kilometres). We then performed multiple renders with varying levels of *solar elevation* ranging from 0 to 20 degrees, as higher elevation values can already be considered daylight. For each of these renders, we obtained the emission spectrum of its most luminous pixel, which resulted in a list of spectra with temperatures ranging from 2200 K to 5000 K stored in an ascending order. The final spectrum is obtained by a linear interpolation of two neighbouring spectra from this list in terms of CCT. Since any two neighbouring spectra are close to each other in terms of curve shape, this approach does not cause any distortions or colour artefacts.

**LED Light Source (1700 K–30,000 K).** In their paper, Kokka et al. [KPB\*18] present a large database of over 1500 measured LED light sources, from which they compute 5 representative distributions with colour temperatures ranging from 2700 K to 6500 K that are currently the CIE LED standard distributions. As the temperatures of LEDs can span a significantly wider range, we pick additional 15 distributions from the provided measurements, ranging from 1700 K to 30,000 K. To ensure proper coverage of the 2700 K–6500 K range and to avoid any interpolation artefacts, we additionally add 4 more spectra, summing up to the overall list of 19 distributions. The uplifting itself is then also performed as an interpolation of the two closest neighbouring spectra in terms of CCT. We note that LEDs with temperatures over 20,000 K are not suitable for regular lighting purposes—however, we offer this possibility for specific corner cases.

**Fluorescent Light Source (2900 K–6500 K).** Similarly to sunset and LED spectra, we obtain a set of fluorescent emission distributions and perform their interpolation according to the input CCT. So far, we only support the CIE standard fluorescent illuminants, which are the F1–F6 lamps from the CIE Illuminant series F. Since other available fluorescent lamp measurements have distinct spectral shapes, performing their interpolation with any of the F1–F6 measurements is undesirable, as it would provide unrealistic results.

**Incandescent Light Source (1000 K–3000 K)** The spectral power distribution of the emission  $M$  of an incandescent object heated to a temperature  $T$  is given by the Planck's law, which fol-

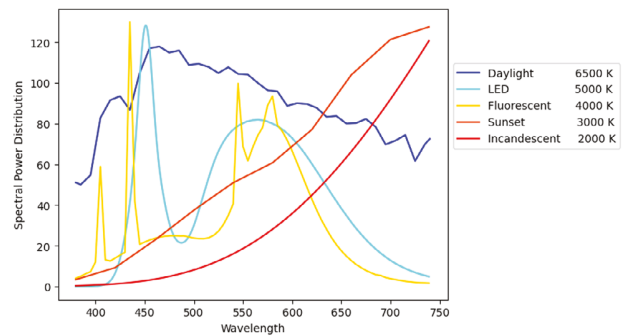


**Figure 5:** Spectral shapes of different light source types obtained with our HDR environment map uplifting system. Note the complexity of the shapes of the LED and fluorescent light sources in comparison to, for example, daylight or an incandescent light source—when used to illuminate an object with a smooth reflectance curve, it is evident that the former are prone to cause visible metamerism artefacts.

lows:

$$M(\lambda, T) = \frac{c_1}{\lambda^5} \frac{1}{\exp\left(\frac{c_2}{\lambda T}\right) - 1}$$

where  $c_1$  is the first radiation constant and  $c_2$  is the second radiation constant. We utilise this equation to compute the final incandescent emission spectrum for an input temperature  $T$ .

While the resulting emission spectra obviously differ depending on the input temperature, their general shapes remain the same throughout every light source category. We visualise the emission shapes that our system is capable of obtaining in Figure 5.

To distinguish the light source type of each cluster, our system takes advantage of the *indoor* and *outdoor* flags obtained during CCT detection (see Subsubsection 3.1.2). Depending on their CCT, outdoor clusters use either the *daylight* ( $CCT \geq 5000$  K) or the *sunset* ( $2200 \leq CCT \leq 5000$  K) uplifting method. Note that our decision to uplift to daylight illumination as opposed to direct sun illumination is motivated by the typical composition of outdoor settings, where daylight sky is the most dominant. Additionally, in the visible range, the D-series illuminants are a reasonable approximation of solar radiance [Kur84], and therefore utilising sun illumination measured during daylight would provide similar results.

Unfortunately, the input environment map captures do not contain enough information for us to be able to accurately determine the type of indoor light sources. Therefore, all indoor light sources are treated as LED unless otherwise specified by the user. We do not see this as a severe shortcoming of our approach, as it is reasonable to ask users what basic types of illumination are present in a capture.

We note that while some of our proposed uplifting scenarios perform linear interpolation of two spectra based on their input CCT, this relationship is not linear. Therefore, the final spectrum will not be evaluated exactly to the desired temperature. However, in practice, this does not pose a problem. As the resulting CCT cannot be outside of the range of the neighbouring spectra, and as the

temperatures of the distributions are sampled densely, the error is minimal to cause any visible colour distortions.

### 3.2. Uplifting from light source

The process of uplifting a specific input HDR pixel is based on the simple fact that its emissive properties are due to the combination of the object's original reflectance and the incoming light, specifically:

$$P(\lambda) = E(\lambda) \cdot R(\lambda)$$

where  $P(\lambda)$  is the final SPD of the pixel,  $R(\lambda)$  is the reflectance of the object the pixel belongs to and  $E(\lambda)$  is the incoming emission that hits the object in the original scene. We simplify this observation by making the assumption that  $E(\lambda)$  is only a result of one specific light source (i.e., the cluster's light source). As previously explained in Subsubsection 3.1.1, with regard to the realism of the final uplifts, this assumption is acceptable. Therefore, to obtain the final uplift  $P(\lambda)$ , the only variable that remains to be determined is the object's reflectance  $R(\lambda)$ .

To do so, we utilise a reflectance-uplifting method. We specifically take advantage of the wide gamut sigmoid uplift cube implemented as part of the work by Tólová et al. [TWF22], which is technically the uplift model proposed by Jakob and Hanika [JH19] extended for support of Adobe Wide Gamut RGB. We select this model due to its favourable results in the area of general reflectance uplifting, as it creates smooth and simple curves similar to those of real-life objects (e.g., wood, vegetation, soil, etc.), which is what typical environment maps tend to consist of.

As previously mentioned in Subsection 2.2, the uplift cube consists of evenly-spaced lattice points that contain a mapping from their coordinate (or RGB value) to a coefficient representation of a reflectance spectrum. This spectrum then evaluates to the RGB value of the lattice point.

However, every RGB value in the cube is already stored *with respect to a white point*. In practice, this means that the reconstructed curve is first multiplied by the illuminant of this white point and only then is the final spectral power distribution converted to its RGB counterpart. For this purpose, both the model proposed by Jakob and Hanika [JH19] and its Adobe Wide Gamut RGB extension [TWF22] use the white point of the D65 daylight illuminant. To determine the reflectance of the objects in our scene, though, we need to know their properties with respect to the white point of the distinguished light source as opposed to D65.

While it is possible to create a new model in a similar manner as proposed in the previous works (i.e., with the process of *cube fitting*), we found this approach to be too costly to perform on the fly. Instead, we make use of the already existing D65 cube and create the new model by reconstructing the reflectances of all of the D65 cube's points and determining their RGB values under the cluster's identified illuminant.

As the conversion of a spectrum to RGB is not a linear operation, the resulting structure does not necessarily have to be an evenly-spaced cube. As shown in Figure 6, this transforms both scales and skews the model. Additionally, as the wide gamut cube also contains empty voxels that do not have viable reflectance mappings,

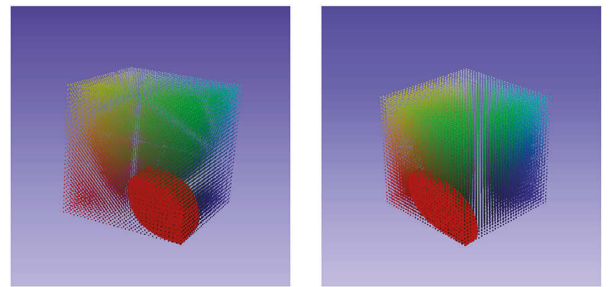


**Figure 6:** Comparison of the wide gamut reflectance uplift cube to our reflectance uplift model (visualised in red) constrained by a LED spectrum with a temperature of roughly 5000 K (left) and a sunset spectrum with a temperature of roughly 2700 K (right). Note that the scale of the models is proportional to the scale with which the illuminants are stored, and does not affect the final uplifting results.

the model loses its original cube shape and rather attains a blob-like shape of the Adobe Wide Gamut RGB colour space. Therefore, as opposed to the regular cube, performing a constant lookup in the structure based on the input RGB value does not guarantee that we will obtain the correct voxel corners for trilinear interpolation. We address this by still utilising constant lookup and, if its results are unsatisfactory, by moving into neighbouring voxels depending on the neighbours' coordinates. We note that, due to the skewing of the model, the trilinear interpolation does not necessarily have to be performed within a voxel, but rather between the closest 8 surrounding points. This penalises the lookup process in terms of execution time. However, we find the performance overhead to be worth the improvements in colour accuracy (see Subsection 4.3, specifically 4.3.1).

Although this model achieves proper round-trip when uplifting under the identified illuminant, it is still bounded and therefore unsuitable for all HDR pixels. We address this in the same manner as the current state-of-the-art emission uplifting, that is, with *scaling*. The scaling factor is determined in the same manner as the current emission scaling in Mitsuba 3, which follows:

$$\text{scale} = 2 \cdot \max(rgb.r, rgb.g, rgb.b)$$

This ensures unproblematic uplifts of all values as opposed to just using the maximum component and attempting to uplift at the gamut boundary. The final uplift is then obtained as:

$$P(\lambda) = \text{scale} \cdot E(\lambda) \cdot R(\lambda)$$

where  $R(\lambda)$  is the reflectance obtained from the model created for the white point of  $E(\lambda)$ . This approach ensures the proper scaling of the illuminant and therefore prevents the loss of spectral shape information.

Lastly, we address the problem of out-of-gamut input pixels. As the emission spectrum of the light source is only an estimation, it may happen that some of the pixels in the image fall outside of the gamut of the uplift model regardless of its scale. This is usually the case of dark pixels close to  $RGB = (0, 0, 0)$ , which suffer from the skewing. As such pixels are barely affected by the light

source anyway, we address these cases by employing the standard scaled emission uplifting with the D65 cube. For the rare cases of HDR out-of-gamut pixels, we also support gamut mapping. Similarly to the wide gamut cube, the process maps to the closest point within the model.

Currently, the uplift model for every cluster is created prior to the actual uplifting process and is stored in memory. Each pixel then contains a pointer to the uplift model (or cluster) it belongs to. As we do not allow more than 6 clusters per environment map (see Subsubsection 3.1.1), this does not significantly affect memory requirements. The uplifting itself is then performed per pixel.

## 4. Results

The evaluation of our technique consists of three parts. First, we prove that our method is technically sound by assessing the round-trip error for a diverse and extensive set of environment maps. Second, we evaluate how our technique improves the current state of the art by comparing a set of ground truth hyperspectral environment maps to both our and the state-of-the-art uplifts of their RGB counterparts. Last, we address the performance overhead of our method in comparison to the current state of the art, both in terms of execution time and memory requirements.

Due to our lack of access to commercial spectral renderers, we present our uplifting system as a standalone implementation. The input is an HDR environment map, and the output an uplift file that contains mappings from individual pixels to their corresponding spectra.

In order to see the performance of our method in terms of the final colour deviations in practice, we incorporated this uplift file for environment map uplifting in the Mitsuba 3 renderer. Unfortunately, the spectral variant of Mitsuba 3 has a hard-wired 3 coefficient representation for every spectrum, which is incompatible with the shape of our uplifted spectra. To fully integrate our solution into the renderer, we would have had to redesign its low-level data structures, which was deemed to be outside the scope of this work. Therefore, we use our implementation in the Mitsuba 3 renderer only for visualisation purposes (e.g., to create Figures 1 and 8). All colour accuracy and performance tests are carried out in our standalone implementation.

For evaluation purposes, our uplifting system also supports the current state of the art, that is, the *scaled reflectance uplifting*. We specifically use a variant of the technique used in the Mitsuba 3 renderer, however, we can expect the scaling of any other type of smooth reflectance spectra to perform similarly.

### 4.1. Uplift accuracy

To evaluate the round-trip error, we compile an extensive set of HDR environment maps. We make sure to encapsulate a variety of different scene settings—both indoors and outdoors; with one or multiple distinct illuminants; with varying light source temperatures; captured at different times of the day. For each environment map in the set, we perform our proposed uplift and obtain its RGB counterpart. We then compare the uplifted RGB image to the original input im-

age by means of the CIE Delta E 2000 metric. To cover all proposed uplifting scenarios, we treat the light sources in indoor environment maps as LED, fluorescent and incandescent respectively and, if applicable, perform a different uplift for each light source type.

On average, we obtain an error of only  $\Delta E = 4.85 \times 10^{-12}$ , while the maximum Delta E achieved is  $\Delta E = 6.53 \times 10^{-12}$ . Generally, colour differences of  $\Delta E \leq 1$  are considered to not be perceivable by the human eye [MT11], which our method definitely satisfies. The pixels that are not uplifted with our model (i.e., the pixels that fall out of its gamut and are therefore uplifted with the D65 cube) take up only 0.0035% of the input and none of them are in the high dynamic range. We can therefore claim that the distinct approach to their uplifting does not reduce the realism of the final uplift.

Of the 166 performed uplifts (counting in the multiple uplifts of indoor environment maps), we found 2 to have pixels out of gamut. On average, the out-of-gamut pixels amounted to 0.000016% of the maps. In practice, this is barely visible to the human eye—however, when matching plate footage to its digital counterpart in the VFX industry, even a couple of erroneous pixels can cause noticeable artefacts. In some cases, we measured errors as high as  $\Delta E = 25$ , which is worrisome in terms of the final appearance. We attribute these errors to the insufficient estimation of the light sources in the scene. We specifically found the biggest deficiency of our pipeline to lie in the CCT detection process, and we strongly suggest focusing on its improvement as future work. However, as the focus of this paper was on spectral uplifting rather than white balance and clustering, we consider the overall accuracy of our method to be satisfactory.

### 4.2. Comparison to the state of the art

In order to determine how our technique improves the current state-of-the-art, we perform comparisons of the following three spectral environment maps: the *ground truth*, that is, an environment map captured with a hyperspectral camera; the *scaled reflectance uplift*, that is, a spectral environment map acquired by uplifting the RGB counterpart of the ground truth with the scaled reflectance uplifting technique; and *our uplift*, which is obtained by applying our technique.

We determine the level of similarity between two spectral environment maps by their effect on the appearance of multiple reflectances when treated as a light source. For each pixel and its two uplifts treated as emission, we iterate over multiple colour atlases of reflectance measurements and compute the RGB of the reflectances under both uplifts. To determine their difference, we once again use the CIE Delta E 2000 metric. The atlases used are the Munsell Book of Colour (1598 samples), the Pantone Colour Matching System (1853 samples) and the Macbeth Colour Chart (24 samples). We note that the proposed test is performed in an isolated environment, that is, in a setting with only a single illuminant and a single Lambertian surface. No rendering or path tracing is performed, and the final colour is obtained by a simple multiplication of the present emission and reflectance spectrum and a subsequent conversion into RGB. Therefore, the results in terms of absolute error measurements do not convey the exact colour error that would be present if both techniques were to be, in turn, applied for the

purposes of environment map uplifting in a state-of-the-art spectral renderer. The final absolute colour error can either be greatly accentuated or diminished, depending on the different types of light interactions with distinct materials during path tracing. Therefore, the more meaningful measure obtained during this test is rather the *relative* colour difference, that is, the Delta E 2000 ratio, between the two techniques. This, on average, remains the same even if applied to more complex scene settings.

While our proposed test is robust insofar as it tests our method's performance on the whole of the Adobe Wide Gamut RGB gamut through the colour atlases, its main drawback is the lack of ground truth data, that is, hyperspectral environment maps. As we do not possess means to perform hyperspectral captures, we rely on existing resources. Specifically, we opted for 4 large datasets from real-world settings (by Morimoto et al. [MLNS24], Chakrabarti and Zickler [CZ11], Kider et al. [KJKN\*14] and the HSSOD dataset [IOZ\*18]), as they, to our best knowledge, most closely align with our requirements. However, similarly to other available data, they also lack in three regards.

First, the data is usually inadequate in certain aspects which are crucial for image-based lighting—for example, the measured values are bounded ([MLNS24], [CZ11]) or the captures are not a 360-degree view but rather a closeup of a small object ([IOZ\*18], [CZ11]). Therefore, for most of the datasets, our technique requires custom adjustments (i.e., scaling of values or forcing certain types of uplifting due to the unreliability of the sky detection process). Second, there are very few indoor captures available, and those that exist do not contain information about the type of present illumination. Third, the capture process consists of a number of steps, none of which are flawless [PHG19]. For example, the results of both colour calibration and geometric calibration may be hindered by imperfections in the target (e.g., a white patch is only 99% white). System stabilisation is susceptible both to human error and to limitations of the used technology, and even environmental conditions, such as wind or dust particles, may introduce noise when present during the capture. Each of these factors can decrease the accuracy of the final measured spectra and, as a result, lead to their deviations from what happens in nature. As our goal is to assess accuracy, we find this to be the most worrisome aspect.

Therefore, in addition to the existing captures, we create our own spectral environment map dataset in terms of renders. Specifically, we use the ART renderer [Wil18] to obtain 20 distinct outdoor environment maps (using the sky model by Wilkie et al. [WVBR\*21] and Vévoda et al. [VBRKW22]), and the Mitsuba 3 renderer to obtain 60 indoor renders—20 using LED lighting, 20 with fluorescent light sources, and 20 with incandescent illumination. In order to cover all possible scenarios, the temperature of the illuminants in individual renders is evenly sampled across the supported CCT range.

As both used renderers are physically based and all the materials of the scenes are defined with physically-plausible spectra, the process of light transport is almost identical to what would happen in nature. However, in contrast to the existing datasets, all inaccuracies caused by performing manual hyperspectral measurements are eliminated. This makes the results of the renders even closer to real world than captures. Additional benefit of this dataset is our ability to cover a wide range of cases and, as we possess knowledge of the

scene's original illuminant, our capability to analyse the accuracy of individual steps of the proposed pipeline.

The evaluation of our method is therefore performed on both a set of existing datasets and our own set of 80 rendered environment maps. Specifically, to test the accuracy of outdoor uplifting, we use 160 spectral captures obtained from the following datasets: 60 captures from the HSSOD dataset [IOZ\*18], 50 daylight captures by Chakrabarti and Zickler [CZ11], 20 sky measurements by Kider et al. [KJKN\*14], 10 hyperspectral environment maps by Morimoto et al. [MLNS24], and 20 of our own custom renders from the ART renderer. The indoor uplifting is tested on 27 hyperspectral captures performed by Chakrabarti and Zickler [CZ11], and on a set of 60 renders from the Mitsuba 3 renderer.

#### 4.2.1. Outdoor uplifting

First, we assess the accuracy of the outdoor uplifting. As mentioned previously in Subsection 3.2, the current state-of-the-art technique utilises the scaled results of the D65 cube for the purposes of HDR uplifting. So if the illumination of the scene is determined to be natural daylight, the estimated spectral power distribution of the light source is bound to be extremely close to D65 in terms of spectral shape. Therefore, our goal is to obtain results very similar to the state of the art for natural daylight, with our technique slightly outperforming in cases where warmer or cooler temperatures are present, and significantly outperforming for extremely warm sunset or sunrise settings (due to visibly distinct spectral shapes of the illuminants).

We provide the results of our measurements in Table 1a. These show that both techniques perform very similarly in terms of the final spectral shape. The observed differences are too small to clearly determine whether the error is caused by one technique being superior, or rather by inaccuracies in the initial ground truth measurements. We attribute them to a combination of the two. However, a noteworthy observation can be made when examining the error for the dataset by Kider et al. [KJKN\*14], which consists of precise sky measurements that are not susceptible to capture errors. Here, our technique outperforms the current state of the art, which implies that its results are closer to real-world natural light measurements. On the other hand, our suboptimal performance for the HSSOD database [IOZ\*18] can be attributed to the calibration of its images. Although they were captured during daylight, they contain warmer, sepia-like tones, which cause our system to incorrectly estimate the final illumination as sunset.

An even more significant observation is the colour accuracy for the *Renders* dataset. As it contains multiple images with sunset settings, we expected our technique to outperform the current state of the art by a notable margin. However, the actual results are only slightly in our favour. Upon closer examination, we attribute this solely to the failure of the CCT detection process, the implementation of which is rather simple and does not account for every possible environment map scenario (see Section 3.1.2). As the goal of this paper was not the design of a CCT detection algorithm, but rather to prove that our pipeline is technically correct, we therefore additionally evaluate how an incorrect CCT estimation affects the colour accuracy of the overall result. To do so, we force the CCT detection

**Table 1:** Accuracy of our proposed (a) **outdoor** and (b) **indoor** uplifting method and the current state-of-the-art uplifting (i.e., the scaled reflectance uplifting) when compared to real-world hyperspectral measurements from distinct datasets.

(a) Outdoor uplifting			
Dataset	Images	Scaled refl. $\Delta E$	Our $\Delta E$
HSSOD	60	0.81	0.90
Chakrabarti and Zickler	50	1.33	1.31
Morimoto et al.	10	0.62	0.57
Kider et al.	20	0.23	0.17
Renders	20	1.19	1.14

(b) Indoor uplifting			
Dataset	Images	Scaled refl. $\Delta E$	Our $\Delta E$
Chakrabarti and Zickler	27	1.25	0.99
Renders LED	20	1.16	0.41
Renders fluorescence	20	0.92	0.34
Renders incandescence	20	0.97	0.48

*Note:* The provided error measurements are the average CIE Delta E 2000 errors caused by illuminating a wide set of reflectances by the ground truth and the two uplifts respectively and comparing the results. Also note that small perceived error differences may not be caused by one technique outperforming the other, but rather by inaccuracies in ground truth captures. Additionally, we emphasise that the error perceived for the *Renders* dataset is mainly caused by incorrect CCT detection and that the differences are much smaller when CCT is established beforehand.

**Table 2:** The effects of correct CCT estimation on the colour accuracy of our uplifting method, evaluated for images from the outdoor *Renders* dataset.

Dataset	Images	Avg $\Delta E$		$\Delta E \geq 1$	
		Scaled refl.	Our	Scaled refl.	Our
Daylight	7	0.56	0.49	12%	10%
Sunset	8	0.70	0.32	26%	4%
Sunset ( $\leq 2k$ )	5	0.87	0.21	29%	2%

*Note:* To better distinguish between different types of uplifting and CCT categories, the images are divided into multiple smaller datasets. Also note that daylight images with  $CCT \geq 10k$  were omitted from the tests, as we do not find them representative of typical lighting conditions.

process to output the correct values and we repeat the tests for the *Renders* dataset.

We provide the results in Table 2. In addition to the average Delta E, it also contains information about the percentage of samples that attain the error over  $\Delta E \geq 1$ . We find this metric especially meaningful, as  $\Delta E = 1$  is the maximum error perceivable by a standard observer. It is clear that once the CCT is correctly detected, our technique behaves exactly as expected.

Lastly, we address the maximum error attained during our tests. While we can observe noticeable improvements (i.e., decreasing the error from  $\Delta E = 35$  to  $\Delta E = 5$  for particular sunset cases, or even from  $\Delta E = 34$  to  $\Delta E = 15$  for daylight settings), we note that the specific values are misleading. This is mainly because the maximum

**Table 3:** Percentage of samples from individual indoor datasets where  $\Delta E > 1$ , measured for tests performed as described in Subsection 4.2.

Dataset	Images	Scaled refl.	Our
Chakrabarti and Zickler	27	48%	35%
Renders LED	20	49%	9%
Renders fluorescence	20	57%	11%
Renders incandescence	20	33%	3%

*Note:* We emphasise the error ratio between our and the scaled reflectance technique, as the absolute Delta E colour errors are mostly dependent on the luminosity range of the input data.

errors are generally achieved for emitters with the highest luminosity, which greatly depends on the capture process and on the scaling of the emission spectra. Therefore, we once again emphasise the importance of relative colour differences as opposed to the absolute error values.

In Figure 7, we present two outdoor examples from the performed tests, along with the achieved spectral shapes and the final colour appearance. While these are mainly for visualisation purposes, we note the spectral shapes and the considerable deviation of the current state of the art from both the ground truth and our technique.

In conclusion, our proposed outdoor uplifting technique improves the current state of the art and can result in significant improvements for warm sunset and sunrise settings. Its only serious drawback is the accuracy of the CCT detection process, which does not diminish the validity of the proof of concept.

#### 4.2.2. Indoor uplifting

In order to test the performance of indoor uplifting on real-life hyperspectral measurements, we utilised the indoor dataset of 27 captures by Chakrabarti and Zickler [CZ11]. As the type of illumination was not provided, we examined the performed measurements and eventually estimated the light sources to be the closest to narrowband fluorescent illuminants, that is, the CIE F10-F12 lamps. To better resemble the original illumination, we additionally performed slight smoothing of the illuminants. We attribute the need for this to either imprecise hyperspectral captures or our inaccurate estimate.

Furthermore, we also perform the tests on our own 3 sets of renders that cover every supported indoor illuminant type and its respective temperature range.

We provide the results of our tests in Table 1b. In all cases, it is clear that our method significantly outperforms the current state of the art. The average error is effectively reduced to at least half in all of the rendered cases, even if the individual steps of the pipeline do not perform exactly as desired. Even the hyperspectral dataset with imprecisely estimated illumination exhibits noticeable improvement. Additionally, in Table 3, we present the percentage of samples that obtained an error of  $\Delta E > 1$ . For all the provided datasets, our technique once again significantly improves the current state of the art.

We emphasise that all of the results obtained for indoor uplifting were achieved with the current version of our system. This means

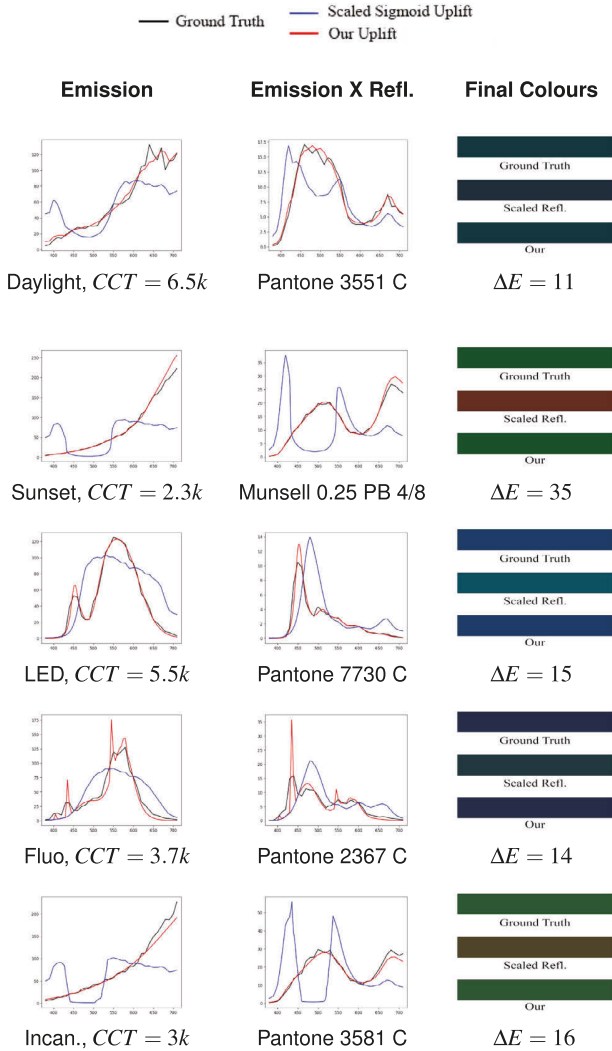


**Figure 7:** Examples of ground truth hyperspectral measurements (black) and their two uplifts (obtained with the current state of the art (blue) and our technique (red)) when used to illuminate specific reflectances from available colour atlases. The first column labelled Emission represents the raw spectral power distribution of the emitter, while the second column labelled Emission x Refl. represents the final SPD when the emission spectrum is used to illuminate the disclosed reflectance patch. Final colours visualises the actual RGB values the spectra in the second column evaluate to. The information regarding the type of applied uplifting, the CCT and the illuminated reflectance patch is available for each image. The provided Delta E measurement is the CIE Delta 2000 error between the ground truth and the state-of-the-art uplift. The Delta E between the ground truth and our uplift remains below 1 for all displayed cases. Note that the colours are visualised in sRGB and their brightness is slightly increased for the reader. Also note that the provided colour error information is only our measured value, and would significantly differ with distinct luminosity of the illuminant.

that we did not force the CCT detection process to output a specific value, nor was any other step altered in any way. However, while improving the CCT detection could additionally aid our technique, we note that this would not be to such an extent as for the outdoor uplifting presented in Table 2. This is because the CCT estimates are already quite accurate for indoor settings, as opposed to outdoor scenes, which are prone to significant deviations. As our CCT detection process relies on a roughly even distribution of RGB values of pixels to estimate the present colour tint, we attribute these failures mainly to the outdoor environment maps not satisfying this requirement (e.g., by containing only a blue sky region and a green grass field).

Similarly to our evaluation of the outdoor uplifting, while we observe some significant improvements in the maximum error (e.g., decreasing from  $\Delta E = 41$  to  $\Delta E = 4$  for specific renders with the incandescent light source), we do not focus on the absolute measurements but rather on the uplifted spectral shapes. We present an example for each of the illumination types in Figure 7, where it can be observed that our method follows the ground truth spectral shape rather closely, while the scaled reflectance uplifting significantly differs.

Although the proposed tests are the most reliable measure for colour accuracy, we remind that they are still performed in an isolated environment. Therefore, while we claim that our technique definitely outperforms the current state of the art, we additionally conclude this section with a couple of examples of the uplifts applied to an actual rendered scene. This is simply for visualisation purposes, that is, to illustrate how the techniques perform in practice when incorporated into the whole path-tracing pipeline. We present the final renders in Figure 8.

### 4.3. Performance

Lastly, we summarise the performance of our proposed method in terms of both the execution time and memory usage. All the tests in this section were executed on an Intel Core i7-11800H 2.3GHz (8 cores, 16 threads) processor and 32GB DDR4 3200MHz RAM.

#### 4.3.1. Execution time

To evaluate the execution time, we use our standalone implementation. This is the preferred method of testing, as it eliminates any potential disruptions caused by other processes. Therefore, even if our technique were to be fully integrated within a state-of-the-art spectral renderer, we would still refer to the standalone implementation for accurate performance measurements.

Similarly to our colour accuracy tests described in Subsection 4.1, we use a dataset of 166 HDR environment maps of the same resolution that cover a wide variety of distinct settings and illumination conditions. For each of these maps, we perform the following: their loading; the initialisation of the uplifting system for the given map (including all the steps of the pipeline, that is, sky detection, CCT detection, etc.); and finally the per-pixel uplifting. The execution time of each step is recorded. In order to compare the performance of our technique, we additionally run the same test on the scaled reflectance uplifting method that is supported by our system. The

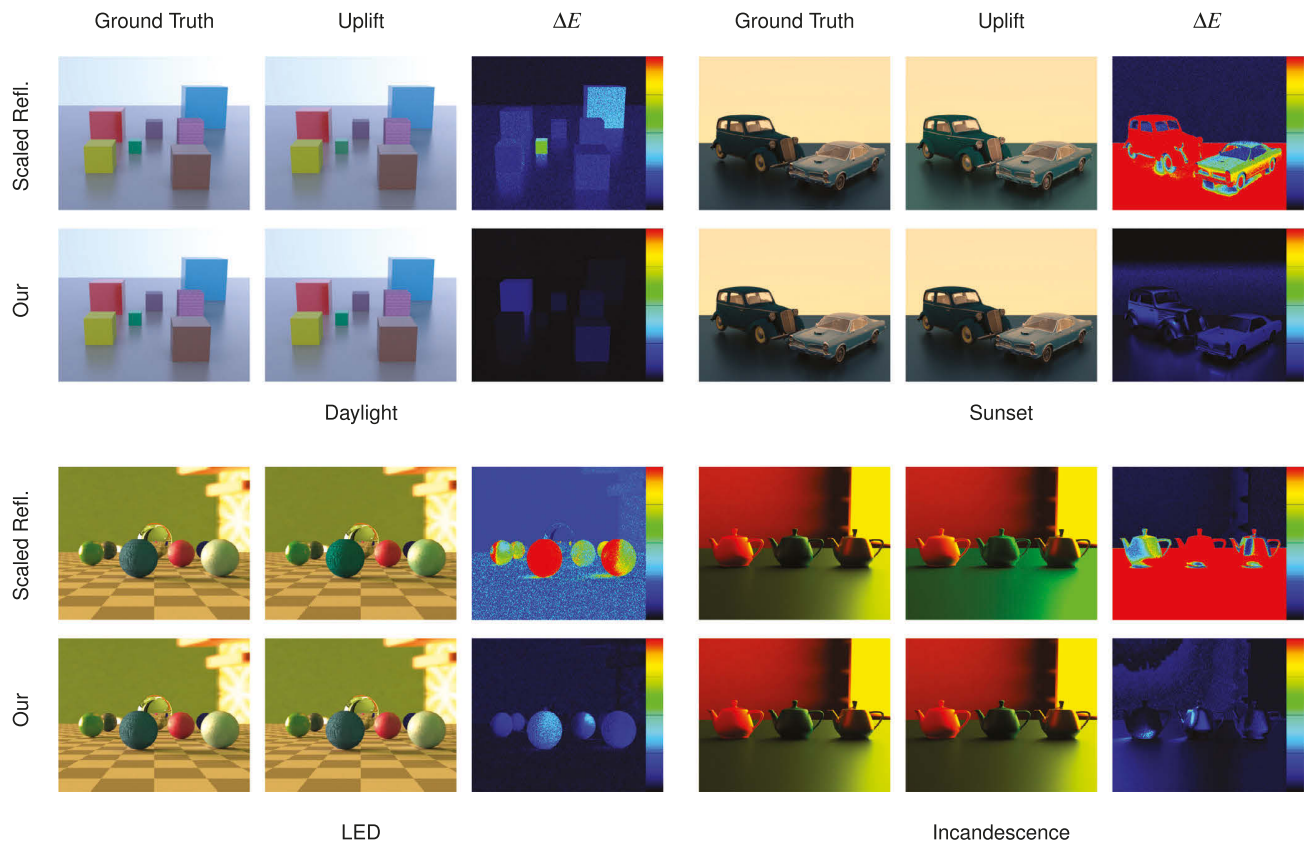


**Figure 8:** Examples of both our technique and the state-of-the-art (or the scaled reflectance) uplifting when used for image-based lighting in the Mitsuba 3 renderer. Both techniques are compared to the ground truth in terms of the CIE Delta E 2000 error. All error images are relative to  $\Delta E = 5$ . All used environment maps are from our own rendered datasets created for the colour accuracy tests in Subsection 4.2. Note that 4 of the 5 available uplifting categories are present, with the Fluorescent uplifting visualised in Figure 1.

**Table 4:** Average execution time of the individual steps of the uplifting pipeline, both for our and the current state of the art (i.e., the scaled reflectance) technique.

Step	Scaled refl. (s)	Our (s)
Image loading	0.1	0.1
Sky detection	N/A	2.8
Clustering	N/A	3.0 [1-13]
Per cluster (up to 6x):		
CCT Detection	N/A	0.001 (x6)
Cube initialization	0.85	0.85 (x6)
Per-pixel Uplifting	174	540

Note: The clustering process is the only one with variable execution time, with range specified in brackets.

method is identical to the one used for testing in Subsections 4.1 and 4.2.

We present our result summary in Table 4. We specifically divide the individual steps into *initialisation* of the uplifting system (which includes image loading, sky detection, clustering, and both the CCT

detection and cube initialisation) and the actual *uplifting* of the input environment map.

We first address the *initialisation* process. As our technique contains a multi-step pipeline in contrast to only a single cube loading of the current state of the art, it is clear that its execution time is worse. Specifically, on average, our initialisation takes 5.45 s as opposed to 0.95 s of the scaled reflectance technique. While the best-case scenario only worsens the current state of the art by a factor of 3, worst-case initialisation cases take up to 16 s.

However, although the initialisation time is significantly worse for our technique, we do not see this as a fundamental problem. In terms of the whole rendering pipeline, this process needs to only be executed once, and we find the performance overhead to be more than acceptable for the improved colour accuracy. Nevertheless, we see possible future work both for the sky detection and the clustering process, the performance of which was not specifically addressed during our research. The clustering process especially is heavily penalised by suboptimal heuristics.

The more worrisome results are for the actual *per-pixel uplifting*. On average, our current implementation takes 3 times longer

than the scaled reflectance technique. While some of this can be attributed to the out-of-gamut values and the overhead caused by multiple clusters, the majority of the performance penalty is caused by the lookup in the new illuminant-based uplift models. While in the D65 cube, a constant lookup is sufficient to find the correct voxel, the new models are scaled and skewed and a lookup within them can also require checking of neighbouring voxels (see Section 3.2). On average, our current implementation requires 6 lookups for each RGB value.

While the goal of this paper was to propose a proof of concept as opposed to a fully functional method, we still see this as a drawback of our technique. In the future, we propose focusing on improving this aspect by optimising the data structures. We specifically suggest researching the idea of creating new cubes by interpolating data from the skewed models.

#### 4.3.2. Memory usage

In terms of memory requirements, the main difference between our technique and the current state of the art lies in the number of stored uplift models. While the scaled reflectance uplifting method stores only one cube of size  $32^3$ , our new system allows for a maximum of 6 models (i.e., one for each recognised cluster). Additionally, the cube uplift structure does not require the storage of RGB values of individual lattice points, as they can be computed from the voxels' indices. However, this is not an option for our skewed models, which therefore additionally store 3 floating point values for every point.

This specifically means increasing the memory requirements from 0.4MB to a maximum of 4.8MB in the worst-case scenario. While our method also uses some additional data structures - such as an array of pointers for pixels to their respective clusters, or the clusters' CCT and illumination type information, we do not consider them of significance for two reasons: first, a lot of this data can be stored in optimised structures in the future; and second, even the current state of the art stores additional information as opposed to only the 3 sigmoid coefficients.

Overall, while our method has higher memory requirements than the scaled reflectance technique, we do not find this to be a limiting factor when used in a spectral renderer. With all the other data that needs to be loaded prior to path tracing, we consider the memory overhead negligible.

## 5. Conclusion

We presented the first method capable of uplifting HDR environment maps based on real-world emission data. Instead of creating synthetic spectra, we rely on estimating the real-world properties of light sources present at environment map capture, which we then use to constrain the uplifting process. The realistic data provided by our method aids in the prevention of colour deviations when using image-based lighting in a spectral renderer. This is important, especially in cases where even slight colour artefacts between the render and its real-life counterpart matter, such as in the VFX industry.

The results of our method are satisfactory in terms of the round-trip error and show a noteworthy improvement of the current state of

the art. This is especially pronounced in the case of indoor lighting conditions, where the current techniques exhibit significant drawbacks.

However, we recognise some remaining deficiencies in certain parts of our proposed uplifting pipeline. Specifically, as the precision of these steps was not the main focus of this work (which is to illustrate that such a pipeline can be made to work in the first place), both the process of clustering and CCT detection still generate insufficiently accurate results for certain inputs. As future work, we propose utilising more robust approaches to increase the precision of these aspects of our method. Additionally, we intend to focus on the data structures that are used to store our new uplift models, as their optimisation could significantly improve the performance of the method. Specifically, we suggest creating cubes by interpolating the data already stored in our models.

As a byproduct of our work, we also presented a novel approach to camera calibration for the purposes of environment map capture that uses both a colour target and a light source. In addition to it aiding our uplifting process, we believe it to be a useful tool in the area of spectral asset creation, since calibrating with only a colour target does not retain sufficient information about the light source colour temperature in the captured scene. An additional benefit of this approach is that it is more cost-effective and practical in comparison to existing emissive calibration targets.

## Acknowledgements

We acknowledge funding by the Grantová Agentura České Republiky with grant number GAČR-22-22875S, the Horizon 2020 Framework Programme of the European Union (grant number 956585, the PRIME ITN), and by Charles University under internal grant SVV-260699. The proposed environment map captures presented in this work were made by Roman Frátrik as a part of a student project at Charles University. We additionally thank Petr Vévoda for his help with the Prague Sky Model.

## Conflicts of Interest

None of the authors have conflict of interest that would affect their objectivity in conducting the presented research.

## References

- [BBG23] BELCOUR L., BARLA P., GUENNEBAUD G.: One-to-many spectral upsampling of reflectances and transmittances. *Computer Graphics Forum* 42, 3 (2023), e14886.
- [CZ11] CHAKRABARTI A., ZICKLER T.: Statistics of real-world hyperspectral images. In *Proceedings of IEEE Conference on Computer Vision and Pattern Recognition (CVPR)* (Los Alamitos, CA, USA, 2011), IEEE, pp. 193–200.
- [Eng] Engineering Image: camSPECS. <https://www.image-engineering.de/products/equipment/measurement-devices/588-camspecks-express>. Accessed: 2024-12-11.
- [Fai20] FAIRCHILD M. D.: Von kries 2020: Evolution of degree of chromatic adaptation. In *Color and Imaging Conference*

- (Bellingham, WA, 2020), vol. 28, Society for Imaging Science and Technology, pp. 252–257.
- [FHL\*18] FASCIONE L., HANIKA J., LEONE M., DROSKE M., SCHWARZHaupt J., DAVIDOVIČ T., WEIDLICH A., MENG J.: Manuka: A batch-shading architecture for spectral path tracing in movie production. *ACM Transactions on Graphics (TOG)* 37, 3 (2018), 1–18.
- [IOZ\*18] IMAMOGLU N., OISHI Y., ZHANG X., DING G., FANG Y., KOUYAMA T., NAKAMURA R.: Hyperspectral image dataset for benchmarking on salient object detection. In *2018 Tenth International Conference on Quality of Multimedia Experience (QoMEX)* (Piscataway, NJ, 2018), IEEE, pp. 1–3.
- [JH19] JAKOB W., HANIKA J.: A low-dimensional function space for efficient spectral upsampling. In *Computer Graphics Forum* (2019), vol. 38, Wiley Online Library, pp. 147–155.
- [JMW\*64] JUDD D. B., MACADAM D. L., WYSZECKI G., BUDDE H., CONDIT H., HENDERSON S., SIMONDS J.: Spectral distribution of typical daylight as a function of correlated color temperature. *Journal of the Optical Society of America* 54, 8 (1964), 1031–1040.
- [JSR\*22] JAKOB W., SPEIERER S., ROUSSEL N., NIMIER-DAVID M., VICINI D., ZELTNER T., NICOLET B., CRESPO M., LEROY V., ZHANG Z.: Mitsuba 3 renderer, 2022. <https://mitsuba-renderer.org>.
- [JWH\*19] JUNG A., WILKIE A., HANIKA J., JAKOB W., DACHSBACHER C.: Wide gamut spectral upsampling with fluorescence. *Computer Graphics Forum* 38, 4 (2019), 87–96.
- [KJKN\*14] KIDER JR J. T., KNOWLTON D., NEWLIN J., LI Y. K., GREENBERG D. P.: A framework for the experimental comparison of solar and skydome illumination. *ACM Transactions on Graphics (TOG)* 33, 6 (2014), 1–12.
- [KPB\*18] KOKKA A., POIKONEN T., BLATTNER P., JOST S., FERRERO A., PULLI T., NGO M., THORSETH A., GERLOFF T., DEKKER P., et al.: Development of white led illuminants for colorimetry and recommendation of white led reference spectrum for photometry. *Metrologia* 55, 4 (2018), 526.
- [Kur84] KURUCZ R. L.: Solar flux atlas from 296 to 1300 nm. *National Solar Observatory Atlas 1* (1984).
- [LF20] LANGLANDS A., FASCIONE L.: Physlight: An end-to-end pipeline for scene-referred lighting. In *Special Interest Group on Computer Graphics and Interactive Techniques Conference Talks* (New York, NY, 2020), Association for Computing Machinery, pp. 1–2.
- [Mac35] MACADAM D. L.: The theory of the maximum visual efficiency of colored materials. *Journal of the Optical Society of America* 25, 8 (1935), 249–252.
- [McC92] MCCAMY C. S.: Correlated color temperature as an explicit function of chromaticity coordinates. *Color Research & Application* 17, 2 (1992), 142–144.
- [MLNS24] MORIMOTO T., LINHARES J. M., NASCIMENTO S. M., SMITHSON H. E.: How many surfaces can you distinguish by color? Real environmental lighting increases discriminability of surface colors. *Optics Express* 32, 20 (2024), 34246–34253.
- [MMD\*76] MCCAMY C. S., MARCUS H., DAVIDSON J. G., et al.: A color-rendition chart. *Journal of Applied Photographic Engineering* 2, 3 (1976), 95–99.
- [MSHD15] MENG J., SIMON F., HANIKA J., DACHSBACHER C.: Physically meaningful rendering using tristimulus colours. *Computer Graphics Forum* 34, 4 (2015), 31–40.
- [MT11] MOKRZYCKI W., TATOL M.: Colour difference $\Delta$  EA survey. *Mach. Graph. Vis* 20, 4 (2011), 383–411.
- [OYH18] OTSU H., YAMAMOTO M., HACHISUKA T.: Reproducing spectral reflectances from tristimulus colours. *Computer Graphics Forum* 37, 6 (2018), 370–381.
- [PHG19] PILLAY R., HARDEBERG J. Y., GEORGE S.: Hyperspectral imaging of art: Acquisition and calibration workflows. *Journal of the American Institute for Conservation* 58, 1-2 (2019), 3–15.
- [Smi99] SMITS B.: An rgb-to-spectrum conversion for reflectances. *Journal of Graphics Tools* 4, 4 (1999), 11–22.
- [SW13] SHEN Y., WANG Q.: Sky region detection in a single image for autonomous ground robot navigation. *International Journal of Advanced Robotic Systems* 10, 10 (2013), 362.
- [TW24] TÓDOVÁ L., WILKIE A.: Constrained spectral uplifting for HDR environment maps. In *Eurographics Symposium on Rendering*, E. Haines and E. Garces (Eds.) The Eurographics Association (2024). <https://doi.org/10.2312/sr.20241153>
- [TWF21] TÓDOVÁ L., WILKIE A., FASCIONE L.: Moment-based constrained spectral uplifting. In *Eurographics Symposium on Rendering (EGSR) (DL)* (Göttingen, Germany, 2021), Eurographics Association, pp. 215–224.
- [TWF22] TÓDOVÁ L., WILKIE A., FASCIONE L.: Wide gamut moment-based constrained spectral uplifting. *Computer Graphics Forum* 41, 6 (2022), 258–272.
- [VBRKW22] VÉVODA P., BASHFORD-ROGERS T., KOLÁŘOVÁ M., WILKIE A.: A wide spectral range sky radiance model. *Computer Graphics Forum* 41, 7 (2022), 291–298.
- [VDRE23] VAN DE RUIT M., EISEMANN E.: Metameric: Spectral uplifting via controllable color constraints. In *ACM SIGGRAPH 2023 Conference Proceedings* (New York, NY, 2023), Association for Computing Machinery, pp. 1–10.
- [Wil18] WILKIE A.: The Advanced Rendering Toolkit, 2018. <http://cg.mff.cuni.cz/ART>.
- [WVBR\*21] WILKIE A., VÉVODA P., BASHFORD-ROGERS T., HOŠEK L., ISER T., KOLÁŘOVÁ M., RITTIG T., KRIVÁNEK J.: A fitted radiance and attenuation model for realistic atmospheres. *ACM Transactions on Graphics (TOG)* 40, 4 (2021), 1–14.

# 4 Spectral Emission Estimation of Light Sources

In the previous chapter, we introduced a technique for uplifting HDR environment maps. It achieves physical accuracy by relying on real-life emission measurements, which are stored in the form of a database. While the approach provides satisfactory results for a multitude of different light sources, it is, similarly to all database-driven methods, inherently limited to the shapes of the predefined spectra. In addition to not encompassing all possible types of illumination, these spectra are obtained from generally available resources, such as the database of standard illuminants by CIE (CIE Technical Report, 2004) – as these are also the resources that are typically used for other uplifting and spectral rendering workflows. However, the provided illuminants are not fully reflective of real-world behavior. Their spectra are obtained in ideal conditions, with smoothing performed to minimize measurement errors. In contrast, the SPDs of lamps in practical settings typically degrade over time, both due to aging and other environmental factors. As a result, color discrepancies may arise when comparing the final uplifts to their real-life counterparts.

These limitations motivate the idea of creating a method that would be capable of identifying the spectral power distribution of virtually any light source from only an RGB capture of a scene that it illuminates. Although this would also improve our technique for HDR environment maps, the potential application areas extend far beyond the scope of this work. For instance, when creating digital counterparts of a scene’s main light sources in the VFX industry, we see a possibility of it eliminating the need for both manual measurements and spectral uplifting — or even assist in product manufacturing, by predicting object appearance under various lighting conditions.

The proposed technique requires only a high quality RAW photograph of the desired scene with a color target, such as the Macbeth Color Checker, properly placed within the frame. As these are also the requirements of the color calibration process, we do not find them overly restrictive to the user. The method then analyzes the differences between the captured RGB values of the target’s patches and their default properties, and this information is used as an input to an optimization algorithm to infer the most likely emission spectrum.

While the current paper provides a proof of concept as opposed to a production-ready version of the technique, it presents a novel approach that has not been explored before, with a multitude of possibilities for further extension. An included evaluation for a specific color target (the Macbeth Color Checker) additionally demonstrates satisfactory results for our testing data, which enhances the practical relevance of the work.

We once again note that the method is technically not a spectral uplifting method. However, due to its broad range of applications and its potential to replace uplifting in certain contexts, we consider it highly relevant to this research.

The following document is a draft of our manuscript that is being prepared for resubmission. It has already undergone a peer review cycle after being rejected from the Eurographics Symposium on Rendering 2025, and the current version incorporates a number of the reviewers' comments and suggestions.

However, as the reviews were received at a late stage nearing the thesis deadline, not all feedback could be fully addressed. We additionally plan to include a more comprehensive evaluation and possibly even extend the method further, given the encouraging preliminary findings and initial feedback.

# Estimating the Spectral Power Distribution of Light Sources via Color Target Captures

Lucia Tólová, Alexander Wilkie

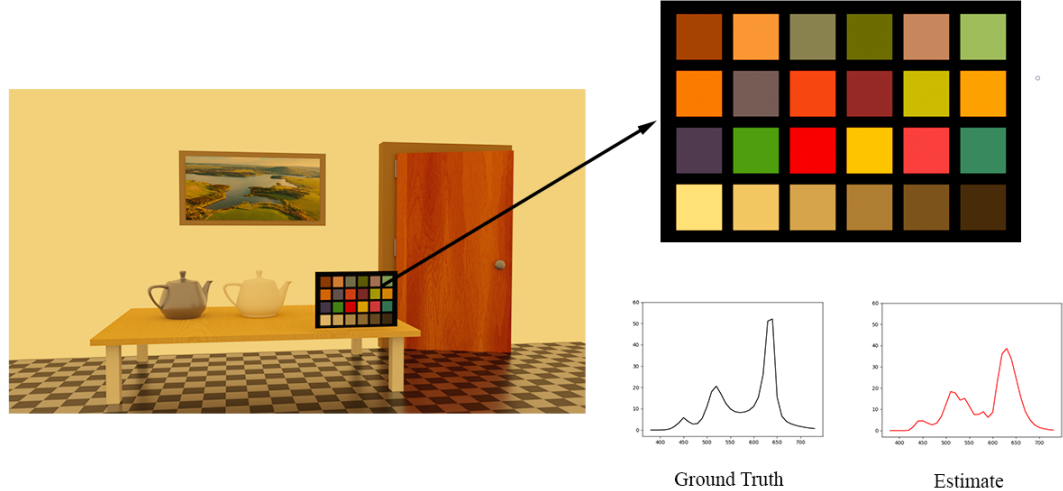


**Figure 1** Spectral emission curve of the light source present in the scene, estimated from the RGB values of the patches of the Macbeth Color Checker. Note that since the color target is required to be placed close to the light source with minimal influence of the surroundings, the image of the full scene (left) serves only for visualization purposes and the final estimation is made from a closeup that is directly illuminated by the light source (top right).

## Abstract

Physical accuracy of a spectral renderer relies on accurate definition of spectral assets. However, real-life spectral data can only be obtained by performing manual measurements, which is tedious, time and resource-intensive, and oftentimes even impossible. While there is a possibility to convert captured RGB variants into the spectral domain (called spectral uplifting), the results do not have to correspond to real-life counterparts, which, in turn, may cause metameristic artifacts. These are especially prevalent in the case of light source uplifting due to the complex and spiky nature of emission spectra.

In this paper, we propose a method that estimates the emission spectrum of a light source that illuminated a scene captured by a camera. In contrast to manual measurements, our technique is lightweight and fast and relies on only the presence of a standard color target, such as the Macbeth Color Checker generally used for color calibration. In addition to our technique aiding spectral rendering workflows in the VFX industry, we propose a way in which it could be utilized for preventing metameristic artifacts when matching materials in e.g., interior design or product manufacturing industry.

## 1 Introduction

One of the key goals in designing a renderer is to simulate real-world behavior. This is especially important for applications where even slight differences between its results and real-life appearance might be noticeable, such as when matching plate footage with digital doubles in visual effects (VFX) or in product design, including industries like furniture or clothing manufacturing. Spectral renderers attempt to achieve this by representing material properties as they are in nature, which is a wavelength distribution. As opposed to the more traditionally used RGB tristimulus representation, their simulation of light transport is physically based, which results in an appearance much closer to its real-world counterparts.

However, obtaining spectral assets and materials is a rather cumbersome task. Either they need to be manually measured, or a process called spectral uplifting

needs to be performed, which is a conversion of their RGB variants into the spectral representation. Both of these options present their own set of challenges. Measurements must be performed with special spectrometers in controlled environments, which is not only time-consuming and resource-intensive, but, in many cases, even impossible. Additionally, inaccuracies are likely to arise both due to imperfections of the devices and human error.

While spectral uplifting, on the other hand, produces accurate results in terms of the desired RGB value, it is prone to metameristic artifacts. As multiple spectra evaluate to the same RGB value (called metamerism), the process has no way of knowing which spectrum to uplift to. Making an arbitrary decision may result in deviations from the real-life counterpart and, therefore, a deviation in the final appearance. While this is generally not a major problem for reflectance data,

where the current techniques, such as the method proposed by Jakob and Hanika (2019), are able to produce smooth and simple spectral curves that typically resemble most of the standard cases, emission data is more complex and cannot be as easily generalized (Tódová; Wilkie, 2025). Therefore, so far, the current state of the art for uplifting emission is simply scaling reflectance data. This means scaling the input high dynamic range RGB value into the low dynamic range, utilizing a general reflectance uplifting technique (for example, the Mitsuba renderer uses the method by Jakob and Hanika (2019), while the Manuka renderer uses a modified version of the technique by Smits et al. (Fascione et al., 2018)), and then scaling the full spectrum back into HDR. However, while the resulting spectra are satisfactory in terms of the RGB value, their shapes do not match the more complex and spiky nature of real-life emission. This deviation is only accentuated by the fact that the influence of emission on the final appearance of the scene is much more prominent than that of reflectance data.

Unfortunately, addressing this problem during the uplifting process is a rather difficult task, as the input RGB data already loses all spectral information during its creation. However, when it comes to assets that contain more than just a single RGB value, we can resort to some reasonable conclusions. For instance, if the input is an RGB capture performed by a digital camera calibrated to record raw data (i.e. no white balance or color calibration is applied), its color tint may be a good indicator of the color temperature of the present illumination – e.g., images with yellowish tones are highly likely to have been captured under a warm illuminant. Additionally, these assumptions can be affirmed if the captured scene contains objects with known material properties. For example, if the scene were to, theoretically, contain an object with a diffuse 100% reflective material which attains yellow color in the final capture, the tint of the present illuminant can be estimated with a high degree of accuracy.

The goal of this work is to use this observation in order to estimate the spectral properties of light sources present in camera captures. As the objects with known material properties, we propose utilizing color targets (such as the Macbeth Color Checker (McCamy et al., 1976)), which are generally present during the capture process for the purpose of color calibration. Our technique is based on identifying the changes in the RGB values of individual patches of the color targets and using this information to approximate the spectral power distribution of the light source that illuminates them. Because of its lightweight nature, this technique offers the VFX pipeline the unique ability to obtain on-set emission spectra without the need for manual measurements. We also see other potential use cases in material matching in interior design. Consider the scenario when looking for a new material to complement a room. As the store lighting may differ from the one at home, the final appearance of materials when incorporated into the home design may differ from the expectations. Our technique could be used to determine the home illumination and to subsequently simulate the material’s appearance under such conditions, thus eliminating the need for time-consuming and often impractical trials – such as physically bringing samples from the store. We also see how the applications of our technique could, in the future, be extended to product manufacturing.

## 2 Previous Work

This section provides a summary of previous methods that have explored similar objectives and are related to this work.

The most closely related technique can be considered

the one proposed by Lee et al. (2000), which also aims at estimating the spectral emission of scene illumination from only a single input image. In contrast to our approach, it does not rely on a color target, but rather uses a gray world algorithm to identify the most achromatic region of the image and then uses principal component analysis (PCA) to determine its reflectance properties. The final emission is obtained based on this information from a previously established database. This inherently limits the spectral shapes the technique is capable of achieving.

Another method with an identical goal was proposed by Shi et al. (2014). Similarly to our approach, it is also based on a color target, but uses a Wiener estimation along with a smoothing factor to obtain the final spectrum. However, it is suspect to multiple limitations. First, it only assumes smooth emission, which is not representative of real-life illumination, such as fluorescent or LED light sources. Additionally, the evaluation of the method lacks diversity, and is only limited to the D50 and A illuminants. As a result, its practical applicability remains unclear.

A novel capture system that identifies both the illumination along with surface reflectance was introduced by Tominaga (1996). In contrast to previous work, which is aimed at standard camera captures, their approach designs a multichannel system that requires more complicated calibration. While the experimental evaluation on a small dataset provides satisfactory results, the complexity of the capture process is exactly what our work is trying to avoid.

Methods based on deep learning and neural networks have also been investigated. Han et al. (2022) propose a solution for emission estimation that uses a large training dataset, comprised of both real-life and generated captures. Their technique demonstrates consistent performance across a wide range of spectra. However, as with any data-driven method, its results are inherently limited by the quality and diversity of the training data, particularly in terms of the spectral shapes.

Deeb et al. (2018) similarly rely on deep learning, and use it to estimate both the emission and surface reflectance from self-interreflections occurring in the captured scene. While the system achieves satisfactory results, both its training and evaluation are only performed on simulated data, which questions practical applicability. Additionally, the technique is reliant on the presence of self-interreflections, which is not guaranteed in all scenarios.

In addition to estimating illumination of a scene, there also exist methods that focus solely on reflectance data. Although this can be seen as a complementary problem, the techniques remain relevant to our work – particularly if they rely on similar underlying principles.

One of such methods was introduced by L. Zhang et al. (2020), who propose reconstructing spectral reflectance of surfaces based on mixed weighting and local optimization. By using a combination of estimation methods, such as the Wiener method, they are capable of improving previous reconstruction attempts for experimental data.

Similarly to the problem of estimating emission, using an approach based on neural networks is also a viable option. However, generally, in order to provide sufficient results, this requires a training set of a substantial size – which typically then necessitates using simulated data due to the considerable difficulty of obtaining real-life captures and measurements of adequate quality and diversity.

Li et al. (2018) approach this problem with sample optimization. Instead of generating synthetic data, they base their method on real measurements and optimize the samples in order to provide a more efficient re-

construction. Experimental results show improvement over previous methods in terms of both spectral and colorimetric reconstruction errors.

Although the current version of our work does not take inspiration from any of the previously proposed methods, we note that a more thorough exploration of some of the techniques (particularly the ones by Shi et al. (2014) and L. Zhang et al. (2020) that take a different approach to optimization) is our immediate priority for future work in order to provide improvements, mainly in terms of practical applicability.

### 3 Method Requirements

In the following, we summarize the necessary set of pre-conditions and assumptions that we make in order for our technique to be applied in the manner as proposed.

**Camera Capture Settings.** A necessary requirement for a successful execution of our technique is that the settings of the used camera need to be set to capture raw data. While this also includes disabling post-processing filters such as noise reduction, sharpening, vignette correction, and automatic adjustments to contrast or image brightness, the main and the most crucial requirement is that the camera’s white balance settings remain unaltered and that all the other color correction options are turned off. This also extends to the process of color calibration with the color target, which must not be applied to the image prior to the execution of our technique. By configuring the camera in this manner, we ensure the capture of raw data, which is essential for a reliable performance of our technique.

**Color Target Placement.** Our technique relies on the even distribution of the emission of the light source across the whole color target. This requires careful positioning, so that the illuminant we wish to estimate influences all of its patches in an identical manner. The rest of the requirements are identical to those of the color calibration process (described in e.g., the color target manual issued by X-Rite (2009)), which include ensuring that the target is placed at a proper distance from the camera, is in focus, and is free from shadows and reflections. This is generally achieved by placing the target in a neutral area, where the influence of indirect illumination is minimized.

**Spectral Representation.** While in theory, a spectrum is a continuous distribution, the support of the spectral representation in a renderer requires its discretization. This is done by simply sampling the spectrum at a sufficiently high resolution in order to not lose color precision. In the case of emission and reflectance spectra in the visible range, this translates to sampling wavelengths between 380 nm to around 740 nm at intervals from 1 nm to 10 nm, depending on the desired level of accuracy. Generally, 10 nm intervals are deemed sufficient for simple reflectance data and smooth emission spectra (such as the daylight or incandescent illumination), however, more complex and spiky data (e.g., fluorescent illuminants or lasers) require denser sampling. For reference, the resources released with the ART renderer are sampled at 5 nm increment for the emission data and 10 nm increment for the reflectance data (Alexander Wilkie, 2018), while the Mitsuba renderer uses the 5 nm increment to sample both its standard daylight spectra and its color matching functions (Jakob; Speierer, et al., 2022).

As the goal of our work is to present a proof of concept as opposed to a complete solution incorporated in the rendering pipeline, we opted for using the 10 nm increment and 36 samples. Another reason for this decision is our choice of the color target (discussed in section 4). We note that this choice both slightly limits the visible range (which, in some works, goes up to 780 nm) and results in a decrease of color accuracy. However, for

our purposes, we find the trade-off acceptable given the simple and lightweight nature of the solution. This is further supported by the fact that even in production pipelines, similar trade-offs are often made, especially in cases where storing and loading of densely sampled spectra would result in significant performance and memory overhead.

**Color Target.** Similar to its positioning, the requirements we place on the individual patches of the color target closely align with those of the color calibration process. Specifically, the patches must be highly diffuse to accurately reflect the effect of the illuminant. Additionally, their colors should vary in hue, saturation, and brightness, to ensure that a wide color gamut is covered. All standard color targets already meet these conditions, and as the goal of our work is for the solution to be as lightweight and user-friendly as possible, we propose utilizing an existing target that is already generally present during camera capture (as opposed to designing a new one). However, we place one additional requirement on the color target, and that is on the number of its patches. Specifically, we require that the number of samples  $s$  of the estimated spectrum is at most 3 times greater than the number of patches whose reflectance curves are linearly independent,  $p$ , i.e.:

$$s \leq 3 * p \quad (1)$$

This specific requirement is caused by the nature of the solution (see later in section 4, specifically subsection 4.1).

### 4 Light Source Estimation

Our technique relies on a sole input in terms of an RGB camera capture with a color target that satisfies all of the requirements posed in section 3. The output is then a single emission spectrum sampled at a pre-defined rate, which is the approximation of the light source that illuminated the color target.

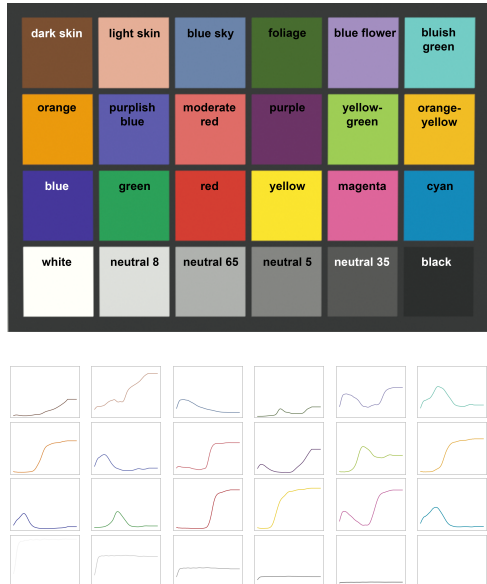


**Figure 2** The Macbeth Color Checker visualized under the illuminant D65, with the reflectance curves of individual patches (taken from the spectral dataset distributed with the ART renderer (Alexander Wilkie, 2018)) shown underneath.

We specifically show the implementation of our technique and its subsequent performance for the sampling

rate of 36 samples with 10 nm increments (starting at 380 nm). Our choice of the color target is the Macbeth Color Checker, which contains 24 color patches. At least 12 of their respective reflectances are linearly independent (see Figure 2), which satisfies Equation 1. We provide the specific details of our technique in two steps. First, we present the formulation of our approach to the problem. This is almost identical regardless of the choice of the color target and the sampling rate, with only minor changes in e.g., matrix and vector sizes. Second, we present our specific implementation for our choice of the Macbeth Color Checker and the sampling rate of 36 samples and 10 nm increment.

#### 4.1 Problem Formulation

To compute the RGB value from an input spectral power distribution (SPD), the general approach involves first determining the XYZ color coordinates, followed by a conversion to the RGB color space. While the conversion from XYZ to RGB is performed by a simple  $3 \times 3$  matrix multiplication, obtaining the XYZ coordinates from an input SPD follows:

$$\begin{aligned} X &= \int_{\lambda} S(\lambda) \bar{x}(\lambda) d\lambda \\ Y &= \int_{\lambda} S(\lambda) \bar{y}(\lambda) d\lambda \\ Z &= \int_{\lambda} S(\lambda) \bar{z}(\lambda) d\lambda \end{aligned}$$

where  $S(\lambda)$  is the input SPD and  $\bar{x}$ ,  $\bar{y}$  and  $\bar{z}$  are the color matching functions corresponding to the CIE XYZ color space.

In a spectral renderer, i.e. in a discretized space, finding a solution to the integrals translates to their approximation by sampling the color matching functions and the SPD at the same intervals and expressing the solution as a sum. In our specific case (i.e. using 36 samples at 10 nm intervals), this corresponds to solving the following equations:

$$\begin{aligned} X &= \sum_{i=0}^{36} S[i] * \bar{x}[i] * 10 \\ Y &= \sum_{i=0}^{36} S[i] * \bar{y}[i] * 10 \\ Z &= \sum_{i=0}^{36} S[i] * \bar{z}[i] * 10 \end{aligned}$$

where the functions  $S$  and  $\bar{x}$ ,  $\bar{y}$  and  $\bar{z}$  are already sampled at 10 nm intervals, with the first sample starting at 380 nm.

Since standard screens and monitors can only display tristimulus data, in a spectral rendering pipeline, it is essential to perform the conversion of the final spectral result of the light transport into a tristimulus space. In principle, this is also what happens during camera capture, where the results of the light transport occurring in nature are converted into tristimulus values through the camera's sensors.

The same concept is also applicable to our case of the color target positioned in the captured scene. The final XYZ values of its patches are also a result of the conversion of their respective SPDs that are, again, a result of the scene's light transport interactions. We resort to a simplification of the previous statement, and that is that the final SPD of a patch is only a result of

the interaction of the reflectance of the patch with the present illumination, i.e.:

$$S(\lambda) = R(\lambda) * E(\lambda)$$

where  $S(\lambda)$  is the final SPD of the patch,  $R(\lambda)$  is the reflectance of the patch and  $E(\lambda)$  is the present illuminant.

This assumption is reasonable due to the requirements placed on the color target (see section 3) both in terms of the material properties of its patches (i.e. high diffusion) and its positioning (i.e. placed in a neutral area to minimize the influence of other objects). A similar approach is commonly employed in the color calibration process.

Therefore, the final X value of every patch can be expressed as follows:

$$X = \sum_{i=0}^{36} R[i] * E[i] * \bar{x}[i] * 10$$

with the same applying to the Y and Z components and their respective color matching functions.

Since the XYZ values of the patches can be obtained by a simple conversion from their RGB values in the input capture, and since both the color matching functions and the reflectance curves of the individual patches are known (specifically, we use the measurements obtained from the resources of the ART renderer (Alexander Wilkie, 2018)), the only unknown variables left in the equation are the 36 samples of the illuminant  $E[i]$ .

As we can express the XYZ values of every patch in this manner, and as the Macbeth Color Checker contains at least 12 patches with linearly independent reflectances (as per Equation 1), this, in theory, leaves us with a linear system of 36 unknown coefficients and at least 36 equations, which should be easily solvable with a simple Gaussian elimination process. However, in practice, the equality in the equations is extremely unlikely to hold, and the reason for that is noise. Whether it is due to the imperfections of the camera sensors or the influence of other objects in the captured scene (or even the patches themselves, which are not 100% diffuse), the final captured XYZ values will never be exactly the same as the results of the calculations. This redefines our problem as an *approximation* problem.

To be specific, our problem can be formulated as:

$$\min_{x \geq 0} (\|Ax - b\|)$$

where  $x$  is the discretized emission curve of the light source we are trying to find,  $b$  is a vector of size  $72 \times 1$  containing X, Y and Z values of all patches respectively and  $A$  is a matrix of size  $72 \times 36$  whose elements follow  $A[i][j] = R_{idx}[j] * \bar{c}[j] * 10$  with  $idx$  expressed as  $idx = \lfloor \frac{i}{3} \rfloor$  (with  $R_i$  being the  $i$ th patch of the color checker and  $\bar{c}$  being the color matching function for the respective color component, i.e.  $\lfloor \frac{i}{3} \rfloor = 0$  translates to using  $\bar{x}$ , etc.).

While this justifies the necessary precondition set on the number of linearly independent patches (see Equation 1), it does not mean that using 12 distinct patches (in the case of 36 samples) is going to be sufficient for accurately determining the result. Optimization problems of this nature benefit from a higher number of input data to reduce bias, and while overfitting can be a concern, this is generally the case of using a way larger input than the 24 patches we have available.

Additionally, we note the shapes of the reflectance curves of the individual patches, which can further decrease their informative value – either by being linearly dependent (or even extremely similar in terms of spectral shape) on one another, or by attaining zero values at certain wavelengths and thus not providing

any information for the respective coefficients. We provide the visualization of individual reflectances of the Macbeth Color Checker in Figure 2. This shows quite clear shape similarity of the neutral patches in the bottom row and, upon closer look, even some other pairs (e.g., the Green and Foliage patches, Blue and Purplish Blue patches and Orange Yellow and Yellow patches). Patches that are not reflective for specific wavelength ranges are also present (e.g., the Red, Yellow or the Blue patch).

Therefore, while the information obtained from the input is not necessarily insufficient to estimate the result, we note that the capabilities of the Macbeth Color Checker may not provide the level of accuracy that could be achieved with a more diverse color target.

## 4.2 Solution Approximation

We treat the problem as a non-linear least squares problem due to the added constraint on the non-negativity of the solution, which therefore follows:

$$\min_{x \geq 0} (\|Ax - b\|^2)$$

To solve the problem, we utilize the CVXPY library (Diamond; Boyd, 2016). We specifically choose the CLARABEL solver (Goulart; Chen, 2024), both due to its suitability for problems of similar nature, but also because of its demonstrated effectiveness in our test cases in comparison to other solvers.

However, while it manages to successfully minimize the objective, the results in terms of the final spectral shapes are less than ideal. Specifically, it often resorts to spiky, unrealistic spectra, as it treats samples as individual components rather than one continuous spectral curve.

Therefore, to discourage extremely high and unrealistic coefficient values, we additionally introduce an L2 regularization term, which penalizes large variations between adjacent coefficients. The final optimization problem then follows:

$$\min_{x \geq 0} (\|Ax - b\|^2 + \lambda \|x\|_2^2)$$

where  $\lambda$  is a regularization parameter controlling the strength of the penalty.

In our implementation, we specifically choose the value of 10 for the regularization parameter. However, we note that this is a choice based purely on heuristics, by testing the method on a large number of curves and attempting to find the right balance between its performance on smooth, simple curves and its effectiveness with more complex, spiky spectra, such as those of fluorescent or even LED illuminants.

Additionally, we emphasize that we do not claim that either our choice of the solver nor the choice of the regularization parameter is optimal. Throughout our research, the primary focus was not on the specific implementation details, but rather on providing a proof of concept with a simple and lightweight solution. Additionally, we believe that a highly accurate solution incorporated into a production pipeline would require more advanced color targets, the use of which could, potentially, require additional changes to the optimization approach.

## 5 Method Evaluation

As the primary application of our technique is within the VFX production pipeline, the ideal way of testing it would be on a production set. First, the ground truth emission spectra would need to be obtained by performing manual measurements of the present light

sources with a spectrometer, then, our method would need to be executed, and finally, the resulting emission approximation could be compared to the ground truth. To assess the performance of our technique on a wide variety of illuminants, this process would need to be performed a substantial amount of times for various illumination settings, ranging from simple daylight spectra to complex fluorescent and even laser illuminants. Ideally, even the spectral measurements should be performed multiple times to minimize measurement errors.

While we still suggest this approach for future work, unfortunately, it requires a significant amount of resources that were not available during our research. However, we manage to compensate for this by devising alternative methods of evaluation which also allow us to assess the validity and robustness of the proposed method. Specifically, we design scenarios where the ground truth illuminant is known beforehand and does not need manual measurements. As a result, our evaluation is conducted in the following settings:

### Test 1 - Synthetic Data

In the first testing scenario, we obtain an extensive set of illuminants and for each of them, we simply *compute* the appearance of the patches of the Macbeth Color Checker (i.e. no captures or renders are performed). This is done by a simple multiplication of the illuminants and the respective reflectances and then performing the conversion of the obtained SPDs to RGB as explained at the beginning of subsection 4.1. Our technique is then executed for the new computed color checker, and the resulting emission is compared to the original illuminant.

### Test 2 - Renders

Similarly to the previous test, the second evaluation scenario is also based on an extensive set of known illuminants. However, as opposed to performing simple computations to obtain the appearance of the Macbeth Color Checker, we perform its *renders*. We specifically use the Mitsuba 3 renderer and we create a scene that contains only a sole illuminant (in the form of an environment map) and the spectral definition of the Macbeth Color Checker. In order to minimize the noise present in the final render, the input XYZ value of each patch is obtained by iterating through all of its pixels and averaging their values. The new color checker comprised of the final averaged XYZ values is then used as an input for our technique.

In contrast to *Test 1*, which is purely synthetic, we base this scenario on the idea that the discrepancies caused by performing camera captures can be simulated by the noise generated during rendering. We therefore find this setup to be the closest simulation of the precise on-set captures described in our ideal evaluation conditions.

### Test 3 - Lab Camera Captures

Lastly, our goal was to also evaluate our technique on a couple of real-life captures of the Macbeth Color Checker. Unfortunately, due to resource limitations, the evaluation was conducted on only four captures, each under a different illuminant, taken with an iPhone 6S in X-Rite's Judge QC Light Booth. We note that this evaluation setup is by far suboptimal. Firstly, it does not meet the requirements of our technique, as the capture device was not properly calibrated and does not provide all the raw information needed for a reliable estimate. Furthermore, the illuminants were measured without professional-grade equipment, which

Light Source Type	Database	Illum. Count	Max $\Delta E$		Avg $\Delta E$		
			Uplifting	Our	Uplifting	Our	Improvement
Daylight	CIE	4	0.273	0.936	0.062	0.114	<b>0.54×</b>
	Kider	20	0.307	0.967	0.067	0.101	<b>0.66×</b>
	Sky Model	1728	0.173	0.087	0.009	0.004	<b>2.25×</b>
LED	CIE	9	10.928	0.905	1.249	0.046	<b>27.15×</b>
	LSPDD	122	16.055	0.552	0.038	0.013	<b>2.92×</b>
	Kokka et al.	1494	0.080	0.007	0.006	0.000	<b>12.00×</b>
	Royer LED	1089	22.400	1.788	1.420	0.033	<b>43.03×</b>
	Royer OLED	5	18.674	0.730	1.682	0.034	<b>49.47×</b>
Fluorescent	CIE	27	23.404	1.816	1.642	0.060	<b>27.37×</b>
	LSPDD	33	4.464	0.502	0.241	0.018	<b>13.39×</b>
	Royer	73	22.082	1.695	1.564	0.061	<b>23.64×</b>
Incandescent	LSPDD	17	3.398	0.870	0.121	0.029	<b>4.17×</b>
	Royer	26	4.295	1.520	0.374	0.074	<b>5.05×</b>
HID	CIE	5	25.560	1.528	2.240	0.109	<b>20.55×</b>
	LSPDD	4	0.282	0.035	0.028	0.002	<b>14.00×</b>
	Royer	36	24.754	1.527	2.013	0.108	<b>18.64×</b>
Halogen	LSPDD	31	0.796	1.431	0.053	0.036	<b>1.47×</b>
Laser	Royer	9	3.055	0.735	0.348	0.112	<b>3.12×</b>

**Table 1** Results of *Test 1* shown for all light source categories and their respective datasets. Note that due to the low luminosity of the *Royer* and *LSPDD* datasets, their emission spectra are scaled in order for the errors to be visible. However, we emphasize the *relative* differences between the techniques (also shown in the last column labeled *Improvement*), as the absolute values are directly proportional to the luminosity of the illuminants. Also note that values lower than 0.0005 are rounded and shown as 0.

may further undermine the credibility of the results. As such, we present them primarily as a preliminary indication of our technique’s performance in practice. However, we also note that such an imperfect setup has the advantage of testing the robustness of our method against much noisier and lower-quality data.

While all three testing scenarios differ in the way they obtain the final estimated emission, the method for comparing the results to the ground truth remains identical for all of them. Specifically, we use the approach for emission spectra comparison also used by Tódová and Wilkie (2025), which involves utilizing a large set of reflectance spectra and computing their appearance in terms of RGB value under both the ground truth and under the estimate (as described at the beginning of section 4.1). The average color error between the two RGB values then indicates the difference between the two illuminants.

In our case, we specifically use a dataset of 3656 reflectance data comprised of the following measurements: 1853 samples from the Pantone Color Matching System, 1598 samples from the Munsell Book of Color and 205 samples from the RAL Classic collection. As the color error, we use the CIE Delta E 2000 color error.

Additional dataset needed to perform the proposed evaluation scenarios is a large and varied set of known emission spectra for both *Test 1* and *Test 2*. A good example of this would be the CIE Standard Illuminants dataset (015:2018, 2018). However, while its spectra are based on real-life measurements, a lot of them are synthetic and smoothed out to create a representative approximation for a whole light source category. As we also wish to evaluate our technique for practical use, we require a dataset with measurements obtained also from real-life objects. To additionally account for measurement inaccuracies, which can differ in distinct settings, we opt for using multiple datasets obtained by different parties. Specifically, we use the following sets of illuminants: the CIE Standard Illuminants (015:2018, 2018); the LSPDD dataset (ROBY; AUBÉ, 2019); the database of real light sources by Royer (2020); the

dataset of LED measurements by Kokka et al. (2018); the Prague Sky Model (by Wilkie, Vevoda, et al. (2021) and the subsequent implementation by Vévoda et al. (2022)); and the sky measurements by Kider Jr et al. (2014). While not every dataset contains measurements from every light source category, we find the data they provide sufficient enough to cover a vast majority of existing illuminants.

To better distinguish between individual measurements, we categorize them according to their light source type. Each category is then evaluated separately, in order to show how our technique performs for distinct spectral shapes. We provide an overview of the individual categories along with their measurements from respective color atlases in Table 1. We note that for some categories, not all measurements are used for *Test 2*, mainly because of limited computational resources. However, in those cases, the illuminants used in the test are evenly sampled across the category according to their correlated color temperature, which results in a sufficiently representative set.

In order to show the performance of our technique in comparison to the current state of the art, we also execute all the tests for the *scaled reflectance uplifting*. Specifically, we use a variant of the method used in the Mitsuba 3 renderer, which uses a pre-computed RGB model that stores mappings from RGB values to reflectance spectra. Uplifting of an arbitrary HDR RGB value is then performed by scaling the value into the range of the model, performing a lookup in the model and, if needed, an interpolation of the closest mappings. The result is then scaled back into HDR, yielding an emission spectrum. As the reflectance spectra in the model need to be stored with respect to an illuminant, we specifically use the D65 daylight illumination. However, we do not concern ourselves with the specifics of the implementation, as we expect the scaling of any other type of smooth reflectance spectra to perform similarly.

In case of *Test 1*, the uplifting method is applied directly to the RGB value the input emission evaluates to. However, as the light source is not always present in

Light Source Type	Database	Illum. Count	Max $\Delta E$		Avg $\Delta E$		
			Uplifting	Our	Uplifting	Our	Improvement
Daylight	CIE	4	2.872	1.148	1.795	0.366	<b>4.90×</b>
	Kider	20	2.238	1.139	1.072	0.309	<b>3.47×</b>
	Sky Model	36	5.350	3.813	0.328	0.197	<b>1.66×</b>
LED	CIE	9	11.300	0.909	1.689	0.193	<b>8.75×</b>
	LSPDD	118	1.802	0.151	0.044	0.006	<b>7.33×</b>
	Kokka et al.	116	0.913	0.505	0.041	0.030	<b>1.37×</b>
	Royer LED	124	6.200	8.359	0.389	0.481	<b>0.81×</b>
	Royer OLED	5	1.958	0.190	0.308	0.043	<b>7.16×</b>
Fluorescent	CIE	27	15.587	22.057	3.262	3.041	<b>1.07×</b>
	LSPDD	33	0.218	0.197	0.022	0.019	<b>1.16×</b>
	Royer	73	2.118	2.170	0.261	0.208	<b>1.25×</b>
Incandescent	LSPDD	17	0.163	0.016	0.017	0.002	<b>8.50×</b>
	Royer	26	1.225	0.214	0.252	0.028	<b>9.00×</b>
HID	CIE	5	29.277	13.781	3.507	2.366	<b>1.48×</b>
	LSPDD	4	0.755	0.761	0.111	0.110	<b>1.01×</b>
	Royer	36	1.817	1.975	0.272	0.195	<b>1.39×</b>
Halogen	LSPDD	31	0.293	0.047	0.040	0.005	<b>8.00×</b>
Laser	Royer	9	2.073	2.076	0.504	0.505	<b>0.99×</b>

**Table 2** Results of *Test 2*, executed on *renders* of the Macbeth Color Checker instead of synthetic calculations. Note that the results of both our and the uplifting technique had to be scaled in order to match the luminosity of the renders. However, as for all the other evaluation scenarios, we again highlight the *relative* color error differences (shown in the last column labeled *Improvement*) as opposed to the absolute values.

the capture, both *Test 2* and *Test 3* apply the uplifting to the white patch of the Macbeth Color Checker, as it directly reflects the RGB value of the illuminant.

We place the main focus of the evaluation of our method on *Test 1* and *Test 2* due to their wide variety of illuminants. While we emphasize the results of *Test 2* as we find its setup to be the closest to what would happen in real life, we note that final obtained emission spectra had to be scaled due to luminosity properties of the final renders. As the scaling factor was solely derived from the scene, the measurements obtained in *Test 2* lack decimal accuracy. This is why we also place a high importance on the specific error values achieved in *Test 1* – since the evaluation is based purely on synthetic computations, no additional factors can skew the results.

We first present the results of *Test 1* in Table 1. As the uplifting technique uses a model that stores reflectances with respect to the daylight illuminant D65, it is expected to achieve a perfect match when applied to the RGB value of D65 and a very high level of accuracy when applied to daylight illuminants with similar spectral shapes. While this is supported by the results, the only datasets where uplifting outperforms our method are the Daylight CIE and Daylight Kider. The rest see a rather significant improvement by utilizing our technique. The average error is, in most cases, lowered by more than a factor of 10, which is rather noteworthy. Even the Prague Sky Model benefits from our method, which we attribute to it also containing sunset spectra that are quite far from D65 in terms of spectral shape. While a significant improvement can also be seen for the maximum error, we note that the specific values are not representative of the performance for the whole dataset, as they can be caused by outliers being present. The measurements are mainly included to show the scale of the potential error that an insufficient light source estimation may cause.

Additionally, we emphasize that for all performed evaluation scenarios, the key takeaway is the *relative* difference between the two techniques, as the absolute values are directly proportional to the luminosity of the illuminant and therefore not representative of the meth-

ods' performance. This is where *Test 1* demonstrates promising results for our technique. We show some of them in Figure 3, where it is clear that the estimated spectral shapes follow the ground truth quite closely, while the current state-of-the-art uplifting results in a significant deviation.

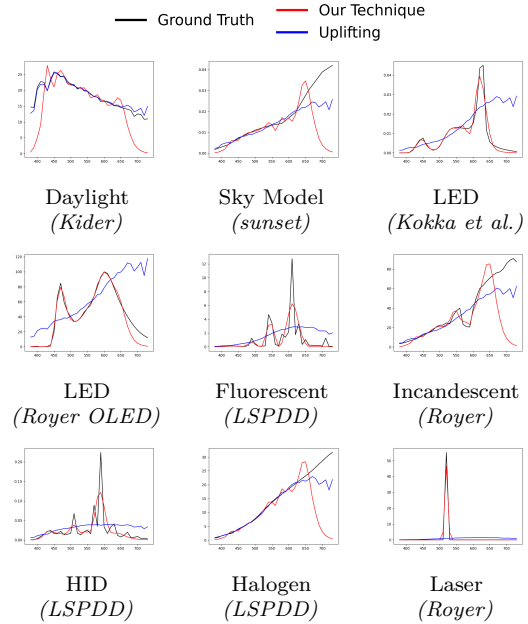


**Figure 3** Samples from *Test 1* for multiple light source categories and datasets. The high precision of the input data allows our technique to closely reconstruct even extremely narrow spikes (see the *Laser* or *Fluorescent* reconstruction).

However, the results of *Test 2* (shown in Table 2) do not support these claims to such an extent. Firstly, while the expected behavior for daylight datasets is for

the uplifting to outperform our technique, this does not happen in this test. Upon closer examination, we attribute this to the inaccuracies of the uplifting technique, which are mainly caused by the necessity to apply a scaling factor to the final emission spectrum in order to maintain luminosity consistency with the ground truth. This is necessary, as the uplifting is applied to the color target, which has inherently lower luminosity than the original illuminant. However, while our technique uses the whole color target to obtain the scaling factor, the uplifting technique only has the information from the white patch to work with. Using the scaling factor of our technique only additionally worsens the results. Therefore, although the uplifting technique generally produces spectral shapes that resemble the ground truth for daylight conditions — and in some cases, even achieves near-perfect matches — the final average error is ultimately higher. This demonstrates the unreliability of the uplifting technique when used in practical scenarios.

Secondly, following the results of *Test 1*, the expected behavior would be an outperformance of our technique for the rest of the categories. While this holds true for most of the datasets, the relative error differences are not as significant as for *Test 1*. In case of the LED Royer and Laser Royer datasets, using the uplifting technique even offers a slight advantage. Additionally, there are multiple other samples among other sets where our technique does not achieve the expected performance.

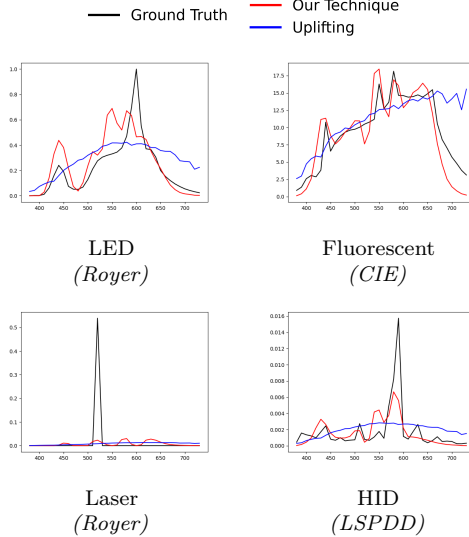


**Figure 4** Samples from *Test 2* that show the shortcomings of our technique, along with their comparison to the current state-of-the-art emission uplifting. Note that even though our technique has lower accuracy in the visualized cases, in most of them, the resulting spectral shapes follow the ground truth more closely. Also note that the fluorescent illuminant shown is a narrowband illuminant.

In Figure 4, we show some of these samples. By examining their properties (along with the properties of other subpar estimates), we can see a clear pattern forming — in all cases, while the estimate describes the shape of the curve rather closely, it fails to reproduce specific spikes that are present for narrow wavelength bands. This observed pattern is consistent across all datasets. While our technique completely fails in identifying lasers and also performs below expectations for the fluorescent and HID light sources and even the LED Royer dataset (which all contain narrow spikes), it performs

quite well for smooth and simple emission spectra, such as incandescent or halogen, as well as smoother LED spectra, which contain wider spikes.

We attribute this shortcoming to our choice of the sampling rate as well as the color target. The 10 nm increments are insufficient for capturing the extreme spikes present for narrow wavelength bands. Additionally, the smooth and simple reflectances of the Macbeth Color Checker are also suboptimal for capturing the metameristic artifacts caused by such complex emission, for which additional patches with more pronounced spectral features could be more suitable.

Finally, we evaluate *Test 3*, which involves applying our technique to 4 photos taken in the Judge QC Light Booth. As the captures are only JPEGs performed with a mobile phone that was not pointed directly at the color target (i.e. the photos are at an angle), and as the white balance settings were additionally set to default which prevented the capture of raw color data, we make multiple edits to the images in order to satisfy the requirements of our technique. Specifically, we apply white balance, and we correct the exposure of patches that were taken at an angle. We note that the resulting image does still not fully satisfy the presented requirements, and that we advise against focusing on the accuracy of the evaluation and against using our method in this manner. The test is only performed as means to see the application of our technique in practice and should not be used as a basis for further analysis.

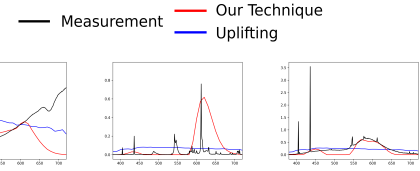


**Figure 5** Results of *Test 3*, shown for 3 of the 4 performed captures. We note the possible inaccuracy of the visualized spectral data, as the input captures did not meet the method’s requirements and as the ground truth measurements may also be susceptible to errors. Additionally, to account for the significant noise present in the captures, the regularization parameter used in our solution had to be tweaked. Nonetheless, we still recognize our method’s effort to mimic the present spectral patterns, which is not the case for the uplifting technique.

We present the results in Figure 5. While the curves are not as closely matched as in the previous tests, we can see that our estimates are able to mimic the shapes of the original measurements. Therefore, even in suboptimal conditions, we can claim that our method offers advantage over the uplifting technique, which has no notion of the original spectral shape.

Lastly, we note that, in order to preserve consistency, the reflectance data of the patches of the Macbeth Color Checker used in the testing scenarios is identical to the one used during the implementation of our technique, and that is the data from the ART renderer (Alexander Wilkie, 2018). While a disclaimer that using a distinct source could result in slightly different results is necessary, we do not deem this part of the work influential enough to conduct a thorough research of the specific measurements. This is mainly due to the shape of the reflectance spectra, which remains rather consistent throughout a multitude of research work concerned with the specific properties of the Macbeth Color Checker (e.g., McCamy et al. (1976), Lapray et al. (2017) or Gerhardt and Hardeberg (2008)).

## 6 Conclusion

In this paper, we proposed a method capable of estimating spectral emission curves of light sources present at camera capture. The method relies on only a single color target positioned in the captured scene that is evenly illuminated by said light source. The result is obtained from the RGB values of the target's patches with the help of a simple optimization algorithm. While the main goal of this paper was to present a proof of concept and an overview on how the method could be used for arbitrary color targets with distinct precision requirements, we additionally also demonstrate its performance in practice on a specific implementation that uses the Macbeth Color Checker and outputs emission spectra sampled at 10 nm increment (starting at 380 nm with 36 samples).

Given the spectral reconstruction capabilities of such sparse representation, we find the results of our method satisfactory. Although the specific proposed implementation is not capable of accurately reconstructing extremely spiky and complex spectra, such as lasers, the performance for most of the light source categories is noteworthy. While this also applies to the improvement in terms of decreased metamerism artifacts when compared to the current state of the art (i.e. spectral uplifting), the effectiveness of the technique is especially valuable for cases when using existing methods is not viable. This offers novel options for simplifying spectral rendering workflows not only the VFX industry, but possibly also in e.g., the product manufacturing industry.

Despite the favorable results, we note the main drawback of our technique, which is its sensitivity to external conditions. Even minor changes to the placement of the color target or the capture process are capable of significantly affecting the accuracy of the optimization process. This is even more pronounced by noise present in the captures, which is, in practice, unavoidable to at least some degree.

However, we believe that this could be minimized with a more robust and detailed implementation. In the future, our primary focus will be improving the optimization process by allowing room for possible noise.

Additionally, while our choice of color target and sampling rate was in favor of the simplicity of the implementation and ease of use, we note that the combination does not, inherently, have capabilities sufficient for recognizing extremely complex and spiky emission spectra. For workflows requiring high precision, we encourage using a higher sampling rate and a more complex color target. We also do not deny the idea of possibly creating a novel color target for specifically such purposes.

## Bibliography

- 015:2018, CIE, 2018. *Colorimetry, 4th Edition*. Available from doi: 10.25039/TR.015.2018.
- DEEB, Rada; VAN DE WEIJER, Joost; MUSELET, Damien; HEBERT, Mathieu; TREMEAU, Alain, 2018. Deep spectral reflectance and illuminant estimation from self-interreflections. *Journal of the Optical Society of America A*. Vol. 36, no. 1, pp. 105–114.
- DIAMOND, Steven; BOYD, Stephen, 2016. CVXPY: A Python-embedded modeling language for convex optimization. *Journal of Machine Learning Research*. Vol. 17, no. 83, pp. 1–5.
- GERHARDT, Jeremie; HARDEBERG, Jon Y, 2008. Spectral color reproduction minimizing spectral and perceptual color differences. *Color Research & Application: Endorsed by Inter-Society Color Council, The Colour Group (Great Britain), Canadian Society for Color, Color Science Association of Japan, Dutch Society for the Study of Color, The Swedish Colour Centre Foundation, Colour Society of Australia, Centre Français de la Couleur*. Vol. 33, no. 6, pp. 494–504.
- GOULART, Paul J.; CHEN, Yuwen, 2024. *Clarabel: An interior-point solver for conic programs with quadratic objectives*. Available from arXiv: 2405.12762 [math.OC].
- HAN, Dong; COLANTONI, Philippe; DINET, Éric; TRÉMEAUX, Alain, 2022. Lighting Spectral Power Distribution Estimation With RGB Camera. In: *2022 16th International Conference on Signal-Image Technology & Internet-Based Systems (SITIS)*. IEEE, pp. 281–288.
- JAKOB, Wenzel; HANIKA, Johannes, 2019. A Low-Dimensional Function Space for Efficient Spectral Upsampling. In: *Computer Graphics Forum*. Wiley Online Library. Vol. 38, pp. 147–155. No. 2.
- KIDER JR, Joseph T; KNOWLTON, Daniel; NEWLIN, Jeremy; LI, Yining Karl; GREENBERG, Donald P, 2014. A framework for the experimental comparison of solar and skydome illumination. *ACM Transactions on Graphics (TOG)*. Vol. 33, no. 6, pp. 1–12.
- KOKKA, Alexander; POIKONEN, Tuomas; BLATTNER, Peter; JOST, Sophie; FERRERO, Alejandro; PULLI, Tomi; NGO, Mathias; THORSETH, Anders; GERLOFF, Thorsten; DEKKER, Paul, et al., 2018. Development of white LED illuminants for colorimetry and recommendation of white LED reference spectrum for photometry. *Metrologia*. Vol. 55, no. 4, p. 526.
- LAPRAY, Pierre-Jean; THOMAS, Jean-Baptiste; GOUTON, Pierre, 2017. A database of spectral filter array images that combine visible and NIR. In: *Computational Color Imaging: 6th International Workshop, CCIW 2017, Milan, Italy, March 29–31, 2017, Proceedings 6*. Springer, pp. 187–196.
- LEE, Cheol-Hee; MOON, Byung-Joon; LEE, Ho-Young; CHUNG, Eui-Yoon; HA, Yeong-Ho, 2000. Estimation of spectral distribution of scene illumination from a single image. *Journal of Imaging Science and Technology*. Vol. 44, no. 4, pp. 308–320.
- LI, Yuqi; WANG, Chong; ZHAO, Jieyu; YUAN, Qingshu, 2018. Efficient spectral reconstruction using a trichromatic camera via sample optimization. *The Visual Computer*. Vol. 34, pp. 1773–1783.
- MCCAMY, Calvin S; MARCUS, Harold; DAVIDSON, James G, et al., 1976. A color-rendition chart. *J. App. Photog. Eng.* Vol. 2, no. 3, pp. 95–99.
- ROBY, J.; AUBÉ, M, 2019. *Lamp Spectral Power Distribution Database (LSPDD)*. Available also from: <https://lspdd.org/>. Accessed on 03.07.2025.
- ROYER, Michael, 2020. Real Light Source SPDs and Color Data for Use in Research. Available from doi: 10.6084/m9.figshare.12947240.v2.
- SHI, Junsheng; YU, Hongfei; HUANG, Xiaoqiao; CHEN, Zaiqing; TAI, Yonghang, 2014. Illuminant spectrum estimation using a digital color camera and a color chart. In: *Optoelectronic Imaging and Multimedia Technology III*. SPIE. Vol. 9273, p. 927307.
- TÓDOVÁ, Lucia; WILKIE, Alexander, 2025. Constrained spectral uplifting for HDR environment maps. In: *Computer Graphics Forum*. Wiley Online Library. Vol. 44, e15280. No. 1. Available from doi: 10.1111/cgf.15280.

- TOMINAGA, Shoji, 1996. Multichannel vision system for estimating surface and illumination functions. *Journal of the Optical Society of America A*. Vol. 13, no. 11, pp. 2163–2173.
- VÉVODA, Petr; BASHFORD-ROGERS, Thomas; KOLÁŘOVÁ, Monika; WILKIE, Alexander, 2022. A wide spectral range sky radiance model. In: *Computer Graphics Forum*. Wiley Online Library. Vol. 41, pp. 291–298. No. 7.
- WILKIE, Alexander; VEVODA, Petr; BASHFORD-ROGERS, Thomas; HOŠEK, Lukáš; ISER, Tomáš; KOLÁŘOVÁ, Monika; RITTIG, Tobias; KŘIVÁNEK, Jaroslav, 2021. A fitted radiance and attenuation model for realistic atmospheres. *ACM Transactions on Graphics (TOG)*. Vol. 40, no. 4, pp. 1–14.
- X-RITE, 2009. *User Manual (ColorChecker Passport)*. Available also from: [https://www.xrite.com/-/media/xrite/files/manuals\\_and\\_userguides/c/o/colorcheckerpassport\\_user\\_manual\\_en.pdf](https://www.xrite.com/-/media/xrite/files/manuals_and_userguides/c/o/colorcheckerpassport_user_manual_en.pdf). Accessed on 27.02.2025.
- ZHANG, Leihong; XU, Runchu; LU, Shuangquan; YANG, Liuhua; YUAN, Xiao; WANG, Kaiming; ZHANG, Dawei, 2020. Reconstruction of spectral reflectance based on mixed weighting and local optimization. *Ukrainian Journal of Physical Optics*. Vol. 21, no. 2.

# Conclusion

While spectral rendering has the potential for more physically accurate color reproduction in comparison to RGB renderers, its results heavily depend on the fidelity of the spectral representations of materials and their alignment with real-world measurements. This is why the accuracy of spectral uplifting is a crucial part of the spectral rendering pipeline.

However, as summarized in Chapter 1, the current state of the art in spectral uplifting is limited in several key areas. Most of the existing techniques only aim at returning general spectral shapes, which, while satisfying the mandatory requirements of the process, typically do not correspond to real-world counterparts. For specific material categories or types of spectra, this may result in a significant deviation of the final appearance of the render.

This thesis broadens the current scope of spectral uplifting in three main aspects:

**Constrained spectral uplifting.** In Chapter 2, a technique offering user the possibility of constraining the spectral uplifting process is described. This allows the preservation of predefined spectral shapes, which is especially useful in cases where specific saturated objects are the main subjects of the scene, such as superhero costumes in the VFX industry or colorful fabrics in catalogues for product manufacturing. This work is an extension of our previous research on this topic (see Subsection 1.2.3 of Chapter 1).

**HDR environment maps.** Previously available uplifting for emission consisted of only scaling existing reflectance uplifts. This approach posed significant limitations, especially in the context of environment maps. Our second contribution, introduced in Chapter 3, addresses this with a novel technique capable of recognizing the type of illumination in the input map and uplifting based on its real-world measurements. The results show significant improvement for image-based lighting over the current state of the art.

**Light source estimation.** Following up on the uplifting of environment maps, Chapter 4 proposes a method for estimating the spectral power distribution of a light source that illuminates a scene, with the input being only an RGB camera capture containing a properly positioned color target. The technique is based on recognizing the changes in the RGB values of individual patches of the target, and has the potential to reconstruct the spectral power distribution of virtually any type of light source. While the method is not, in itself, a spectral uplifting method, it shows promise to replace both the need for uplifting and manual measurements when determining the spectral properties of the main light sources in a scene. Additional use cases include improvement of the uplifting technique for image-based lighting, and multiple other applications in the product manufacturing industry.

For all of the proposed techniques, the results in terms of the achieved spectral shapes show significant improvement over the current state of the art. This allows the preservation of color information otherwise lost in the previous approaches, which is essential for replicating real-world behavior. The focus on the physical accuracy of the spectra by basing them on real-world measurements can be

considered novel in the area of spectral uplifting, and as such, these contributions significantly expand the research field.

At the same time, the techniques introduced in this work inevitably give rise to an even wider range of questions and open problems – whether in refining the proposed methods or in addressing new challenges that emerge as their result.

## Future Challenges

In the current phase of our research, we identify our light source estimation method (see Chapter 4) as the highest priority for completion. The work has already undergone a peer review cycle and was deemed promising, with a strong encouragement for its further development and finalization. This primarily includes extending the evaluation of the method by including more complex settings, and, as already indicated by the work, refining the optimization algorithm and the spectral representation used. Multiple other ideas for improvement are additionally suggested by the reviews, such as exploring the effect of different camera sensitivity curves and addressing the optimization problem from a different angle (by, for example, using a Gaussian mixture), which are also promising directions for further investigation. Another option, which could even be explored as a separate project, is the design of a new color target. Given the wide range of potential application areas, we consider this to be a valuable research direction.

Another area for future exploration is the practical application of our techniques. While all of the proposals were thoroughly tested on data obtained from our resources, their evaluation within a production pipeline would significantly enhance their value. Moreover, we believe this could uncover new opportunities for their application, which could further motivate their improvement. We particularly highlight our method for uplifting HDR environment maps as a prime candidate for integration within state-of-the-art spectral rendering pipelines, both due to its low implementation effort and its ability to provide significant improvements to the accuracy of the light transport process.

However, apart from building on our current work, spectral uplifting as a research area still has many underexplored aspects with room for advancement. In particular, within production pipelines, we see strong potential in the targeted uplifting of specific material categories or even individual objects that have more complex spectral characteristics. A good example of this is the previous work on skin (Aliaga et al., 2023), which, from the point of view of spectral rendering, is considered a two-layer volume, with each layer defined by both its absorption and scattering spectral curves. Uplifting of an input albedo (i.e. an RGB value) therefore outputs multiple spectral properties. We see possibilities for future work by applying similar principles to other types of materials, such as wood, plastics, metallic paints, gemstones, biological materials like hair or fur, or even makeup or other cosmetic layers of human skin.

# Bibliography

- ALEXANDER WILKIE, Robert F. Tobler, 2018. *The Advanced Rendering Toolkit*. Available also from: <https://cgg.mff.cuni.cz/ART>.
- ALIAGA, Carlos; XIA, Menqi; XIE, Xiao; JARABO, Adrian; BRAUN, Gustav; HERY, Christophe, 2023. A hyperspectral space of skin tones for inverse rendering of biophysical skin properties. In: *Computer Graphics Forum*. Wiley Online Library. Vol. 42, e14887. No. 4.
- BELCOUR, Laurent; BARLA, Pascal; GUENNEBAUD, Gaël, 2023. One-to-Many Spectral Upsampling of Reflectances and Transmittances. In: *Computer Graphics Forum*. Wiley Online Library. Vol. 42, e14886. No. 4.
- BROADBENT, Arthur D, 2004. A critical review of the development of the CIE1931 RGB color-matching functions. *Color Research & Application: Endorsed by Inter-Society Color Council, The Colour Group (Great Britain), Canadian Society for Color, Color Science Association of Japan, Dutch Society for the Study of Color, The Swedish Colour Centre Foundation, Colour Society of Australia, Centre Français de la Couleur*. Vol. 29, no. 4, pp. 267–272.
- BURNS, Scott, 2020. *Fast RGB to Spectrum Conversion for Reflectances* [<http://scottburns.us/fast-rgb-to-spectrum-conversion-for-reflectances/>]. Accessed: 2025-04-28.
- CIE, (International Commission on Illumination), 2019. *Colour-matching functions of CIE 1931 standard colorimetric observer*. Vienna, AT. Available from DOI: 10.25039/CIE.DS.xvudnb9b.
- CIE TECHNICAL REPORT, 2004. *Colorimetry*. Vienna. Tech. rep., Publication 15:2004. CIE Central Bureau. ISBN 978-3-901906-33-6.
- DEVELOPERS, Colour, 2013. *Colour* [<http://github.com/colour-science/colour>]. Released under the New BSD License. Available at: <http://opensource.org/licenses/BSD-3-Clause>.
- FAIRCHILD, Mark D, 2008. Beyond the locus of spectrally pure colors. In: *Color Imaging XIII: Processing, Hardcopy, and Applications*. SPIE. Vol. 6807, pp. 11–16.
- FAIRMAN, Hugh S; BRILL, Michael H; HEMMENDINGER, Henry, 1997. How the CIE 1931 color-matching functions were derived from Wright-Guild data. *Color Research & Application: Endorsed by Inter-Society Color Council, The Colour Group (Great Britain), Canadian Society for Color, Color Science Association of Japan, Dutch Society for the Study of Color, The Swedish Colour Centre Foundation, Colour Society of Australia, Centre Français de la Couleur*. Vol. 22, no. 1, pp. 11–23.
- FASCIONE, Luca; HANIKA, Johannes; LEONE, Mark; DROSKE Marc and Schwarzaupt, Jorge; DAVIDOVIČ, Tomáš; WEIDLICH, Andrea; MENG, Johannes, 2018. Manuka: A batch-shading architecture for spectral path tracing in movie production. *ACM Transactions on Graphics (TOG)*. Vol. 37, no. 3, pp. 1–18.

- GLASSNER, Andrew S, 1989. How to derive a spectrum from an RGB triplet. *IEEE Computer Graphics and Applications*. Vol. 9, no. 4, pp. 95–99.
- GUARNERA, Claudio; GITLINA, Yuliya; DESCHAINTRE, Valentin; GHOSH, Abhijeet, 2022. Spectral upsampling approaches for RGB illumination. In: *Eurographics Symposium on Rendering*. Eurographics Association.
- IBRAHEEM, Noor A; HASAN, Mokhtar M; KHAN, Rafiqul Z; MISHRA, Pramod K, 2012. Understanding color models: a review. *ARPN Journal of science and technology*. Vol. 2, no. 3, pp. 265–275.
- JAKOB, Wenzel; HANIKA, Johannes, 2019. A Low-Dimensional Function Space for Efficient Spectral Upsampling. In: *Computer Graphics Forum*. Wiley Online Library. Vol. 38, pp. 147–155. No. 2.
- JAKOB, Wenzel; SPEIERER, Sébastien; ROUSSEL, Nicolas; NIMIER-DAVID, Merlin; VICINI, Delio; ZELTNER, Tizian; NICOLET, Baptiste; CRESPO, Miguel; LEROY, Vincent; ZHANG, Ziyi, 2022. *Mitsuba 3 renderer*. Version 3.0.1. <https://mitsubarenderer.org>.
- JOBLOVE, George H; GREENBERG, Donald, 1978. Color spaces for computer graphics. In: *Proceedings of the 5th annual conference on Computer graphics and interactive techniques*, pp. 20–25.
- JUDD, Deane B, 1949. *Response functions for types of vision according to the Müller theory*. US Government Printing Office.
- JUNG, Alisa; WILKIE, Alexander; HANIKA, Johannes; JAKOB, Wenzel; DACHSBACHER, Carsten, 2019. Wide gamut spectral upsampling with fluorescence. In: *Computer Graphics Forum*. Wiley Online Library. Vol. 38, pp. 87–96. No. 4.
- KÖNIG, Lars; JUNG, Alisa; DACHSBACHER, Carsten, 2020. Improving Spectral Upsampling with Fluorescence. In: *MAM@ EGSR*, pp. 9–12.
- LEHTONEN, Juha; PARKKINEN, Jussi; JAASKELAINEN, Timo, 2006. Optimal sampling of color spectra. *Journal of the Optical Society of America A*. Vol. 23, no. 12, pp. 2983–2988.
- MACADAM, David L, 1935. The theory of the maximum visual efficiency of colored materials. *JOSA*. Vol. 25, no. 8, pp. 249–252.
- MALLETT, Ian; YUKSEL, Cem, 2019. Spectral Primary Decomposition for Rendering with sRGB Reflectance. In: *EGSR (DL/I)*, pp. 9–15.
- MENG, Johannes; SIMON, Florian; HANIKA, Johannes; DACHSBACHER, Carsten, 2015. Physically meaningful rendering using tristimulus colours. In: *Computer Graphics Forum*. Wiley Online Library. Vol. 34, pp. 31–40. No. 4.
- MOKRZYCKI, WS; TATOL, Maciej, 2011. Colour difference $\Delta$  EA survey. *Mach. Graph. Vis.* Vol. 20, no. 4, pp. 383–411.
- NASSAU, Kurt, 1987. The fifteen causes of color: The physics and chemistry of color. *Color Research & Application*. Vol. 12, no. 1, pp. 4–26.
- OHNO, Yoshi, 2000. CIE fundamentals for color measurements. In: *NIP & Digital Fabrication Conference*. Society of Imaging Science and Technology. Vol. 16, pp. 540–545.

- OTSU, Hisanari; YAMAMOTO, Masafumi; HACHISUKA, Toshiya, 2018. Reproducing spectral reflectances from tristimulus colours. In: *Computer Graphics Forum*. Wiley Online Library. Vol. 37, pp. 370–381. No. 6.
- PETERS, Christoph; MERZBACH, Sebastian; HANIKA, Johannes; DACHSBACHER, Carsten, 2019a. Supplementary Document on Using Moments to Represent Bounded Signals for Spectral Rendering.
- PETERS, Christoph; MERZBACH, Sebastian; HANIKA, Johannes; DACHSBACHER, Carsten, 2019b. Using moments to represent bounded signals for spectral rendering. *ACM Transactions on Graphics (TOG)*. Vol. 38, no. 4, pp. 1–14.
- PHARR, Matt; JAKOB, Wenzel; HUMPHREYS, Greg, 2023. *Physically based rendering: From theory to implementation*. MIT Press.
- SCHANDA, János, 2007. *Colorimetry: understanding the CIE system*. John Wiley & Sons.
- SHARMA, Gaurav; WU, Wencheng; DALAL, Edul N, 2005. The CIEDE2000 color-difference formula: Implementation notes, supplementary test data, and mathematical observations. *Color Research & Application: Endorsed by Inter-Society Color Council, The Colour Group (Great Britain), Canadian Society for Color, Color Science Association of Japan, Dutch Society for the Study of Color, The Swedish Colour Centre Foundation, Colour Society of Australia, Centre Français de la Couleur*. Vol. 30, no. 1, pp. 21–30.
- SMITS, Brian, 1999. An RGB-to-spectrum conversion for reflectances. *Journal of Graphics Tools*. Vol. 4, no. 4, pp. 11–22.
- STANDARD, CIE et al., 2007. Colorimetry-part 4: CIE 1976 L\* a\* b\* colour space. *International Standard*, pp. 2019–06.
- STOCKMAN, Andrew; SHARPE, Lindsay T, 2000. The spectral sensitivities of the middle-and long-wavelength-sensitive cones derived from measurements in observers of known genotype. *Vision research*. Vol. 40, no. 13, pp. 1711–1737.
- SÜSSTRUNK, Sabine; BUCKLEY, Robert; SWEN, Steve, 1999. Standard RGB color spaces. In: *Color and imaging conference*. Society of Imaging Science and Technology. Vol. 7, pp. 127–134.
- TÓDOVÁ, Lucia, 2021. *Constrained Spectral Uplifting*. Prague, Czech republic. Diploma thesis. Charles University. Supervised by Wilkie, Alexander.
- TÓDOVÁ, Lucia; WILKIE, Alexander, 2024. Constrained Spectral Uplifting for HDR Environment Maps. In: HAINES, Eric; GARCES, Elena (eds.). *Eurographics Symposium on Rendering*. The Eurographics Association. ISBN 978-3-03868-262-2. ISSN 1727-3463. Available from DOI: [10.2312/sr.20241153](https://doi.org/10.2312/sr.20241153).
- TÓDOVÁ, Lucia; WILKIE, Alexander, 2025. Constrained spectral uplifting for HDR environment maps. In: *Computer Graphics Forum*. Wiley Online Library. Vol. 44, e15280. No. 1. Available from DOI: [10.1111/cgf.15280](https://doi.org/10.1111/cgf.15280).
- TÓDOVÁ, Lucia; WILKIE, Alexander; FASCIONE, Luca, 2021. Moment-based Constrained Spectral Uplifting. In: *EGSR (DL)*, pp. 215–224.

- TÓDOVÁ, Lucia; WILKIE, Alexander; FASCIONE, Luca, 2022. Wide Gamut Moment-based Constrained Spectral Uplifting. In: *Computer Graphics Forum*. Wiley Online Library. Vol. 41, pp. 258–272. No. 6. Available from DOI: [10.1111/cgf.14617](https://doi.org/10.1111/cgf.14617).
- VAN DE RUIT, Mark; EISEMANN, Elmar, 2023. Metameric: Spectral Uplifting via Controllable Color Constraints. In: *ACM SIGGRAPH 2023 Conference Proceedings*, pp. 1–10.
- WEIDLICH, Andrea; FORSYTHE, Alex; DYER, Scott; MANSENCAL, Thomas; HANIKA, Johannes; WILKIE, Alexander; EMROSE, Luke; LANGLANDS, Anders, 2021. Spectral imaging in production: course notes Siggraph 2021. In: *ACM SIGGRAPH 2021 Courses*, pp. 1–90.
- WILKIE, Alexander; NAWAZ, Sehera; DROSKE, Marc; WEIDLICH, Andrea; HANIKA, Johannes, 2014. Hero wavelength spectral sampling. In: *Computer Graphics Forum*. Wiley Online Library. Vol. 33, pp. 123–131. No. 4.
- WYSZECKI, Günther; STILES, Walter Stanley, 2000. *Color science: concepts and methods, quantitative data and formulae*. John wiley & sons.
- ZHANG, Jingang; SU, Runmu; FU, Qiang; REN, Wenqi; HEIDE, Felix; NIE, Yunfeng, 2022. A survey on computational spectral reconstruction methods from RGB to hyperspectral imaging. *Scientific reports*. Vol. 12, no. 1, p. 11905.

# List of Figures

1.1	The electromagnetic spectrum. . . . .	8
1.2	Examples of spectral properties of materials and their interaction. . . . .	9
1.3	Relative cone sensitivities. . . . .	10
1.4	Color processing of the human brain. . . . .	11
1.5	Color matching functions. . . . .	12
1.6	Color gamuts of some of the most popular RGB color spaces visualized in the chromaticity diagram. . . . .	14
1.7	Comparison of the same scene rendered with a spectral and an RGB renderer. . . . .	17
1.8	An example of illuminant metamerism. . . . .	18
1.9	The effects of metamerism. . . . .	19
1.10	Two spectral renders of the same scene with distinct uplifting methods applied to the same RGB HDR environment map. . . . .	20
1.11	Importance of shape consistency when designing an uplifting method. . . . .	21
1.12	Examples of possible metamers for distinct colors of the chromaticity diagram. . . . .	22
1.13	Examples of different general reflectance uplifting techniques when applied to two distinct sRGB values. . . . .	25
1.14	Results of constrained uplifting in the sRGB gamut. . . . .	29
2.1	The shape of the gamut of realizable reflectances in the 3D RGB space. . . . .	30
3.1	The core principle behind the proposed method for HDR environment map uplifting. . . . .	48
3.2	A summary of the proposed uplifting process for HDR environment maps. . . . .	49

# List of Publications

## Conference Publications

TÓDOVÁ, Lucia; WILKIE, Alexander, 2024. Constrained Spectral Uplifting for HDR Environment Maps. In: HAINES, Eric; GARCÉS, Elena (eds.). *Eurographics Symposium on Rendering*. The Eurographics Association. ISBN 978-3-03868-262-2. ISSN 1727-3463. Available from DOI: [10.2312/sr.20241153](https://doi.org/10.2312/sr.20241153).

## Journal Publications

TÓDOVÁ, Lucia; WILKIE, Alexander, 2025. Constrained spectral uplifting for HDR environment maps. In: *Computer Graphics Forum*. Wiley Online Library. Vol. 44, e15280. No. 1. Available from DOI: [10.1111/cgf.15280](https://doi.org/10.1111/cgf.15280).

TÓDOVÁ, Lucia; WILKIE, Alexander; FASCIONE, Luca, 2022. Wide Gamut Moment-based Constrained Spectral Uplifting. In: *Computer Graphics Forum*. Wiley Online Library. Vol. 41, pp. 258–272. No. 6. Available from DOI: [10.1111/cgf.14617](https://doi.org/10.1111/cgf.14617).